NUREG/CR-6664
ANL-99/23

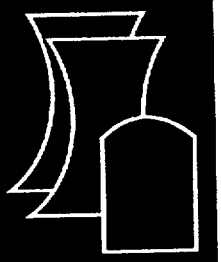

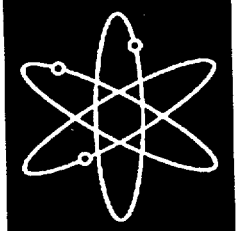

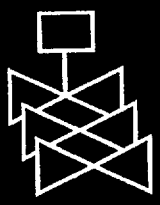

Pressure and Leak-Rate Tests and Models for Predicting Failure of Flawed Steam Generator Tubes

Argonne National Laboratory

U.S. Nuclear Regulatory Commission
Office of Nuclear Regulatory Research
Washington, DC 20555-0001

AVAILABILITY OF REFERENCE MATERIALS IN NRC PUBLICATIONS

NRC Reference Material

As of November 1999, you may electronically access NUREG-series publications and other NRC records at NRC's Public Electronic Reading Room at www.nrc.gov/NRC/ADAMS/index.html.
Publicly released records include, to name a few, NUREG-series publications; *Federal Register* notices; applicant, licensee, and vendor documents and correspondence; NRC correspondence and internal memoranda; bulletins and information notices; inspection and investigative reports; licensee event reports; and Commission papers and their attachments.

NRC publications in the NUREG series, NRC regulations, and *Title 10, Energy*, in the Code of *Federal Regulations* may also be purchased from one of these two sources.

1. The Superintendent of Documents
   U.S. Government Printing Office
   P. O. Box 37082
   Washington, DC 20402–9328
   www.access.gpo.gov/su_docs
   202–512–1800
2. The National Technical Information Service
   Springfield, VA 22161–0002
   www.ntis.gov
   1–800–533–6847 or, locally, 703–805–6000

A single copy of each NRC draft report for comment is available free, to the extent of supply, upon written request as follows:

Address: Office of the Chief Information Officer,
Reproduction and Distribution
Services Section
U.S. Nuclear Regulatory Commission
Washington, DC 20555-0001
E-mail: DISTRIBUTION@nrc.gov
Facsimile: 301–415–2289

Some publications in the NUREG series that are posted at NRC's Web site address www.nrc.gov/NRC/NUREGS/indexnum.html are updated periodically and may differ from the last printed version. Although references to material found on a Web site bear the date the material was accessed, the material available on the date cited may subsequently be removed from the site.

Non-NRC Reference Material

Documents available from public and special technical libraries include all open literature items, such as books, journal articles, and transactions, *Federal Register* notices, Federal and State legislation, and congressional reports. Such documents as theses, dissertations, foreign reports and translations, and non-NRC conference proceedings may be purchased from their sponsoring organization.

Copies of industry codes and standards used in a substantive manner in the NRC regulatory process are maintained at—

The NRC Technical Library
Two White Flint North
11545 Rockville Pike
Rockville, MD 20852–2738

These standards are available in the library for reference use by the public. Codes and standards are usually copyrighted and may be purchased from the originating organization or, if they are American National Standards, from—

American National Standards Institute
11 West 42nd Street
New York, NY 10036–8002
www.ansi.org
212–642–4900

The NUREG series comprises (1) technical and administrative reports and books prepared by the staff (NUREG–XXXX) or agency contractors (NUREG/CR–XXXX), (2) proceedings of conferences (NUREG/CP–XXXX), (3) reports resulting from international agreements (NUREG/IA–XXXX), (4) brochures (NUREG/BR–XXXX), and (5) compilations of legal decisions and orders of the Commission and Atomic and Safety Licensing Boards and of Directors' decisions under Section 2.206 of NRC's regulations (NUREG–0750).

NUREG/CR-6664
ANL-99/23

Pressure and Leak-Rate Tests and Models for Predicting Failure of Flawed Steam Generator Tubes

Manuscript Completed: June 2000
Date Published: August 2000

Prepared by
S. Majumdar, K. Kasza, J. Franklin

Argonne National Laboratory
9700 South Cass Avenue
Argonne, IL 60439

J. Muscara, NRC Project Manager

Prepared for
Division of Engineering Technology
Office of Nuclear Regulatory Research
U.S. Nuclear Regulatory Commission
Washington, DC 20555-0001
NRC Job Code W6487

Pressure and Leak-Rate Tests and Models for Predicting Failure of Flawed Steam Generator Tubes

by

Saurin Majumdar, Ken Kasza, and Jeff Franklin

Abstract

This report summarizes the models used for predicting failure pressures and leak rates in unrepaired steam generator tubes with axial and circumferential cracks that developed under normal operation and design-basis accident conditions. These models are first validated with failure and leak rate tests at room temperature and at 282°C on tubes with well-characterized rectangular EDM notches and are then applied to the failure and leak rate tests conducted on tubes with laboratory-generated outer-diameter stress corrosion cracks (ODSCC), which have highly complex morphology. A procedure for defining equivalent rectangular cracks for SCC cracks on the basis of Eddy Current +Point™ data is presented. Except for tests that exhibited time-dependent initiation and increase of leak rates, the model predictions are in reasonable agreement with test results. In the second half of the report, a model is presented for predicting failure during severe accidents of Electrosleeved* steam generator tubes with axial cracks in the parent tubes. The model is refined on the basis of high-temperature failure test results on Electrosleeved tubes with electro-discharge-machined notches. It is then used to predict failure of Electrosleeved tubes with cracks subjected to postulated severe accident transients.

*Electrosleeve is a trademark of Ontario Hydro Technologies, Inc.

Contents

Abstract iii

Executive Summary xv

Acknowledgments xviii

List of Acronyms xix

List of Symbols xx

1 Introduction 1

2 Background Information 3

3 Failure and Leak Rate Models Applicable to Normal Operation and Design-Basis Accident Conditions 5
- 3.1 Axial Cracks 5
  - 3.1.1 Throughwall Axial Cracks 5
  - 3.1.2 Part-Throughwall Axial Cracks 6
- 3.2 Circumferential Cracks 8
  - 3.2.1 Throughwall Circumferential Cracks 8
  - 3.2.2 Part-Throughwall Circumferential Cracks 20
- 3.3 Leak Rate Model 22

4 Pressure and Leak Rate Tests 24
- 4.1 Tests on Machined (EDM) Notches 24
  - 4.1.1 Predicted Failure Pressures 24
  - 4.1.2 Predicted Leak Rates 25
- 4.2 Tests on Heat-Treated Tubes with Laboratory-Grown Stress Corrosion Cracks 26
  - 4.2.1 Predicted Failure Pressures 27
  - 4.2.2 Predicted Leak Rates 28

5 Behavior of Electrosleeved Tubes at High Temperatures 32
- 5.1 Determination of m_p for Axial Cracks 32
- 5.2 Material Property Data for Electrosleeve 33
- 5.3 Analytical Model Based on Hall-Petch Equation 34
- 5.4 Initial Analytical Results 37
  - 5.4.1 Results for Unsleeved Tubes 37
  - 5.4.2 Predicted Results for Electrosleeved Tubes 37
  - 5.4.3 Predicted vs. Observed Failure Temperatures for FTI Tests 38
- 5.5 ANL Test Results 38
  - 5.5.1 Revised Unaged Flow Stress Curve of Electrosleeve 39
  - 5.5.2 Predicted Failure Temperatures 39
  - 5.5.3 Part-Throughwall Cracks 40
- 5.6 Predicted Failure Temperatures for Postulated SBO Severe Accidents 42
- 5.7 Sensitivity Analyses 42

5.7.1 Creep Effect 42
5.7.2 Thickness of Electrosleeve 43
5.7.3 Crack Depth 43
5.7.4 Crack Length 43
5.7.5 Variation of Activation Energy with Temperature 44
5.7.6 Failure Criterion 44
5.7.7 Reduction of Flow Stress with Aging 45

6 Discussions and Conclusions 46
6.1 Transversely Supported SG Tubes with Circumferential Cracks 46
6.2 Failure and Leak Rate Tests on SG Tubes with EDM Notches and Stress Corrosion Cracks 47
6.3 Electrosleeved Tubes under Simulated Severe Accident Loading 48

References 51

Figures

Fig. 1. Predicted crack opening areas by FEA (finite deformation) vs. those predicted by the Zahoor model of 12.7 mm (0.5 in.) long throughwall axial crack for yield stress values of 179 MPa (26 ksi), 234 MPa (34 ksi) and 296 MPa (43 ksi)..... 61

Fig. 2. (a) Crack depth profile in Specimen SGL-177 as measured by Eddy Current +Point and (b) a candidate equivalent rectangular crack corresponding to depth d_O = 50%..... 61

Fig. 3. Ligament rupture pressures corresponding to three candidate equivalent rectangular cracks, 11 mm by 60%, 9 mm by 70%, and 7 mm by 75%. Equivalent rectangular crack for SGL-177 is 9 mm by 70% because it corresponds to lowest ligament rupture pressure (30 MPa). 62

Fig. 4. Geometry, loading, and idealized deformation of tube with single throughwall circumferential crack 62

Fig. 5. Calculated (by FEA) displaced (solid line) and original (dashed line) shape of laterally supported tube (L/R=26) with single 240° throughwall circumferential crack at clamped edge..... 63

Fig. 6. Stress distribution through section at collapse of tube with single throughwall circumferential crack 63

Fig. 7. Variation of fracture toughness with critical crack tip opening displacement for material with E = 2 x 10^5 MPa..... 64

Fig. 8. (a) Determination of axial yield strength S_Y for bending analysis using Tresca criterion and (b) predicted variation of pressure to cause initial yielding of the tube away from the crack plane with crack angle as a function of ratio between yield to flow stress..... 64

Fig. 9. Normalized uniaxial stress-strain curve (symbols used in FEA) and power-law fit..... 65

Fig. 10. Comparison of model prediction and elastic-plastic FEA results $(\sigma_y / \sigma = 0.5)$ for (a) crack section rotation and (b) support reaction force of tube simply supported at one end and clamped at the other (as in Fig. 4) at various normalized pressures..... 65

Fig. 11. Radial loading path used in FEA is replaced in model by nonradial path consisting of loading to final pressure (at 2 to 1 stress ratio) followed by applying axial bending stress at constant hoop stress. 66

Fig. 12. Nonlinear stress distribution through section away from crack section after yield for power-law hardening material..... 66

Fig. 13. (a) Model-calculated normalized rotation vs. applied bending moment for configuration of Fig. 4 and a polynomial fit to results, and (b) variation of crack section rotation with normalized pressure as calculated by FEA ($\sigma_y / \sigma = 0.5$) and those calculated by model that allows for plastic yielding away from crack plane. 67

Fig. 14. Variation of failure pressure, normalized by unflawed burst pressure, of tube with crack angle of single throughwall circumferential crack (a) with plasticity confined to crack plane and (b) allowing for plastic yielding away from crack plane..... 67

Fig. 15. Calculated variation of applied tearing modulus with pressure, normalized by unflawed burst pressure, for single 180°, 240°, and 300° throughwall circumferential cracks in a tube, using power-law hardening stress-strain curve..... 68

Fig. 16. Normalized crack opening area vs. pressure plots calculated by Paris/Tada model (dashed line) and by current model (solid lines) for L/R = 0 (fully constrained), 60, 120, and infinitely (free-bending) long simply-supported-clamped tube with 240° crack at clamped edge..... 68

Fig. 17. Stress distributions through section at failure of tubes with (a) two symmetrically located part-through circumferential cracks and (b) single part-through circumferential crack..... 69

Fig. 18. Variations of experimental failure bending moments with crack angle and those predicted by (a) Kurihara model and (b) ANL model for unsymmetrical part-through circumferentially cracked 165.2-mm-diameter (11-mm wall thickness) pipe specimens subjected to four-point bend test with constant internal pressure of 6.9 MPa (1000 psi) at room temperature. Dashed lines denote predicted failure bending moments for throughwall cracks; open symbols denote tests that failed by leakage, and filled symbols denote those that failed by breaking into two pieces..... 70

Fig. 19. (a) Engineering stress-strain curves for as-received and heat treated Alloy 600 at room temperature and (b) estimated reduction of flow properties with temperature..... 71

Fig. 20. Predicted vs. observed ligament rupture pressures for notched (a) as-received and (b) heat-treated tubes tested at 20°C. Arrows indicate no failure. Square, circles, diamond, and triangles indicate specimens with 60%, 80%, 90%, and 100% throughwall notches, respectively. Open symbols denote ligament rupture, and filled symbols denote unstable burst..... 71

Fig. 21. Predicted vs. observed ligament rupture pressures for notched as-received tubes tested at 282°C. Arrow indicates no failure. Diamond and triangle indicate specimens with 90% and 100% throughwall notches, respectively. Open symbol denotes ligament rupture, and filled symbol denotes unstable burst..... 72

Fig. 22. Comparison of calculated (solid line) vs. experimentally measured (symbols) leak rates at 20°C for as-received and heat-treated 22-mm (7/8 in.)-diameter tubes with (a) 25.4 mm (1 in.) and (b) 12.7 mm (0.5 in.) throughwall axial EDM notches. Cross symbols (x) in Fig. 22a denote calculated leak rates using posttest measured crack opening areas. 72

Fig. 23. Calculated (solid line) vs. experimentally measured (symbol) leak rates in as-received 22-mm (7/8 in.)-diameter tubes with (a) 6.35 mm (0.25 in.) flaw at 20°C and (b) 12.7 mm (0.5 in.) flaw at 282°C. 73

Fig. 24. Correction factors for obtaining leak rates in as-received Alloy 600 tubes with single throughwall axial cracks from heat-treated tube data at (a) 20°C and (b) 282°C..... 73

Fig. 25. Correction factors for obtaining leak rates in as-received Alloy 600 tubes with single throughwall axial EDM notches from heat-treated tube data at (a) 20°C and (b) 282°C..... 74

Fig. 26. (a) Estimated crack depth profile from Eddy Current +Point data for specimen SGL-195 tested at 20°C and (b) calculated ligament failure pressure of 16.5 MPa for equivalent rectangular crack length of 12.3 mm..... 74

Fig. 27. (a) Estimated crack depth profile from Eddy Current +Point data for specimen SGL-104 tested at 282°C and (b) calculated ligament failure pressure of 18 MPa at an equivalent rectangular crack lengths of 10 mm. 75

Fig. 28. (a) Estimated crack depth profile from Eddy Current +Point data for specimen SGL-219 tested at 282°C and (b) calculated ligament failure pressure of 20 MPa at equivalent rectangular crack lengths of 10.5 mm. 75

Fig. 29. Estimated crack depth profile from Eddy Current +Point data for Westinghouse tube 2-10..... 76

Fig. 30. Calculated ligament rupture pressure for two equivalent rectangular cracks in Westinghouse tube 2-10 at (a) room temperature and (b) 282°C. 76

Fig. 31. Effective throughwall crack length estimated from leak rate data for test SGL-177. 77

Fig. 32. (a) Posttest and (b) pretest dye-penetrant-enhanced views of crack in test specimen SGL-177. Marker in (a) indicates effective throughwall crack length (5.6 mm) estimated (Fig. 31) from measured leak rate..... 77

Fig. 33. (a) Predicted leak rate vs. pressure plot for test SGL-195; symbol represents measured leak rate at maximum test pressure after abrupt increase of leak rate. (b) Posttest view of OD crack of specimen SGL-195; marker indicates equivalent rectangular crack length (12.3 mm)..... 78

Fig. 34. (a) Predicted leak rate vs. pressure plot for test SGL-104; symbol represents measured leak rate at maximum test pressure after abrupt increase of leak rate. (b) Posttest view of OD crack of specimen SGL-104; marker indicates equivalent rectangular crack length (10 mm). 78

Fig. 35. (a) Effective throughwall crack lengths estimated from leak rate data for test SGL- 219 and (b) posttest view of OD crack of specimen SGL219. Marker indicates final effective throughwall crack length (11 mm) calculated from measured leak rate. 79

Fig. 36. (a) Calculated leak rate in Westinghouse tube 2-10 vs. crack length at 17.2 and 18.6 MPa at room temperature and at 18.6 MPa at 282°C. (b) Posttest view of OD crack of Westinghouse specimen 2-10. Marker indicates effective throughwall crack length (4.8 mm) calculated from measured leak rate. 79

Fig. 37. Reference geometry for Electrosleeved steam generator tube with axial crack... 80

Fig. 38. Variation of m_p' factor with pressure for (a) 76-mm (3 in.)-long and (b) 13-mm (0.5 in.)-long cracks for various values of flow stress ratios between tube and Electrosleeve..... 80

Fig. 39. Comparison of m_p values calculated by ANL correlation for single layer shell (dashed line) with those by FEA (solid lines with symbols) for ratios of flow stress of Alloy 600 and Electrosleeve of 1, 2, and 3. Tube wall thickness was assumed equal to 1.27 mm (0.050 in.)..... 81

Fig. 40. Variation of m_p reduction factor with flow stress ratio (FSR) as calculated from FEA results for various crack lengths. 81

Fig. 41. Variations of normalized Vickers Hardness Number (VHN) of Electrosleeve material with time under isothermal aging at various temperatures..... 82

Fig. 42. Variation of activation energy for reciprocal of time to onset of rapid reduction of flow stress (or grain growth) with temperature. 82

Fig. 43. Flow stress (without aging) vs. temperature plot for Electrosleeve material and Alloy 600. Electrosleeve data (square symbol) at 760°C were estimated from tensile data on single specimen preaged and tested at 760°C, using n = 0.33. This flow stress curve of Electrosleeve was subsequently modified on the basis of ANL tests. 83

Fig. 44. Flow stress data on Electrosleeve material preaged for various times at high temperatures. All tensile tests were conducted at 343°C, except for test on specimen preaged at 760°C, which was conducted at 760°C. 83

Fig. 45. Flow stress ("unaged") parameter vs. temperature plot for Electrosleeve material. Data (open square symbol) at 760°C were estimated from tensile data (filled square symbol) on specimen aged and tested at 760°C, using a Hall-Petch exponent (a) n = 0.33 and (b) n = 0.40. 84

Fig. 46. Flow stress ("unaged") vs. temperature plot for Electrosleeve material and Alloy 600. Electrosleeve data (square symbol) at 760°C were estimated from tensile data on single specimen preaged and tested at 760°C, using n = 0.4. 84

Fig. 47. Variation of calculated "nucleation" times to onset of rapid loss of flow stress (or grain growth) under isothermal aging with aging temperature for Hall-Petch exponents of n = 0.33 and n = 0.40, using a temperature-dependent activation

energy given by step function in Fig. 42. Also shown are nucleation times for rapid loss of flow stress derived from FTI data shown in Fig. 41. 85

Fig. 48. Comparison of calculated variations of normalized Vickers Hardness Number (VHN) of Electrosleeve, using Hall-Petch model with n = 0.33 and n = 0.4. with experimentally measured variations under isothermal aging at various temperatures. 85

Fig. 49. Time temperature history for tests reported in Ref. 5 (dashed line represents a simplified version) and simplified scoping ramp (solid line). Internal pressure = 16.2 MPa (2.35 ksi). 86

Fig. 50. Calculated variations of flow stress of Electrosleeve material with temperature, using Hall-Petch exponent (a) n = 0.33 and (b) n = 0.40, for scoping ramp (Fig. 49) and constant ramp rate of 1°C/min. 86

Fig. 51. Predicted ligament failure temperatures by Hall-Petch model for Electrosleeved tubes with throughwall axial cracks under scoping ramp (Fig. 49) and constant-temperature ramp rates of 1 and 5°C/min and constant internal pressure of 16.2 MPa (2.35 ksi), using (a) n = 0.33 and (b) n = 0.4..... 87

Fig. 52 Predicted ligament failure temperatures by Hall-Petch model for Electrosleeved tubes with throughwall 360° circumferential crack under various temperature ramps with constant internal pressure of 16.2 MPa (2.35 ksi). 87

Fig. 53. Temperature ramps used in FTI tests on Electrosleeved specimens (a) BTF-23, (b) BTF-25, and (c) R.5.2..... 88

Fig. 54. Calculated variation and ANL test simulation of (a) temperature and (b) pressure differential during SBO (Case 6RU) severe accident transient. 89

Fig. 55. Original unaged flow stress curve (dashed line) of Electrosleeve estimated from FTI tensile data before ANL tests were conducted and revised unaged flow stress curve (solid line) of Electrosleeve calculated using the ANL tests..... 90

Fig. 56. Variation of ANL test failure temperatures (symbols) and predicted upper and lower bounds to the failure temperatures with notch length..... 90

Fig. 57. Predicted vs. observed failure temperatures of ANL tests..... 91

Fig. 58. Stress-strain curves used for (a) Electrosleeve (Case 6RU ramp) and (b) Alloy 600. 91

Fig. 59. Calculated variations of average ligament stress, average ligament plastic strain, yield stress and flow stress of Electrosleeve with temperature under Case 6RU loading on tube with (a) 13-mm (0.5 in.), (b) 25-mm (1 in.), and (c) 51 mm (2 in.)-long 100% throughwall cracks. 92

Fig. 60. Predicted (open symbols) and observed (filled symbols) failure temperatures vs. notch length of FTI tests; the predicted points are based on actual geometry and actual temperature ramp for each specimen..... 93

Fig. 61. Comparison of experimental ligament failure temperatures (open symbols from Ref. 4) with predicted values (solid lines using flow stress model) for unsleeved Alloy 600 tube with part-throughwall axial notches under EPRI ramp. Also shown are FTI data (filled circle) for unsleeved tube with 51 mm (2 in.)/50% TW notch and Electrosleeved tubes (filled squares) with throughwall cracks in parent tubes. 93

Fig. 62. Comparison of FTI test failure temperatures of Electrosleeved tubes with those adjusted by using flow stress model so that all specimens have identical geometry, except for notch length, and are subjected to same temperature ramp as BTF-25 (Fig. 53b). 94

Fig. 63. Calculated variations of ligament-averaged stress, plastic strain, yield stress, and flow stress with temperature under Case 6RU loading of tube with a (a) 13 mm (0.5 in.), (b) 25-mm (1 in.), and (c) 51-mm (2 in.)-long 80% part-throughwall cracks. 94

Fig. 64. Calculated variations of ligament-averaged plastic strain with temperature under Case 6RU loading of tube with a (a) 13-mm (0.5 in.), (b) 25-mm (1 in.), and (c) 51-mm (2 in.)-long, 80, 90, and 100% deep part-throughwall cracks. ... 95

Fig. 65. Predicted ligament failure temperatures for 80, 90, and 100% throughwall cracks due to Case 6RU loading; symbol represents failure temperature of test (BTF-16) conducted at ANL on specimen with 90% part-throughwall, 51-mm (2 in.)-long EDM notch. 96

Fig. 66. Calculated variations of average plastic strain in Alloy 600 tube ligament with temperature under Case 6RU loading of tube with a (a) 13-mm (0.5 in.), (b) 25-mm (1 in.), and (c) 51-mm (2 in.)-long, 80 and 90% deep part-throughwall cracks. Also shown are average ligament plastic strains for 100% throughwall cracks. 97

Fig. 67. Calculated variation of m_p for Alloy 600 tube ligament with temperature under Case 6RU loading of tube with (a) 13-mm (0.5 in.), (b) 25-mm (1 in.), and (c) 51-mm (2 in.)-long 80 and 90% deep part-throughwall cracks. Also shown are m_p (ANL) values for unsleeved tubes with 80 and 90% deep part-throughwall cracks. 98

Fig. 68. Predicted ligament failure temperatures by simplified model for 80, 90, and 100% throughwall cracks due to Case 6RU loading. 99

Fig. 69. Part-throughwall crack depth profiles reported by FTI for specimen (a) BTF-7 and (b) BTF-3. Also shown are equivalent crack lengths and depths. 99

Fig. 70. Temperature ramps used in FTI tests on Electrosleeved specimens with part-throughwall notches (a) BTF-3 and (b) BTF-7. 100

Fig. 71. Effect of Electrosleeve thickness on predicted ligament failure temperature of tube with throughwall axial cracks 101

Fig. 72. Effect of crack length on predicted ligament failure temperature of reference Electrosleeved tube with throughwall axial cracks in parent tube during Case 6RU SBO severe accident ramp 101

Fig. 73. Effect of shape of variation of activation energy with temperature on calculated loss of flow stress for 1°C min ramp. Nucleation time t_n has little effect on flow stress at temperatures of interest. 102

Fig. 74. Variations of average hoop stress, average effective stress, and average hoop plastic strain in ligament with pressure as calculated from FEA results for homogeneous tube of wall thickness 2.24 mm (0.088 in.) containing a 76-mm (3 in.)-long, 1.27-mm (0.050 in.)-deep part-throughwall axial crack. Also shown is variation of nominal hoop stress in unflawed tube with pressure..... 102

Fig. 75. Variations of average hoop stress, average effective stress, and average hoop plastic strain in ligament with pressure as calculated from FEA results for bi-layer tube (simulating Electrosleeved tube at high temperature) with 0.9-mm (0.038 in.)-thick inner layer and 1.27-mm (0.050 in.)-thick outer layer containing 76-mm (3 in.)-long 100% throughwall axial crack. Flow stress ratio between outer and inner layer = 2. Also shown is variation of nominal hoop stress in unflawed tube with pressure. 103

Fig. 76. Comparison of calculated flow stresses (including aging) of Electrosleeve (solid line) with flow stress data (open symbols) of Ni 200 (Huntington) and Ni-201 (ASTM). Also shown are flow stress of unaged electrosleeve (short dashed line) and two FTI flow stress data (filled circle) on 30-min aged specimens. 103

Tables

Table 1. Effective lengths of tubes for several circumferential crack locations and edge conditions 53

Table 2. Summary of notched (EDM) specimens tested in Pressure and Leak Rate Facility and High-Pressure Test Facility (last 7 tests) 54

Table 3. Summary of tests on specimens with ODSCC tested in Pressure and Leak Rate Test Facility 55

Table 4. Summary of estimated leak rates, corrected for flow stress, of ANL tests on heat-treated Alloy 600 steam generator tubes with laboratory-grown SCC cracks. 56

Table 5. Observed and initial predictions of failure temperatures for FTI severe-accident tests on unsleeved and Electrosleeved tubes. 57

Table 6 Summary of simulated severe accident tests conducted at ANL and FTI on notched Electrosleeved tubes 58

Table 7. Predicted failure temperatures by flow stress model and creep rupture model for unsleeved tube with $3\Delta p_{NO}$ crack subjected to various temperature transients and constant internal pressure of 2.35 ksi (16.2 MPa) 59

Table 8. Summary of simulated severe accident tests conducted at ANL and FTI on part-throughwall notched Electrosleeved tube 60

Executive Summary

This report covers two general topics. The first is concerned with models for predicting failure pressures and leak rates of unrepaired Alloy 600 steam generator tubes containing axial and circumferential cracks and subjected to both normal operation and design-basis accident conditions. The second topic is concerned with predicting failure of Electrosleeved* steam generator tubes with throughwall and part-throughwall axial cracks in the parent tubes and subjected to postulated severe accident transients. The accuracy of various predictive models is determined on the basis of available test data on tubes containing machined notches and stress corrosion cracks.

Failure pressures, leak rates, etc., depend on the mechanical properties (primarily the flow stress) of the tubing. The minimum ASME code requirements for yield and ultimate tensile strengths of Alloy 600 steam generator tube are 35 and 80 ksi (240 and 550 MPa), respectively, which correspond to a minimum flow stress of 58 ksi (400 MPa). Some of the older steam generators may have tubes with properties close to the code minimum. The actual flow stress of steam generator tubes in most current plants can vary widely depending on the age and heat of material used. In order to compare results on one material with results on a different material, the effect of variations in the mechanical properties must be accounted for, i.e., the results must be normalized in terms of the flow stress. The analyses of the pressure and leak rate tests have been used to develop procedures that account for flow stress effects.

Finite-element analyses (FEAs) were conducted for axial throughwall cracks to determine the crack opening area as a function of pressure and the flow stress of the material at reactor operating temperatures. Crack opening areas calculated by a simple model (Zahoor's model) as prescribed in the EPRI Ductile Fracture Handbook agreed reasonably well with the FEA results, as well as with measured values.

Models for predicting the onset of crack growth and for calculating crack opening area and leak rate from a throughwall circumferential crack in a steam generator tube have been developed. Under normal operating and design-based accident conditions of pressurized water reactors (PWRs), plasticity is confined to the plane of the crack. However, in failure tests conducted in the laboratory, plasticity does spread to sections away from the crack section. For typical steam generator tubes containing a circumferential throughwall crack at the top of tube sheet, any crack $\leq 180°$ does not reduce the burst pressure from the burst pressure of an unflawed tube. Aiso, tubes with throughwall cracks $\geq 240°$ will behave as if they were fully constrained against bending and will have significantly greater failure pressures than the same tubes under free bending condition – a result that has been verified by tests in Europe. Consequently, steam generator tubes with circumferential cracks at the top of tube sheet can withstand much higher pressures under normal operating temperatures than those calculated on the basis of a simpler free-bending failure analysis. For typical PWR steam generator properties, the longest throughwall circumferential cracks at the top of tube sheet that are predicted to experience onset of crack initiation during normal operation and design basis accident conditions are 340° and 310°, respectively. Crack opening areas during normal operation and design-basis accidents are small when compared with the tube cross-sectional area for a steam generator tube with $\leq 240°$ throughwall cracks at the top of the tube sheet. The driving force for crack instability, which is negligible as long as plasticity is confined to the

*Electrosleeve is a trademark of Ontario Hydro Technologies, Inc.

crack plane, increases rapidly with plastic yielding away from the crack plane. However, failure by unstable tearing is more likely with short cracks (<180°) than with long cracks.

Leak rates measured at The Pressure and Leak Rate Test Facility at ANL on tubes with machined axial throughwall notches can be predicted by the simple orifice leak-rate formula with a coefficient of discharge of 0.6. The difference in the leak rates at room temperature and at 282°C could be accounted for by the density difference of water without explicitly considering the details of the complicated two-phase flow. The models for crack opening area and leak rate have been used to develop calibration curves for converting leak rate data from one material to another with a different flow stress.

An analytical procedure was developed to predict ligament failure pressure for the onset of large leak rates (>19 L/min [5 gpm]) in specimens with deep part-throughwall stress corrosion cracks at normal operating temperatures; this procedure uses an equivalent rectangular crack geometry from the measured pretest eddy current plus-point data. Detailed analyses of the tests on specimens with laboratory-grown SCC cracks show that if the pretest crack depth profile is reasonably uniform and deep (80-90%), as measured by eddy current plus point, a significant portion of the through-thickness crack tip ligament can rupture abruptly at a pressure that can be calculated by the ANL correlation. Posttest pictures of the OD surface did not reveal the presence of surface ligaments in these specimens. Effective throughwall crack lengths estimated by the ligament rupture model using the Eddy Current +Point data are reasonably close to those estimated from the leak rate data and correspond closely to a segment of the crack with >70% throughwall thickness. In these specimens, the leak rate generally increased abruptly from 0 or ≤ 0.04 to >19 L/min (0 or ≤ 0.01 to >5 gpm) under increasing pressure loading, indicating sudden rupture of the ligament, and did not increase under constant pressure hold subsequent to ligament rupture.

For specimens having highly nonuniform crack tip ligament thicknesses (as measured by Eddy Current +Point) with predicted ligament failure pressures that are greater than our system capability (i.e., 2800 psi), the ligaments can fail locally during a constant pressure hold at a lower pressure than the predicted failure pressure. The effective throughwall crack lengths for these specimens can subsequently increase due to time-dependent ligament rupture at both room temperature and 282°C. Based on very scant data, it appears that the time-dependent ligament rupture process occurs at a much slower rate (hours rather than minutes) in the higher-strength tube obtained from Westinghouse than in the lower-strength heat-treated ANL tubes. Also, the time-dependent rupture process occurs more rapidly at 282°C than at room temperature. A procedure for converting the constant pressure hold data on time-dependent leak rate from heat-treated tube to as-received tube must be developed in the future.

In all ANL specimens, the lengths of the throughwall segments of the cracks calculated from leak rate data are close to the lengths of the most open part of the cracks as evident visually from posttest pictures of the specimens. None of these pictures showed the presence of axial segments separated by ligaments. In one test, the posttest measured length of the throughwall segment of the crack (determined by a submerged-bubble technique) is reasonably close to that calculated from the measured leak rate. In contrast to those for the ANL specimens, the calculated throughwall crack length for the Westinghouse specimen is much shorter than that observed visually. However, a posttest picture of the OD surface of this specimen revealed at least three axial segments separated by ligaments, showing that the

effective throughwall crack length can be seriously underestimated from the measured leak rate if the effects of the ligaments on the crack opening area are not taken into account.

Under severe accident conditions, steam generator tubing can be subjected to very high temperatures. If other primary system components fail before the steam generator tubing reaches the temperature at which it will fail, the system will vent inside the containment, the primary system will depressurize, and the steam generator tubes will not fail. If the tubes reach failure before another primary system component fails, a bypass event could occur.

Predicting failure of a complex composite structure such as an Electrosleeved steam generator tube under severe accident transients is a difficult problem. The Electrosleeve material derives its strength from its nanocrystalline grain structure. At the high temperatures anticipated during severe accidents, rapid grain growth occurs, resulting in a loss of strength. When the review of the behavior of Electrosleeve repairs at high temperatures was initiated, only very limited data on the strength of the Electrosleeve material at high temperatures were available. Therefore, analytical models were developed to predict failure. The available data were used to determine the parameters of the models, but no confirmatory test results were initially available.

Two approaches for predicting failure of Electrosleeved tubes were developed. The first is an approximate analytical procedure based on a linear-damage-rule hypothesis analogous to that often used to analyze creep failures. The second is a more mechanistically based approach that accounts for the loss of flow stress due to grain growth. Initial studies showed the failure temperatures predicted by the two approaches were comparable, but the mechanistic model was used for most of the analyses.

After the initial development of the analytical model, Framatome Technologies, Inc. (FTI) provided failure data from six tests on internally pressurized tubes that were subjected to a variety of temperature ramps simulating those expected during the most challenging severe accidents, i.e., "high–dry" sequences that can occur when the core melts, the primary side remains at high pressure, and the secondary side is depressurized. The initial comparison showed that the predicted failure temperatures were within 35–70°C of those observed in the experiments. FTI also provided 11 Electrosleeved specimens that were subsequently tested at ANL. The results from these tests were used to refine the input parameters used in the analytical model. Based on the refined model and more accurate data on the test geometries, the predicted failure temperatures in the FTI and ANL tests are within 15°C of the observed failure temperatures.

The model predicts that Electrosleeved tubes with throughwall axial cracks ≤ 1 in. and throughwall 360° circumferential cracks in the parent tubes will survive "high–dry" transients based on the temperature histories for such sequences presented in NUREG–1570. Tubes with throughwall axial cracks of any length but with depths ≤80% are also predicted to survive these transients.

Acknowledgments

Helpful discussions with Drs. D. R. Diercks and W. J. Shack of Argonne National Laboratory are acknowledged. Thanks are also due to Framatome Technologies, Inc., for providing the Electrosleeved specimens. This work is sponsored by the Office of Nuclear Regulatory research, U.S. Nuclear Regulatory Commission, under Job Code W6487; Project Manager Dr. J. Muscara.

List of Acronyms

ANL	Argonne National Laboratory
ASME	American Society of Mechanical Engineers
COA	Crack opening area
COD	Crack opening displacement
EC	Eddy current
EC + point	Eddy Current Plus Point
EDM	Electrodischarge machining
EPRI	Electric Power Research Institute
FEA	Finite-element analysis
FSR	Flow stress ratio
FTI	Framatome Technologies, Inc.
INEEL	Idaho National Engineering and Environmental Laboratory
NO	Normal operation
NRC	(U.S.) Nuclear Regulatory Commission
ODSCC	Outer diameter (secondary water) stress corrosion cracking
PNNL	Pacific Northwest National Laboratory
PWR	Pressurized water reactor
RT	Room temperature
SBO	Station blackout
SCC	Stress corrosion cracking
SG	Steam generator
TW	Throughwall

List of Symbols

A, A_c	crack opening area and critical crack opening area
a	crack depth
B, C	constants
c	toughness parameter
c, c_e	half crack and half effective crack lengths
d, d_o	notch depths
d, d_i, $\dot{d}$	grain diameter, initial grain diameter and its rate of growth
E	Young's modulus
H	hardness or flow stress
h	wall thickness
I	moment of inertia
J, J_P, J_c	J integral, plastic component of J integral and critical J integral
K, K_{JC}	stress intensity factor and fracture toughness
k	constant for defining flow stress
L, L_o	crack lengths
L_e	effective length
M,	bending moment
M_y, M_L	bending moments to cause first yielding and collapse
m	bulging factor (or exponent for defining stress-strain curve)
m_p	ligament stress magnification factor
n	number of cracks
p, p_y	pressure and pressure to cause first yielding
p_b, p_{cr}	unstable burst pressures for unflawed and flawed tubes
p_{sc}	pressure to cause ligament rupture
Q	activation energy or leak rate
Q_g	activation energy for growth
Q_n	activation energy for nucleation
R	Universal gas constant (1.987 cal/mole/°C)
R, R_o, R_i	mean radius (or radius of curvature), outer radius and inner radius of tube
S_y, S_u	yield and ultimate tensile strengths
T_{APP}, T_{MAT}	applied and material tearing modulus
T, T_f	temperature and failure temperature
t, t_n, t_f	time, nucleation time and failure time
w	transverse displacement
z, z_y	axial coordinate and location of first yielding
β	angular location of plastic neutral axis
Δp	pressure differential
δ, δ_c	crack tip opening and critical crack tip opening displacements
ε, ε_y	strain and yield strain
ϕ, ϕ_c	rotation and critical rotation
ν	Poisson's ratio
ρ	density of water
σ	stress, hoop stress
$\bar{\sigma}$	flow stress
σ_A	axial stress
σ_{lig}	ligament stress

σ_y, σ_u	yield and ultimate tensile strengths
θ	half circumferential crack angle

1 Introduction

For typical unflawed steam generator (SG) tubes made of Alloy 600, the burst pressure, p_b, at room temperature is ≈ 9.4 ksi (65 MPa). However, operating experience with PWR steam generators in both the U.S. and abroad has shown that cracks of various morphologies can and do occur in steam generator tubes, starting early in life. These may be single cracks that are axial or circumferential, inside or outside diameter (ID or OD) initiated, part-throughwall or throughwall, or multiple cracks that are parallel or form a network. Tests have shown that, depending on the location and morphology of these cracks, the tubes can be weakened relative to unflawed tubes to various extents.

Detection of cracks and assessment of leak rate and structural integrity of cracked steam generator tubing during normal operation and accident conditions are of interest because failure of the tubes, including those that have been repaired (e.g., by sleeving), could lead to bypass of the containment.

The primary-to-secondary differential pressure during normal operation of PWR SGs, Δp_{no}, is in the range of 1.25 ksi (8.6 MPa) to 1.6 ksi (11 MPa). Degraded tubes must actually be capable of withstanding $3\Delta p_{no}$ = 3.75 - 4.8 ksi (26 - 33 MPa) to meet requirements for continued operation. Hot leg temperature can range from about 305 to 330°C although most fall in the range of 312 to 320°C. In this temperature range, creep effects are negligible in Alloy 600.

The severest design-basis accident depends on the license of the plant. Typically, main steam line break (MSLB) leads to a long term differential pressure of 2.56 ksi (17.7 MPa) at 315°C. Creep effects are negligible in Alloy 600 at this temperature. For other plants there is a feed line break event that leads to a pressure spike of 2.65 ksi (18.3 MPa). Hence, the pressure differential across a SG tube wall during design basis accident condition, Δp_{MSLB}, can range from 2.56 to 2.65 ksi (17.7 to 18.3 MPa). Degraded tubes must actually be capable of withstanding $1.4\Delta p_{MSLB}$ = 3.58 - 3.71 ksi (24.7 - 25.6 MPa) to meet requirements for continued operation.

Several correlations are currently available for predicting ligament rupture pressure of axial and circumferential part-throughwall rectangular cracks under normal operation, design-basis accident, and severe accident conditions.[1-4] However, data on SG tubing are relatively sparse for short and deep flaws. In this report we present failure data on tubes with notched axial flaws, including those that are short and deep. The same data are used to validate the ANL ligament rupture model presented in Ref. 4.

In contrast to rectangular machined notches, SCC cracks in operating SG tubes are irregularly shaped, have variable depths along their lengths and may have one or more through-thickness penetrations in localized regions. Instead of being a single planar crack, each is composed of a family of crack segments in different planes. Currently, it is not clear as to how much detail must be available on the complex morphology of the cracks before the structural integrity of the tubes can be assessed by mechanistic models. In this report, we present a method for handling such complex-shaped cracks, based on the concept of an equivalent rectangular crack that can be determined from Eddy Current +Point data.

Severe accidents that involve significant core damage are unlikely events in nuclear reactors. Even in the unlikely event that such an accident occurs, in most cases any potential risk to the public is mitigated by the robust containment. The accident sequences that appear to produce the greatest risk of steam generator tube failure are those in which the reactor pressure vessel fails to depressurize, but depressurization does occur on the secondary side. Even in these cases, preliminary investigations suggest that failures are likely to occur in the hot-leg nozzle or the inlet surge-line nozzle, leading to depressurization of the reactor system, which prevents failure of steam generator tubes.[5] However, such calculations are subject to large uncertainties, and the NRC is pursuing additional studies to better understand the progression of such sequences, the temperature of the steam generator tubes during such accidents, and the behavior of steam generator tubes (both unrepaired and repaired) at the high temperatures associated with such accidents. At these high temperatures, plastic deformation is likely to be much more extensive than at normal reactor operating temperatures, and creep effects may no longer be negligible.

Behavior of Electrosleeved* tubes during severe accident is of interest, because Electrosleeving can be used as a repair technique for steam generator tubes. Although the nanocrystalline Electrosleeve has better mechanical properties than those of Alloy 600 at reactor operating temperatures, it loses strength at high temperatures because of grain growth, which raises concern as to its integrity during severe accidents. No relevant data were initially available, and the NRC instructed ANL to investigate by analytical means the high-temperature behavior of Electrosleeved tubes with cracks. In this report, we present a model that can predict failure of Electrosleeved steam generator tubes with cracks in the parent tubes subjected to postulated severe accident transients. Subsequently, both Framatome Technologies, Inc. (FTI) and ANL conducted tests on pressurized Electrosleeved tubes with notches by subjecting them to postulated severe accident transients. These data were used to further refine the model.

*Electrosleeve is a trademark of Ontario Hydro Technologies, Inc.

2 Background Information

Circumferential cracks in steam generator tubes are often detected at the top of the tube sheet in PWR generating plants. Circumferential cracks are of concern because of the potential for double-ended rupture of steam generator tubes and consequent large leaks. In addition, circumferential cracks are considered difficult to detect and accurately size by NDE techniques.

Analytical models[6] for the failure of tubes with circumferential cracks predict that the pressure required to cause onset of crack extension may fall within the MSLB condition (17 MPa) if the tube section that contains the crack is free to bend and the crack is sufficiently long (>180°). It is also known that if the crack section is fully constrained against rotation, the failure pressures are significantly increased and cracks must be much longer (>300°) for the onset of crack propagation to occur. In an actual steam generator, tubes are neither free to bend nor fully constrained. The degree of constraint on a circumferential crack at the top of the tube sheet depends on the span between the top of the tube sheet and the first tube support plate or baffle plate (15-125 cm). Recent tests on steam generator tubes have shown that failure pressures of laterally supported tubes can be significantly higher than those of tubes that are free to bend.[7]

An extensive series of tests on failure and leak rates in circumferentially flawed reactor coolant piping subjected to externally applied forces and moments has been conducted at Battelle Columbus Laboratories under the NRC-sponsored Degraded-Piping[8] and Short Cracks in Piping and Piping Welds Programs.[9] At the same time, finite-element analyses (FEAs) led to the development of the fracture-mechanics-based leak rate estimation model SQUIRT.

A simplified stability analysis of circumferentially cracked reactor piping was presented by Tada et al.,[10] who analyzed the pipe as a beam whose cracked section was subjected to plastic limit moment. A similar approach was followed by Smith to analyze failure[11] and leakage[12] of a throughwall circumferential crack in piping. Smith[13] has emphasized the importance of the crack-system compliance on the onset and stability of crack extension and leakage through a crack. In all of these analyses, plasticity was confined to the crack section, while the rest of the pipe responded elastically. We use the same approach in this report to analyze the problem of steam generator tube failure under internal pressure loading in the absence of externally applied forces and moments, and we consider a case in which plastic deformation may spread to sections other than that of the crack.

Prediction of failure of a complex composite material such as Electrosleeved steam generator tubing under severe accident transients is a difficult problem. The Electrosleeve material is almost pure Ni and derives its strength and other useful properties from its nanocrystalline grain structure, which is stable at reactor operating temperatures. However, it undergoes rapid grain growth at the high temperatures incurred during severe accidents, resulting in a loss of strength and a corresponding decrease in flow stress. The magnitude of this decrease depends on the time/temperature history during the accident. Low-temperature tensile data on the Electrosleeve material (without the tube) are available, but few tensile data on Electrosleeve at high temperatures in either the aged or unaged condition are available. Initially, the assumption was made that there were no experimental failure data available on Electrosleeved tube with cracks. Therefore, analytical models were exclusively relied upon to

predict failure of the composite structure with cracks, using the available tensile data to determine the parameters of the models.

Following initial modeling and analysis, Framatome Technologies, Inc. (FTI) provided failure data from six tests on unsleeved and Electrosleeved tubes with and without notches under simulated severe accident loading. In contrast to the model prediction that the damaging effect of notch length should level off with increasing notch length, the FTI test data indicated that the failure temperature of the Electrosleeved tube decreased almost linearly with notch length. On the other hand, the failure temperatures of the unsleeved and degraded tubes were predicted quite accurately by the flow stress model for Alloy 600 presented in Ref. 4. One of the tests was on an undegraded Alloy 600 tube and involved a long hold time at constant temperature – a loading history for which the flow stress model is inapplicable. However, the creep rupture model for Alloy 600 tubing presented in Ref. 4 predicts the failure time of this specimen within a factor of 2.

Subsequent to their initial tests, FTI supplied twelve Electrosleeved tube specimens, three of which have 51-mm (2 in.)-long throughwall notches for testing at ANL. Eight other specimens were notched by electrodischarge machining (EDM) at ANL with notch lengths of 13, 25, and 76 mm (0.5, 1, and 3 in.), all nominally 100% throughwall of the parent tube. All specimens were tested to failure with a temperature and pressure history that closely simulated those for a station blackout (SBO) with a depressurized secondary side (Case 6RU). This report describes the basis for the analytical models and shows how they were revised on the basis of the test results. Although the initial model overestimated the failure temperatures of the FTI tests, the failure temperatures were predicted accurately by the revised model. Finally, the models are used to predict failure of Electrosleeved steam generator tubing during postulated severe accidents.

Two approaches were developed for predicting failure of Electrosleeved tubes, both based on the flow stress failure model, as discussed in Ref. 4. The first is an approximate analytical procedure based on a linear-damage-rule hypothesis. The second is a more mechanistically based approach that accounts for the loss of flow stress due to grain growth. The predicted failure temperatures by both approaches led to comparable results. Although the work in Ref. 4 showed that a creep model gave a more accurate prediction of failure at high temperatures than did a flow stress model, insufficient data are available to do a creep analysis of the Electrosleeved tube at the present. However, based on comparison with limited experimental failure data, it is believed that in the absence of hold times at constant temperature, flow stress models give reasonable estimates of failure temperatures for Electrosleeved tubes with cracks. The predictions of the relative strength of tubes with and without repairs are probably more accurate than predictions of failure temperatures. The reference geometry of Electrosleeved tubes considered in this report is a 22-mm (7/8 in.)–diameter, 1.27-mm (0.050-in.)-wall-thickness Alloy 600 tubing, with a nominal 0.97-mm (0.038-in.)-thick Electrosleeve at the ID surface.

3 Failure and Leak Rate Models Applicable to Normal Operation and Design-Basis Accident Conditions

Flow-stress-based models are suitable for tubes with cracks operating under normal operation and design-basis accident conditions, because temperatures are too low for creep effects to occur. In the following sections, we summarize the available equations for calculating ligament rupture pressures, crack opening areas, and leak rates of SG tubes with throughwall and part-throughwall, axial and circumferential cracks.

3.1 Axial Cracks

3.1.1 Throughwall Axial Cracks

The critical pressures and crack sizes for the unstable failure (rupture) of a thin-wall internally pressurized cylindrical shell with a single throughwall axial crack can be estimated with an equation originally proposed by Hahn[14] and later modified by Erdogan[15]:

$$p_{cr} = \frac{\bar{\sigma}h}{mR} = \frac{p_b}{m}, \tag{1a}$$

where:

$$\bar{\sigma} = \text{flow stress} = k(S_y + S_u) \text{ (with } k = 0.5 - 0.6), \tag{1b}$$

S_y and S_u = yield and ultimate tensile strengths, respectively, (1c)

$$m = 0.614 + 0.481\lambda + 0.386\exp(-1.25\lambda), \tag{1d}$$

$$\lambda = \left[12(1-\nu^2)\right]^{\frac{1}{4}} \frac{c}{\sqrt{Rh}} = \frac{1.82c}{\sqrt{Rh}}, \tag{1e}$$

$$p_b = \frac{\bar{\sigma}h}{R} = \text{burst pressure of an unflawed virgin tubing,} \tag{1f}$$

R and h = mean radius and wall thickness of tube, respectively, (1g)

ν = Poisson's ratio, and (1h)

2c = axial crack length. (1i)

The crack opening area in the Zahoor model[16] for an axial throughwall crack in a thin-walled tube is given by

$$A = 2\pi c_e^2 V_o \sigma / E, \tag{2}$$

where

σ = hoop stress = pR/h,

p = differential pressure across tube wall,

E = Young's modulus,

R and h = mean radius and thickness of tube,

$$V_o = 1 + 0.64935\lambda_e^2 - 8.9683\text{x}10^{-3}\lambda_e^4 + 1.33873\text{x}10^{-4}\lambda_e^6,$$

$$\lambda_e^2 = c_e^2 / Rh,$$

$$c_e = c\left[1 + \frac{F}{2}\left(\frac{\sigma}{S_y}\right)^2\right],$$

$$F = 1 + 1.2987\lambda^2 - 2.6905\text{x}10^{-2}\lambda^4 + 5.3549\text{x}10^{-4}\lambda^6,$$

$$\lambda^2 = c^2 / Rh,$$

S_y = yield strength, and

c = crack half length.

The flaw opening area for an EDM notch can be estimated by adding the initial flaw area (= flaw length x flaw width) to the crack opening area given by Eq. 2. Crack opening areas calculated by Eq. 2 agree well with FEA results (Fig. 1).

3.1.2 Part-Throughwall Axial Cracks

A general failure criterion for predicting rupture of the crack tip ligament in a tube with a part-throughwall crack can be expressed as follows:

$$\sigma_{lig} = \bar{\sigma}, \tag{3a}$$

where σ_{lig} is the average ligament stress, which for the axial crack is given by

$$\sigma_{lig} = m_p\sigma\ , \tag{3b}$$

where m_p (which depends on the axial crack length and depth) is the ligament stress magnification factor, and σ is the nominal hoop stress (calculated using the mean radius and thickness of the tube including the sleeve, if any).

Various expressions for m_p of rectangular part-throughwall axial cracks are currently available.[1-4] For this report, we adopt the ANL correlation as described in Ref. 4 and reproduced below, because it provided the best correlation for the failure pressures of the tests conducted at Pacific Northwest National Laboratory (PNNL) on flawed steam generator tubes.[3,4]

$$m_p = \frac{1 - \alpha\frac{a}{mh}}{1 - \frac{a}{h}} \tag{4a}$$

$$\alpha = 1 + 0.9\left(\frac{a}{h}\right)^2\left(1 - \frac{1}{m}\right), \qquad (4b)$$

where a is crack depth.

Although Eqs. 3a-b and 4a-b can be used to estimate the crack tip ligament rupture pressure of rectangular part-throughwall cracks, they are not directly applicable to laboratory-grown and service-induced SCC cracks, which are irregular in shape and have variable depth along their length. Instead of being a single planar crack, they are composed of a family of crack segments in different planes. Local variations in crack depth and geometry are smoothed out in the EC measurements because the EC signals are necessarily averaged over a finite volume, and hence the EC data tend to show a relatively smooth variation of crack depth along the crack length (for example, see Fig. 2a-b). This is evidenced by the fact that although all the SCC specimens tested to date (including a "doped steam" cracked specimen supplied by Westinghouse) have shown leakage under low gas pressure before testing, the EC +Point method has failed to detect or identify the locations of these small pinholes. However, no leakage of water was detected through these cracks until much higher pressures were applied.

Currently, there are no widely accepted models available for predicting the ligament failure pressure of cracks with such complex geometries. From a limit analysis viewpoint, it can be argued that the collapse behavior of a crack tip ligament with an irregular point-by-point variation of crack depth should be similar to that of a crack with a smoothed-out "average" crack depth profile. For the present, we assume that the average profile measured by the EC +Point method is the one that is relevant for limit analysis. With this assumption, although the real crack may have short throughwall segments at a number of locations, from the viewpoint of plastic collapse of the ligament, the tube behaves as if it has a smoothly varying average ligament thickness (or crack depth) profile.

Since the measured crack depth profile by eddy current plus point is generally not rectangular (e.g., see Fig. 2a), the procedure described below was used to establish the length and depth of an equivalent rectangular crack.*

(1) Choose a crack depth d_o and assume that any crack segment with depth $d < d_o$ does not reduce the crack tip ligament rupture pressure of the tube (Fig. 2a) and can be ignored. In other words, replace the original crack depth profile by a new crack depth profile in which any crack segment with depth $d<d_o$ is replaced by $d = 0$ (Fig. 2b). The choice of d_o fixes the candidate equivalent rectangular crack length (L_o).

(2) The depth of the candidate equivalent rectangular crack is determined by equating its area to the area under the newly defined crack depth profile in step 1 (Fig. 2b). For example, in Figs. 2a-b, the choice of d_o = 50% fixes the length and depth of the candidate equivalent rectangular crack at 9 mm (0.35 in.) and 70%, respectively.

*Similar equivalent rectangular crack approaches have been used by others, e.g., see Report by Aptech Engineering Services, Inc., in Docket No. 50-361, Steam Generator Run Time Analysis for Cycle 9, San Onofre Nuclear Generating Station, Unit 2, September 25, 1997.

(3) Generate a series of candidate equivalent rectangular cracks by parametrically varying d_o and use the ANL correlation (Eqs. 3a-b and 4a-b) for calculating the ligament rupture pressures for all the candidates (Fig. 3).

(4) The equivalent rectangular crack corresponds to the crack with the lowest ligament rupture pressure (in Fig. 3, this equals 30 MPa (4.4 ksi), which corresponds to an equivalent crack length and depth of 9 mm (0.35 in.) and 70%, respectively).

Generally, a few trials for d_o were sufficient for cracks with relatively uniform ligament thickness as in specimen SGL-177 (Fig. 2a). This procedure can be automated by systematically choosing various candidate equivalent crack lengths L_o (instead of d_o), superimposing each crack length on the crack depth profile, and determining candidate equivalent crack depths by equating areas as before. The length of the equivalent rectangular crack, which corresponds to the minimum ligament rupture pressure, is used as an estimate for the length of the throughwall segment of the crack after ligament rupture.

3.2 Circumferential Cracks

3.2.1 Throughwall Circumferential Cracks

Failure loads of tubes with a single circumferential crack critically depend on the bending constraint imposed externally on the tubes. The two extreme cases are the free-bending case and the fully constrained case. In reality, steam generator tubes are partially constrained against bending by tube support plates.

3.2.1.1 Free Bending Case

Failure loads for tubing with through-wall circumferential cracks can also be calculated by plastic limit load (collapse) analyses, which were based on earlier work by Kanninen et al.[17] and are described by Ranganath and Mehta.[6] For an unconstrained (free-to-bend) tube with a through-wall crack of angular length 2θ and no applied primary bending stress, the critical failure pressure is

$$p_{cr} = \frac{2\bar{\sigma}h}{R}\left(1 - \frac{\theta}{\pi} - \frac{2\beta}{\pi}\right), \tag{5a}$$

where the angular location of the neutral axis is given by

$$\beta = \sin^{-1}\left(\frac{\sin\theta}{2}\right). \tag{5b}$$

3.2.1.2 Fully Constrained Case

Equation 5a is applicable to one extreme case, where the tube is completely free to bend. In the opposite extreme case of total constraint against bending, a criterion based on maximum shear stress in the net section, as proposed by Cochet et al.,[18] can be used to calculate the instability limit pressure:

$$p_{cr} = \frac{2(\gamma^2 - 1)(\pi - \theta)\bar{\sigma}}{2\pi + (\pi - \theta)(\gamma^2 - 1)}, \tag{6a}$$

where

$$\gamma = \frac{R_o}{R_i}, \tag{6b}$$

where R_o and R_i are the outer and inner radius, respectively. Equation 6c, which is a thin-shell uniaxial approximation to Eq. 6a, is often used to predict failure of steam generator tubes that are fully constrained against bending:

$$p_{cr} = \frac{2\bar{\sigma}h}{R}\left(1 - \frac{\theta}{\pi}\right). \tag{6c}$$

In reality, the tube support plates offer significant but not total restraint against bending, a circumstance that tends to increase the failure pressure to somewhere between those predicted by Eq. 5a and those of Eqs. 6a (or 6c).

3.2.1.3 Partially Constrained Case

Consider a tube of mean radius R, wall thickness h, and length L, containing a throughwall circumferential flaw of angular length 2θ at any axial location. The tube can be subjected to various edge conditions. For example, the tube may be clamped at one end (simulating the tubesheet) and simply supported at the other end (simulating the first tube support plate). Figure 4 shows such a tube with the crack located at the top of tube sheet. Under internal pressure loading, finite-element analysis shows that a tube in the configuration of Fig. 4 deforms as shown in Fig. 5 with a definite crack flank rotation and crack tip opening displacement. In this report, limit load analysis will be used to estimate failure pressure of tubes made of ductile materials like Alloy 600.

We assume that the tube is thin and is under internal pressure loading only (no constraint on axial deformation of the tube), and that the onset of crack extension occurs after the attainment of the limit state. The last assumption is valid provided that the Battelle Screening Criterion[19] is satisfied, i.e.,

$$\frac{E\delta_c}{R\bar{\sigma}}\left(1 - \frac{\theta}{\pi}\right) \geq 1, \tag{7}$$

where δ_c is the critical crack tip opening displacement. Thus, for alloy 600 steam generator tubing with E = 30,000 ksi, $\bar{\sigma}$ = 70 ksi, R=0.4 in., and 2θ= 270°, $\delta_c \geq 0.004$ in., which is generally satisfied by all ductile alloys.

The stress distribution through the section containing the crack at the limit-state is shown in Fig. 6. We further assume that plastic deformation is limited to only the section containing the crack while the rest of the tube responds elastically.

The bending moment (about the tube centerline) and axial force equilibria of the stress distribution of the limit-state (Fig. 6) give the following:

$$M_L = 4\bar{\sigma}R^2h\left(\frac{1}{2}\sin\theta - \sin\beta\right) \tag{8a}$$

and

$$\beta = \frac{\pi-\theta}{2} - \frac{P}{4\bar{\sigma}Rh} = \frac{\pi-\theta}{2} - \frac{\pi pR}{4\bar{\sigma}h} \tag{8b}$$

or

$$\frac{p}{p_b} = \frac{pR}{\bar{\sigma}h} = 2\left(1-\frac{\theta}{\pi}\right) - \frac{4\beta}{\pi}, \tag{8c}$$

where β defines the location of the plastic neutral axis, p is the internal pressure, p_b is the burst pressure of an unflawed tube.

Plasticity Confined to Crack Section. Denoting the calculated bending moment (positive counterclockwise in Fig. 4) in an undefected tube at the crack location (z=0) by M (for internal pressure loading, M=0) and by considering the equilibrium of the bending moment in the elastic part of the tube just to the left of the crack section with the limit moment acting on the crack section (see Fig. 4),

$$M = -M_L + \frac{3EI\phi}{L} = 0, \tag{9a}$$

where I is the bending moment of inertia (πR^3h), and Φ is the rotation at the cracked section due to crack opening (Fig. 4). Equation 9a is applicable for the configuration shown in Fig. 4. It can be generalized for any set of edge conditions and crack locations by using an effective length L_e. The generalized version of Eq. 9a is as follows:

$$M = -M_L + \frac{EI\phi}{L_e} = 0. \tag{9b}$$

Relationships between L and L_e for several crack locations and edge conditions are given in Table 1. The plastic rotation Φ_c about the neutral axis at the onset of crack extension is related to the critical crack tip opening displacement δ_c by the expression

$$\phi_c = \frac{\delta_c}{R(\cos\beta + \cos\theta)}. \tag{10}$$

Combining Eqs. 8a, 9b, and 10 at the point of crack initiation,

$$\left(\tfrac{1}{2}\sin\theta - \sin\beta\right)(\cos\beta + \cos\theta) - c = 0, \tag{11a}$$

where

$$c = \frac{\pi E \delta_c}{4 L_e \bar{\sigma}}. \tag{11b}$$

Equation 11a can be solved for the critical value $\beta = \beta_c$ which when substituted in Eq. 11b gives the crack initiation pressure p_c. Note that the equation for the free-bending case can be obtained by setting $L_e = \infty$, i.e., c=0 in Eq. 11a.

The onset of crack extension can also be expressed in terms of the critical value of the plastic component of the deformation J integral J_P which, for the bending case, is defined in terms of the plastic rotation ϕ as follows:

$$J_P = -\int_0^{\phi} \left(\frac{\partial M}{\partial A}\right)_{\phi} d\phi\ , \tag{12}$$

where A = 2Rhθ. In the context of limit analysis $J = J_P$ and $M = M_L$ as given in Eq. 8a. Differentiating Eq. 8a with respect to θ and noting from Eq. 8b that at constant rotation, i.e., at constant pressure,

$$\frac{\partial \beta}{\partial \theta} = -\frac{1}{2}.$$

$$J = R\bar{\sigma}\int_0^{\phi} (\cos\beta + \cos\theta) d\phi = R\bar{\sigma}\phi(\cos\beta + \cos\theta). \tag{13}$$

Thus, the critical plastic rotation is given in terms of the critical J integral J_c as follows:

$$\phi_c = \frac{J_c}{R\bar{\sigma}(\cos\beta + \cos\theta)}. \tag{14a}$$

Comparing Eqs. 10 and 14a, we recover the familiar equation

$$J_c = \bar{\sigma}\delta_c. \tag{14b}$$

The toughness parameter c is related to the fracture toughness parameter K_{JC} ($K_{JC} = \sqrt{E J_C}$) by (using Eqs. 11b and 14b)

$$c = \frac{3\pi}{4L}\left(\frac{K_{JC}}{\bar{\sigma}}\right)^2. \tag{14c}$$

A plot of the fracture toughness K_{JC} versus the critical crack tip opening displacement is shown in Fig. 7. For ductile alloys, the critical crack tip displacement is somewhere in the range of 0.03 in. - 0.1 in.

Unstable failure need not necessarily be associated with onset of crack extension. If the crack is to be unstable at onset of crack extension under constant loading, the following condition must be satisfied (by using Eq. 9b):

$$\frac{dM}{d\phi} = \left.\frac{dM_L}{d\phi}\right|_I + \frac{EI}{L_e} < 0 \ , \tag{15}$$

with $\left.\frac{dM_L}{d\phi}\right|_I$ being measured at the onset of crack extension. Eq. 15 can be expressed in terms of the familiar tearing modulus by first differentiating Eq. 13 with respect to θ,

$$\frac{dJ}{d\theta} = \frac{\partial J}{\partial \theta} + \frac{\partial J}{\partial \phi}\frac{d\phi}{d\theta} = R\bar{\sigma}\left[-\phi\left(\sin\theta - \frac{1}{2}\sin\beta\right) + \frac{d\phi}{d\theta}(\cos\beta + \cos\theta)\right] \tag{16a}$$

and then solving

$$\frac{d\phi}{d\theta} = \frac{\dfrac{dJ}{d\theta} + J\dfrac{\sin\theta - \frac{1}{2}\sin\beta}{\cos\beta + \cos\theta}}{R\bar{\sigma}(\cos\beta + \cos\theta)} \ . \tag{16b}$$

Differentiating Eq. 8a with respect to φ, using Eq. 16b, and rearranging, we obtain the condition of instability as

$$\frac{2L_e}{\pi R}(\cos\beta + \cos\theta)^2 - \frac{EJ}{R\bar{\sigma}^2}\frac{\sin\theta - \frac{1}{2}\sin\beta}{\cos\beta + \cos\theta} > \frac{E}{\bar{\sigma}^2}\frac{dJ}{da} \ , \tag{17a}$$

where a is the crack length (Rdθ = da). We can identify the left-hand-side of Eq. 17a as the applied tearing modulus, T_{APP}, and the condition of instability can be written as

$$T_{APP} \equiv \frac{2L_e}{\pi R}(\cos\beta + \cos\theta)^2 - \frac{EJ}{R\bar{\sigma}^2}\frac{\sin\theta - \frac{1}{2}\sin\beta}{\cos\beta + \cos\theta}$$

$$> \frac{E}{\bar{\sigma}^2}\frac{dJ}{da} = T_{MAT} \ . \tag{17b}$$

Note that Eq. 17b is the same as that given by Smith.[11] For ductile materials with high crack growth resistance, the J-term is usually negligible. In such cases, we can simplify Eq. 17b as

$$T_{APP} \approx \frac{2L_e}{\pi R}(\cos\beta + \cos\theta)^2 > T_{MAT} \ . \tag{17c}$$

For many ductile alloys, $T_{MAT} \approx 200$.

Onset of yielding away from the crack plane can be calculated by using the current model and assuming a loading path consisting of first applying the membrane stresses due to pressure, keeping the bending stresses at zero, and then applying the bending stresses while

holding the membrane stresses constant. Although the axial bending analysis in the current model is uniaxial, the axial yield stress S_y is adjusted to account for the biaxial stress effect by assuming it vary with the hoop stress σ_h as follows (Fig. 8a):

$$S_y = \begin{cases} \sigma_y - \dfrac{\sigma_h}{2} & \text{for } \sigma_h \le \sigma_y \\ \dfrac{\sigma_y}{2} & \text{for } \sigma_h > \sigma_y \end{cases}. \tag{18}$$

where σ_y is the virgin uniaxial yield stress. If we denote the bending moment to cause first yielding in an uncracked section just adjacent to the cracked section by M_y,

$$M_y = \frac{S_y I}{R} \tag{19a}$$

and Eq. 8a can be written in a nondimensional form as follows:

$$\frac{M_L}{M_y} = \frac{4}{\pi}\frac{\bar{\sigma}}{S_y}\left(\frac{1}{2}\sin\theta - \sin\beta\right). \tag{19b}$$

Thus, the condition for first yielding in an undefected section just adjacent to the cracked section by bending is:

$$\frac{M_L}{M_y} = \frac{4}{\pi}\frac{\bar{\sigma}}{S_y}\left(\frac{1}{2}\sin\theta - \sin\beta\right) = 1. \tag{20a}$$

Noting that yielding of the undefected tube section can occur by either axial bending or yielding in the hoop direction by membrane hoop stress, we see that the pressure to cause first yielding (denoted by p_y) is the lesser of the following two:

$$\frac{p_y}{p_b} = \begin{cases} \dfrac{2\sigma_y}{\bar{\sigma}} - \dfrac{8}{\pi}\left(\dfrac{1}{2}\sin\theta - \sin\beta\right) \\ \dfrac{\sigma_y}{\bar{\sigma}} \end{cases}. \tag{20b}$$

Since β is a function of pressure (Eq. 8b), Eq. 20b must be solved numerically. A plot of the pressure to first yield versus crack length is shown in Fig. 8b for various values of yield to flow stress ratios.

To provide a basis for comparison with the analytical models, an incremental elastic-plastic FEA using a multilinear kinematic hardening rule was conducted for a tube (L/R=60, simply supported at one end and clamped at the other) with a 240° throughwall circumferential crack at the clamped end under internal pressure loading. The assumed stress-strain curve is shown in Fig. 9. The difference between kinematic and isotropic hardening rules should be small for the near-radial loading path used for the problem at hand. Comparisons of the variation of the crack section rotation and support reaction with pressure are shown in Figs. 10a-b, respectively. The slight discrepancy between the FEA results and the model predictions at low pressures are due to neglect of elastic deformation in the model. However, the FEA results diverge from the model calculations significantly as the pressure

exceeds approximately one-half of the unflawed tube burst pressure. This is because at these higher pressures, tube sections away from the crack plane experience significant plastic deformation, which is assumed to be negligible in the model. Note that with $\sigma_y/\bar{\sigma}$ =0.5, the analytical model predicts (Fig. 8b) onset of yielding in a tube containing a 240° crack at p/p_b =0.43, which agrees very well with the FEA result (Fig. 10a). Thus, the limit of applicability of the current model depends on the crack angle, as well as on the strain-hardening behavior ($\sigma_y/\bar{\sigma}$) of the material (Fig. 8b).

Plasticity Allowed to Occur Away from Crack Section. When plasticity spreads to sections other than that containing the crack, Eq. 9a is no longer applicable and a new nonlinear relationship between bending moment and rotation must be derived. A material with a power-law hardening stress-strain curve is considered:

$$\frac{\varepsilon}{\varepsilon_y} = \begin{cases} \frac{\sigma}{\sigma_y} & \text{for } \sigma \le \sigma_y \\ \left(\frac{\sigma}{\sigma_y}\right)^{\frac{1}{m}} & \text{for } \sigma > \sigma_y \end{cases} \quad (21)$$

We continue to assume that the section containing the crack is at plastic limit state with flow stress H, the assumption being that the crack section experiences extensive plastic deformation long before any plastic yielding occurs away from the crack section.

To keep the analysis tractable for the current analytical model, we make a simplifying assumption that the stresses and total deformation at any pressure can be obtained by considering a nonradial loading path, consisting of first loading radially to the final pressure (hoop to axial membrane stress ratio of 2 to 1) at zero axial bending stress and then applying the axial bending stresses while holding the pressure-induced membrane stresses constant (Fig. 11). This assumption allows us to use the same yield surface (Eq. 18, Fig. 8a) for all axial locations and to obtain an analytical solution for the bending problem. The relatively good agreement between the model prediction and the FEA results, to be discussed later, shows that this assumption is probably reasonable as long as no unloading or reversed yielding occurs.

With the above assumptions, we determine a relationship between the bending moment and rotation in the elastic-plastic regime by a detailed analysis of axial bending of the tube subjected to an end moment M_o at a constant internal pressure p. For $p>p_y$, a length of the tube extending from z = 0 to $z = z_y$ will deform plastically, while the rest of the beam $L>z>z_y$ will remain elastic. The stress distribution in a plastically deforming section is shown in Fig. 12. At every section, there will be an elastic core extending from $\theta = -\beta_y$ to $\theta = \beta_y$, with β_y ranging from $\beta_y = \beta_o$ at z = 0 to $\beta_y = \pi/2$ at $z = z_y$.

By stress integration and using the definition of zy, the bending moment at any section is given by

$$\frac{M}{M_y} = \frac{2}{\pi \sin\beta_y}\left(\beta_y - \frac{1}{2}\sin 2\beta_y\right) + \frac{4}{\pi}\left(\frac{1}{\sin\beta_y}\right)^m \int_{\beta_y}^{\frac{\pi}{2}} \sin^{m+1}\theta d\theta = \frac{L-z}{L-z_y}, \quad (22)$$

where M_y corresponds to the bending moment at first yield away from crack section.

Differentiating Eq. 22 and solving,

$$\frac{d\beta_y}{dz} = \frac{1}{(L - z_y)} \frac{1}{f(\beta_y)}, \tag{23}$$

where

$$f(\beta_y) = \frac{2}{\pi}\left(\frac{\beta_y - \frac{1}{2}\sin 2\beta_y}{\sin\beta_y \tan\beta_y} + \frac{2mI_m}{\sin^m \beta_y \tan\beta_y} \right) \tag{24}$$

$$I_m = \int_{\beta_y}^{\frac{\pi}{2}} \sin^{m+1}\theta d\theta. \tag{25}$$

The equation for bending is given by

$$\frac{d^2w}{dz^2} = -\frac{\kappa_y}{\sin\beta_y}, \tag{26a}$$

where w is the transverse deflection and

$$\kappa_y = \frac{M_y}{EI} = \frac{S_y}{ER}. \tag{26b}$$

Making a transformation of independent coordinate from z to β_y with the help of Eq. 23,

$$\frac{dw}{dz} = \frac{1}{(L - z_y)} \frac{1}{f(\beta_y)} \frac{dw}{d\beta_y} \tag{27a}$$

and

$$\begin{aligned} \frac{d^2w}{dz^2} &= \left[\frac{1}{(L - z_y)} \right]^2 \frac{1}{f(\beta_y)} \frac{d}{d\beta_y} \left[\frac{1}{f(\beta_y)} \frac{dw}{d\beta_y} \right] \\ &= -\frac{\kappa_y}{\sin\beta_y}. \end{aligned} \tag{27b}$$

Integrating Eq. 27b from $\beta = \beta_o$ (i.e., z = 0) to $\beta = \pi/2$ (i.e., $z = z_y$), and denoting the slope at z = 0 by ϕ_o,

$$\left.\frac{dw}{dz}\right|_{z=z_y} = \phi_o - \kappa_y (L - z_y) \int_{\beta_o}^{\frac{\pi}{2}} \frac{f(\beta_y)}{\sin\beta_y} d\beta_y. \tag{28a}$$

In a similar fashion,

$$w|_{z=z_y} = \phi_o\left((L-z_y)\int_{\beta_o}^{\frac{\pi}{2}} \frac{f(\beta_y)}{\sin\beta_y} d\beta_y - \kappa_y (L-z_y)^2 \int_{\beta_o}^{\frac{\pi}{2}} f(\beta_y)\int_{\beta_o}^{\beta_y} \frac{f(\beta_y)}{\sin\beta_y} d\beta_y d\beta_y\right). \quad (28b)$$

The slope and displacement at $z = z_y$ from the elastic part of the beam are

$$\left.\frac{dw}{dz}\right|_{z=z_y} = \frac{M_y(L-z_y)}{2EI} + C_1 \quad (29a)$$

and

$$w|_{z=z_y} = -\frac{M_y}{6EI}(L-z_y)^2 - C_1(L-z_y), \quad (29b)$$

where C_1 is an arbitrary constant. Combining Eqs. 29a and 29b,

$$(L-z_y)\left.\frac{dw}{dz}\right|_{z_y} + w|_{z_y} = \frac{\kappa_y}{3}(L-z_y)^2. \quad (29c)$$

Satisfying continuity of slope and displacement at $z = z_y$, using Eq. 29c, and solving gives

$$\frac{\phi_o M_o}{\phi_y M_y} = \frac{3I_1 + 3I_2 + 1}{1 + I_3}, \quad (30)$$

where

$$\frac{M_o}{M_y} = \frac{2}{\pi \sin\beta_o}\left(\beta_o - \frac{1}{2}\sin 2\beta_o\right) + \frac{4}{\pi}\left(\frac{1}{\sin\beta_o}\right)^m \int_{\beta_o}^{\frac{\pi}{2}} \sin^{m+1}\theta d\theta \quad (31a)$$

$$\phi_y = \frac{1}{3}L\kappa_y = \frac{M_y L}{3EI}, \quad (31b)$$

$$I_1 = \int_{\beta_o}^{\frac{\pi}{2}} \frac{f(\beta_y)}{\sin\beta_y} d\beta_y, \quad (31c)$$

$$I_2 = \int_{\beta_o}^{\frac{\pi}{2}} f(\beta_y)\int_{\beta_o}^{\beta_y} \frac{f(\beta_y)}{\sin\beta_y} d\beta_y d\beta_y, \quad (31d)$$

and

$$I_3 = \int_{\beta_o}^{\frac{\pi}{2}} f(\beta_y) d\beta_y. \quad (31e)$$

We can represent the rotation in terms of a function G of the bending moment as follows, with the exponent m as a parameter,

$$\phi = \phi_y G\left(\frac{M}{M_y}; m\right). \tag{32a}$$

A plot of the calculated end rotation versus the applied moment is shown in Fig. 13a. The function G can be represented by a cubic polynomial of the bending moment (see Fig. 13a):

$$G(x) = \begin{cases} x & \text{for } x \le 1 \\ A + Bx + Cx^2 + Dx^3 & \text{for } x > 1. \end{cases} \tag{32b}$$

Equation 9a can be generalized for the elastic-plastic case as follows:

$$-\frac{M_L}{M_y} + G^{-1}\left(\frac{\phi}{\phi_y}\right) = 0 \tag{33a}$$

or, alternatively

$$\phi = \phi_y G\left(\frac{M_L}{M_y}\right). \tag{33b}$$

Figure 13b shows a plot of crack section rotation with pressure for a tube (L/R=60, simply supported at one end and clamped at the other) with a 240° throughwall circumferential crack at the clamped end under internal pressure loading and using a power-law hardening stress-strain curve (Fig. 9). As expected, the model that allows for plasticity to occur away from crack plane fits the FEA data better than that in which plasticity is confined to the crack plane (Fig. 10a).

Combining Eqs. 33b and 10, at the point of crack initiation,

$$(\cos\beta_c + \cos\theta) G\left(\frac{M_L}{M_y}\right) = \frac{3E\delta_c}{LS_y} = \frac{3\pi E\delta_c}{4L\bar{\sigma}} \frac{4}{\pi} \frac{\bar{\sigma}}{S_y}$$

$$= \frac{4c}{\pi} \frac{\bar{\sigma}}{S_y}, \tag{34a}$$

where M_L/M_y is given by Eq. 19b, c is defined in Eq. 11b, and Eq. 18 can be rewritten as follows:

$$\frac{S_y}{\bar{\sigma}} = \begin{cases} \frac{\sigma_y}{\bar{\sigma}} - \frac{p}{2p_b} & \text{for } \frac{p}{p_b} \le \frac{\sigma_y}{\bar{\sigma}} \\ \frac{p}{2p_b} & \text{for } \frac{p}{p_b} > \frac{\sigma_y}{\bar{\sigma}}. \end{cases} \tag{34b}$$

Equation 34a can be solved for the critical value $\beta = \beta_c$, which when substituted in Eq. 8b, gives the crack initiation pressure p_c.

Onset of crack extension can also be expressed in terms of the critical value J_c of the plastic component of the deformation J integral J_P, and Eqs. 12, 13, and 14a-b still hold.

Proceeding as before, if the crack is to be unstable at onset of crack extension under constant loading, the following condition must be satisfied (using Eq. 33a):

$$\frac{dM}{d\phi} = -\frac{dM_L}{d\phi}\bigg|_I + \frac{3EI}{L}\frac{dG^{-1}\left(\frac{\phi}{\phi_y}\right)}{d\left(\frac{\phi}{\phi_y}\right)} = -\frac{dM_L}{d\phi}\bigg|_I + \frac{3EI}{L}\frac{1}{\left.\frac{dG\left(\frac{M}{M_y}\right)}{d\left(\frac{M}{M_y}\right)}\right|_{M=M_L}} < 0, \tag{35}$$

where $\frac{dM_L}{d\phi}$ is measured at the onset of crack extension. Using Eqs 16a and 16b and following the procedure that was used to derive Eq. 17b, the condition for unstable failure is

$$T_{APP} \equiv \frac{2L}{3\pi R}(\cos\beta + \cos\theta)^2 \left.\frac{dG\left(\frac{M}{M_y}\right)}{d\left(\frac{M}{M_y}\right)}\right|_{M=M_L} - \frac{EJ}{R\bar{\sigma}^2}\frac{\sin\theta - \frac{1}{2}\sin\beta}{\cos\beta + \cos\theta}$$

$$> \frac{E}{\bar{\sigma}^2}\frac{dJ}{da} = T_{MAT}\ . \tag{36}$$

Variation of the normalized failure pressure (onset of crack extension) with crack angle is shown in Fig. 14a for various values of c when plasticity is confined to the crack plane. A conservative value of c for an Alloy 600 steam generator tube in a PWR is 0.2; more typically, it would be in the range of 0.5-1. Figure 14a shows that all such tubes would behave as if fully constrained. Thus, the burst pressure of a tube with a throughwall crack of ≤180° is the same as the burst pressure of an unflawed tube. Also shown in Fig. 14a are the expected differential pressures during normal operation and design-basis accident conditions. The maximum throughwall crack lengths that will not propagate during normal operation and design-basis accidents in PWRs are 340° and 315°, respectively. Note that a free-bending assumption would be much more conservative, because the corresponding allowable crack lengths would be 225° and 200°.

Similar variation of the normalized failure pressure with crack angle is shown in Fig. 14b for the case when plastic yielding is allowed to occur away from the crack plane. Because the value of c is in the range of 0.5-1, the occurrence of plasticity away from the crack plane is not a concern in PWRs. However, laboratory leak rate and failure tests on circumferentially cracked tubes, such as those reported in Ref. 20, generally involve significant plastic deformation away from the crack plane. In Ref. 20, failure curves based on tests that were performed on circumferentially cracked steam generator tubes are similar to those in Fig. 14b. Note that the minimums observed in the failure curves in Fig. 14a are generally absent in Fig. 14b.

The calculated tearing-modulus-vs.-pressure plot (Fig. 15) shows a marked increase in tearing modulus with pressure for shorter cracks (≤180°), indicating that the driving force for crack instability, which is negligible as long as plasticity is confined to the crack plane, increases rapidly with plastic yielding away from the crack plane. This is to be expected

because the loss of bending stiffness of the tube with plastic yielding produces a higher elastic follow-up, which causes the tube to behave like one with a much longer effective span. However, even with the enhanced values of T_{APP}, tubes with longer cracks (≥240°) may not fail by unstable tearing at the onset of crack extension (T_{MAT} for ductile alloys such as Alloy 600 is typically ≈200) and will very likely fail by plastic collapse after some stable crack growth. Because at values of c that are typical for steam generator tubes (0.5 to 1), the pressure for onset of crack extension (Fig. 14b) is already close to the pressure that corresponds to the fully constrained case, the extent of stable crack growth should be small.

3.2.1.4 Crack Opening Area

Because in the current model, we assume rigid-perfectly plastic behavior of the crack section, the crack remains closed (i.e., crack opening area (COA) = 0) until the section containing the crack reaches the limit state, i.e., pressure exceeds the critical pressure for an unconstrained tube. After the crack section reaches the limit state, the bending moment acting on it can increase (along with flexing of the tube) by a shift of the plastic neutral axis (i.e., decreasing β) until β = 0, at which point the crack section behaves as if fully constrained and the maximum pressure capability, which corresponds to net section yielding, is achieved. If the critical crack tip opening displacement is not exceeded and there is no crack extension, the COA can be calculated from the rotation φ and crack size by solving

$$A = 2R^2\phi\int_0^{\theta}(\cos\beta + \cos\alpha)d\alpha = 2R^2\phi(\theta\cos\beta + \sin\theta)\ . \tag{37a}$$

At the point of crack initiation, $\phi = \phi_c$ and $\beta = \beta_c$, which when substituted into Eq. 37a, and with the aid of Eq. 10, gives

$$A = A_c = 2R\delta_c\frac{(\theta\cos\beta_c + \sin\theta)}{(\cos\beta_c + \cos\theta)}. \tag{37b}$$

To obtain the COA over the full pressure range from zero to failure pressure, the COA due to the elastic and elastic-plastic deformation of the crack section prior to reaching the limit state must be included. We used the Paris/Tada model[21] for this purpose. Being restricted to small scale yielding, this model nicely complements the current model which is applicable after the crack section reaches plastic limit state. The COA in the small pressure regime below the range of applicability of the current model can be calculated by using the following equation due to Paris and Tada:

$$A = \frac{\pi pR^2}{E}B, \tag{38a}$$

where

$$B = \begin{cases} \lambda_e{}^2 + 0.16\lambda_e{}^4 \text{ for } 0 \le \lambda_e \le 1 \\ 0.02 + 0.81\lambda_e{}^2 + 0.30\lambda_e{}^3 + 0.03\lambda_e{}^4 \text{ for } 1 \le \lambda_e \le 5 \end{cases} \tag{38b}$$

$$\lambda_e = \theta_e\left(\frac{R}{h}\right)^{0.5} \tag{38c}$$

$$\theta_e = \theta\left[1 + F_m^2 p^2 R^2 / \left(8h^2\sigma_y^2\right)\right] \tag{38d}$$

$$F_m = \begin{cases} 1 + 0.1501\lambda^{1.5} \text{ for } \lambda \le 2 \\ 0.8875 + 0.2625\lambda \text{ for } 2 \le \lambda \le 5 \end{cases} \tag{38e}$$

$$\lambda = \theta\left(\frac{R}{h}\right)^{0.5}. \tag{38f}$$

It should be noted that the Paris/Tada model is restricted to small-scale yielding ($\lambda \le 5$) and does not account for the bending effects that become important at pressures that induce large-scale plasticity in the crack plane. As a result, the COA calculated by this model is independent of the span of the tube or support conditions.

Crack opening areas for a 240° crack, calculated by the current model and by the Paris/Tada model, are shown in Fig. 16. It is assumed that onset of crack extension does not occur before maximum pressure is reached. In Fig. 16, the curve labeled $L = \infty$ corresponds to the free-bending case, whereas the curve labeled $L = 0$ corresponds to the fully constrained case. Results from the Paris/Tada model, which is restricted to small-scale yielding in the crack plane and is independent of the span L, are plotted up to pressure levels significantly above the range of applicability. It is evident that lateral restraint to bending significantly reduces the COA when compared with the tube cross-sectional area, even under a design-basis accident condition ($p/p_b \approx 0.25$).

3.2.2 Part-Throughwall Circumferential Cracks

Consider a tube with mean radius R and wall thickness h and containing either two symmetrical part-through circumferential cracks (Fig. 17a) or a single part-through circumferential crack (Fig. 17b) of angular length 2θ and depth a. At low temperatures, where creep effects are negligible, the ligament failure pressure (p_{sc}) is generally expressed in terms of a stress magnification factor (m_p) by equating the magnified axial stress in the ligament to the flow stress,

$$\sigma_{lig} = m_p \frac{p_{sc} R}{2h} = \bar{\sigma}. \tag{39}$$

Failure pressure for circumferentially cracked tubes, i.e., the value of the magnification factor m_p, depends strongly on the degree of restraint the tubes are subjected to against bending. The two extreme cases, i.e., the free-bending case and the completely constrained case are relatively easy to analyze. Generally, steam generator tubes are sufficiently constrained laterally that failure loads are expected to be much closer to the completely constrained case than the free-bending case. The discussion here assumes that the tubes are either completely constrained or are completely free to bend.

3.2.2.1 Fully Constrained Case

The fully constrained case also includes the case for an unrestrained tube that contains two symmetrical cracks (Fig. 17a). In this situation, the whole section that contains the crack (or cracks) is subjected to axial tensile stress, with the ligament (or ligaments) subjected to

stress intensification. If the average stress in the ligament (or ligaments) is expressed as 1/m times the average stress in the rest of the section that contains the crack (or cracks), the average ligament axial stress (σ_{lig}) can be calculated from a simple equilibrium of axial forces,

$$\sigma_{lig} = \frac{pR}{2h}\frac{1}{\left[m+\left(\frac{n\theta}{\pi}\right)\left(1-\frac{a}{h}-m\right)\right]}, \tag{40a}$$

where

$$n = \begin{cases} 1 \text{ for a single crack} \\ 2 \text{ for two symmetrical cracks.} \end{cases}$$

If we define m_p as the ratio of the average ligament axial stress and the average axial stress in the unflawed tube, m_p is given by

$$m_p = \frac{1}{\left[m+\left(\frac{n\theta}{\pi}\right)\left(1-\frac{a}{h}-m\right)\right]}. \tag{40b}$$

Originally, Kurihara et al.[22] used the empirically obtained expression

$$m = 1-\left(\frac{a}{h}\right)^{\kappa}\left(\frac{n\theta}{\pi}\right)^{\mu}, \tag{41}$$

(with n =1).

Although Kurihara et al.[22] recommended values of κ = 2 and μ = 0.2 for the exponents, the results are almost indistinguishable from those obtained by using κ = 3 and μ = 0.3. Because the behavior of Eq. 41 is not correct (i.e., m does not tend to 0) when a/h tends to 1 for all θ, it was modified to have the same form as in the case of axial cracks, i.e.,

$$m = \frac{1-\frac{a}{h}}{1-\frac{a}{Nh}}, \tag{42a}$$

where

$$N = 1+\lambda\left(\frac{n\theta}{\pi}\right)^{\gamma} \tag{42b}$$

and λ and γ are fitting parameters.

Both the failure modes and moments of the original set of test data from four-point bending failure tests on pressurized part-through circumferentially cracked Type 304 stainless steel pipes at room temperature (used by Kurihara et al.[22]) can be predicted somewhat better by the current model with λ = 0.2 and γ = 0.2 than by the Kurihara model (see Figs. 18a and

b). This approach led to reasonable predictions of failure temperatures of tubes with two symmetrical part-through circumferential notches subjected to high temperature ramps.[4]

3.2.2.2 Free-Bending Case

Figure 17b shows that in the free-bending case, part of the section that contains the crack will generally be subjected to compressive stress. As a result, Eq. 39a must be replaced by

$$\sigma_{lig} = \frac{pR}{2h}\frac{1}{\left[m\left(1-\frac{2\beta}{\pi}\right)+\left(\frac{n\theta}{\pi}\right)\left(1-\frac{a}{h}-m\right)\right]}, \tag{43a}$$

where the angle β that defines the location of the neutral axis is given by

$$\beta = \sin^{-1}\left\{\frac{\sin\theta}{2}\left[1-\frac{1}{m}\left(1-\frac{a}{h}\right)\right]\right\} \text{ for } \beta \le \pi - \theta, \tag{43b}$$

and Eq. (40b) must be replaced by

$$m_p = \frac{1}{\left[m\left(1-\frac{2\beta}{\pi}\right)+\left(\frac{n\theta}{\pi}\right)\left(1-\frac{a}{h}-m\right)\right]}, \tag{43c}$$

with m and N defined by Eqs. 42a and 42b, respectively. This approach led to reasonable predictions of failure temperatures of free-to-bend tubes with a part-through circumferential notch subjected to high temperature ramps.[4]

3.2.2.3 Partially Constrained Case

Although a detailed analysis comparable to that presented in Subsection 3.2.1.3 has not been carried out for the part-throughwall crack, it is expected that for typical steam generators in PWRs, tubes with part-throughwall circumferential cracks at the top of tube sheet will behave as if they were fully constrained against bending.

3.3 Leak Rate Model

Leak rate tests on 7/8-in. (22 mm)-diameter Alloy 600 tubes containing throughwall axial EDM notches and SCC cracks are being conducted on both as-received and heat-treated materials. The heat treatment, which is used to accelerate production of stress corrosion cracks in the laboratory, requires a solution treatment at 1100°C followed by a sensitizing treatment at 700°C, which reduce the yield strength of the tube from 43 to 26 ksi (300 to 180 MPa). Such a reduction in yield strength will have a significant influence on the crack opening area and, hence, on the leak rate. Therefore, we will first investigate the predictive capability of the standard smooth orifice leak rate equation for the leak rate tests conducted on as-received and heat-treated specimens with EDM notches.

The formula used to calculate the volumetric leak rate Q is

$$Q = 0.6A\sqrt{\frac{2\Delta p}{\rho}} \tag{44a}$$

or, using conventional units,

$$Q = 180.2A\sqrt{\frac{\Delta p}{\rho}}\ , \tag{44b}$$

where A is the flaw opening area in $in.^2$, Δp is the pressure differential across the tube wall in psi, and ρ is the density (62.4 lb/ft^3 [1000 kg/m^3] at RT and 45.9 lb/ft^3 [735 kg/m^3] at 282°C). In contrast to a circular hole, whose area remains relatively constant under increasing pressure, the area of a crack or a notch increases with pressure and must be taken into account when calculating the leak rate. Crack opening areas were calculated by the Zahoor model, which is described in Subsection 3.1.1.

4 Pressure and Leak Rate Tests

The Pressure and Leak Rate Test Facility at ANL is being used to obtain data on failure pressures, failure modes, and leak rates of flawed SG tubes at temperatures up to 343°C (650°F), pressures of up to 21 MPa (3000 psi), and pressurized-water flow rates of up to 1520 L/min (400 gpm).[23] Reference 23 includes a brief description of the facility. A second High-Pressure (room-temperature water) Test Facility with a working pressure of 52 Mpa (7.5 ksi) and a maximum sustainable flow rate of up to 47.5 L/min (12.5 gpm) has also been constructed. Specimens with short notches and stress corrosion cracks that cannot be tested to unstable burst in the Pressure and Leak Rate Test Facility are tested to unstable burst in the High Pressure Test Facility using an internal bladder.

4.1 Tests on Machined (EDM) Notches

The purpose of these tests is to fill in the gaps in the existing data base, which is relatively sparse in short and deep flaws, and to validate the ANL ligament rupture criterion for both short and long flaws with various depths. Pressure and leak rate tests were conducted at room temperature and 282°C on specimens with machined (EDM) notches of lengths ranging from 6 mm (0.25 in.) to 38 mm (1.5 in.). Notch depth ranged from 100% throughwall to 90, 80 and 60% part-throughwall. To determine the effect of heat treatment (used to produce stress corrosion cracks in the laboratory) on failure pressure and leak rate, notched specimens were tested in as-received and heat-treated conditions. A few tests with two axially aligned notches were also conducted. A summary of all tests completed to date on notched specimens is given in Table 2. Note that the last seven tests in Table 2 were conducted at the High Pressure Test Facility and include specimens with relatively short and deep notches. Additional tests with short and deep notches and multiple notches will be carried out in the future.

4.1.1 Predicted Failure Pressures

Failure pressures are predicted by using Eqs. 4a and 1a for ligament rupture of part-throughwall cracks and unstable burst of throughwall cracks, respectively. Based on limited tensile tests, the flow stress properties for the as-received and heat treated materials are determined from the stress-strain curves in Fig. 19a. Note that the heat-treatment reduces the yield strength of the as-received material from 300 MPa (43 ksi) to 180 MPa (26 ksi). The corresponding reduction in the ultimate tensile strength is much less – from 675 MPa (98 ksi) to 600 MPa (87 ksi). Overall, the heat treatment causes a 20% reduction in flow stress at room temperature, from 535 MPa (78 ksi) to 430 MPa (62 ksi). Reduction of flow stress with temperature was estimated from INEEL rod data, as indicated in Fig. 19b. There is an ≈10% reduction in flow stress from room temperature to 282°C.

A comparison of predicted versus observed failure pressures for the as-received material at room temperature is shown in Fig. 20a. Note that the ligament rupture pressures for the 80% part-throughwall notches are predicted reasonably well. The ligament rupture pressure of the 90% deep, 9 mm (0.36 in.) long flaw is slightly greater than that predicted, while that of the 6 mm (0.25 in.) long flaws is predicted reasonably well. Additional tests with short and deep flaws are planned for the future. Specimens (80% deep 38 mm [1.5 in.] long and 60% deep 6 mm [0.25 in.] long notches) for which the ligament rupture pressures are greater than the unstable burst pressures for the corresponding 100% throughwall flaws did fail by unstable burst on ligament rupture, as predicted by the model. The 80% deep 6, 12.5 and

19 mm (0.25, 0.5 and 0.75 in.) long flaws and 90% deep 6 mm (0.25 in.) long flaw remained stable after ligament rupture and needed additional pressurization for an unstable burst to occur, also as predicted by the model. The burst pressures of 100% throughwall flaws, as well as those for which the ligament rupture pressures are lower than the burst pressures of corresponding throughwall flaws, were predicted reasonably well. Most specimens with the shorter flaws will be tested to unstable bursts in the High Pressure Test Facility.

A similar plot (Fig. 20b) for the heat-treated material shows that the reduction in failure pressure for the 38 mm (1.5 in.) flaw is consistent with the 20% loss in flow stress. Although the number of tests at 282°C with no observed failure are rather limited, the tests to date are not inconsistent with predictions (Fig. 21).

Predictive models for multiple notches or cracks are not currently available and will be developed in the future.

4.1.1.1 Correction Factor for Ligament Rupture and Tube Burst Pressures

All failure tests on laboratory-grown stress corrosion cracks at ANL are being conducted on Alloy 600 tubes that have been subjected to prior annealing and sensitizing heat treatments. The yield and flow stresses of these heat-treated tubes are considerably lower than those of the as-received tubes (Fig. 19a). The room-temperature flow stress of our as-received Alloy 600 tube is about 20% greater than that of the sensitized tube, which is consistent with the difference in failure pressures between tests on as-received and heat-treated tubes. Thus, a correction factor of 1.2 should be applied to either the ligament failure pressure or unstable burst pressure of the heat-treated tube to obtain that of the as-received 7/8-in.-diameter tube. Until flow stress data at high temperature are available, the same correction factor should also be applied at 282°C.

4.1.2 Predicted Leak Rates

The leak rates were predicted using Eq. 44a-b, with Eq. 2 used for COA. A comparison between predicted and observed leak rates at room temperature for a 1 in. (25 mm) EDM notch in an as-received tube is shown in Fig. 22a. This specimen was depressurized after 2 ksi (13.8 MPa), and the residual crack opening displacement and crack opening area were measured. Subsequently, it was repressurized and tested to failure. The measured and calculated COAs were used to predict the leak rates, which agree remarkably well with the observed leak rates (Fig. 22a).

Calculated and observed leak rates at room temperature for a 0.5 in. (12.5 mm) long EDM notch in as-received and heat-treated tubes are shown in Fig. 22b. Note that the curves for as-received and heat-treated tubes diverge as the pressure is increased beyond 1 ksi (7 MPa). At 2.5 ksi (17 MPa), the leak rate in a heat-treated material is greater by a factor of 3 than that in the as-received tube. A similar plot for a 0.25 in. (6 mm) long flaw in an as-received tube is shown in Fig. 23a. The predicted leak rates are reasonably close to the observed leak rates for all tubes.

A leak rate test at 282°C on an as-received tube with a 0.5 in. (12.5 mm) long EDM notch has also been conducted. Although high-temperature tensile data are not available for the 7/8-in. (22 mm)-diameter tubing, tensile data for 0.5 in. (12.5 mm) round bar stock at various temperatures have been reported by INEEL (Figs. 19a-b). The yield strength of the tubing at

282°C needed for calculations was obtained by multiplying the room temperature yield strength by the ratio of the yield strengths of the round bar stock at 282°C and room temperature. The calculated leak rate is reasonably close to the measured value, as shown in Fig. 23b.

Thus, the standard smooth-edge-orifice leak rate equation (Eqs. 44a-b) appears to predict the leak rates through EDM notches at room temperature and 282°C very well. The difference in leak rate between room temperature and 282°C can be accounted for by the difference in the density of water. Also, reasonable correlation between the Zahoor model predictions and the measured leak rates indicate that the crack opening areas are reasonably estimated by Eq. 2. Whether the same set of equations can predict leak rates through tight and nonplanar stress corrosion cracks remains to be seen.

4.1.2.1 Correction Factor for Leak Rates

As mentioned earlier, all pressure and leak rate tests on laboratory-grown stress corrosion cracks at ANL are being conducted on Alloy 600 tubes that have been subjected to prior annealing and sensitizing heat treatments. The yield and flow stresses of these heat-treated tubes are considerably lower than those of the as-received tubes (Fig. 19a). To convert the leak rate data from the heat-treated tubes to the as-received tubes, we divide the leak rate data on heat-treated tubes by appropriate correction factors (>1).

The correction factor for accounting for the effect of changes in mechanical properties on leak rate is complex because it depends on pressure, temperature, and crack area or length. It also depends on whether the flaw is initially a tight SCC crack or a 0.0075-in. (0.19 mm) wide EDM notch.

To derive the leak rate correction factors, we used the Zahoor model (Eq. 2) to calculate the flaw opening area, and Eq. 44b to calculate volumetric leak rate through EDM flaws. The effects of material flow properties on leak rate enter through their effects on the flaw opening area A.

Variations of the leak rate correction factor with pressure, flaw length, and temperature are given in Figs. 24a-b for tight SCC cracks and in Figs. 25a-b for 0.19-mm (0.0075 in.)-wide EDM notches. These curves are based on room-temperature yield strengths of 296 Mpa (43 ksi) and 179 MPa (26 ksi) for as-received and heat-treated tubes, respectively. The yield strengths are reduced by 10% at 282°C. Note that the leak rate correction factors for notches are generally smaller than those for cracks. Also, the longer the crack (or notch), the larger the correction factor.

4.2 Tests on Heat-Treated Tubes with Laboratory-Grown Stress Corrosion Cracks

The purpose of these tests is to develop and validate predictive models for failure pressure and leak rate in existing steam generator tubes with realistic stress corrosion cracks. The ultimate objective is to be able to estimate the length, depth and morphology of the cracks from NDE data (e.g., EC + Point data) and predict the failure pressures and leak rates under normal operation and accident conditions. Five tests on Alloy 600 tubes with laboratory-produced axial ODSCC have been completed. Four of the tubes, 177, 195, 104, and 219, were cracked at ANL in an aqueous solution of sodium tetrathionate at room temperature. The fifth

tube, 2-10, was produced by Westinghouse with doped steam (without heat-treatment) and provides a comparison with the ANL cracked tubes (heat-treated).

The tests were designed to investigate flaw behavior under constant temperature and pressure holds at temperatures and pressures simulating normal SG operation and main steamline break, i.e., T = 282°C (540°F) and Δp = 8.3 and 17.2 MPa (1.2 and 2.5 ksi), respectively. These pressure plateaus were held for at least 2 h (depending on the leak rate and the water level in the blowdown vessel), with extended duration holds at intermediate pressures if flaw tearing, as indicated by a sudden increase in flow, was observed. Additional tests were conducted at room temperature (RT), and the test on Westinghouse tube 2-10 was initiated at RT and completed at 282°C. A summary of all tests is given in Table 3.

Three techniques were used to characterize the SCC flaws prior to testing, namely (a) dye penetrant examination and digital photography with computerized image analysis, (b) bubble testing with low-pressure air (0.28 MPa [40 psi]) in a water bath to identify regions of through- wall penetration, and (c) Eddy Current (EC) NDE using both a bobbin coil (BC) and an EC +Point probe. All five specimens showed evidence of one or two regions of throughwall penetration of the cracks during the pretest bubble tests, but did not have measurable water leak rates until pressures rose to substantially above 8.3 MPa (1.2 ksi). For the purpose of failure and leak rate predictions, the equivalent crack length and equivalent crack depth for each specimen were determined by the procedure outlined in Section 3.1.2.1.

4.2.1 Predicted Failure Pressures

Predicting failure pressures for the tests on specimens with ODSCC proved to be challenging because all were subjected to holds at constant temperature and pressure prior to failure – a situation to which flow stress criterion for failure does not generally apply. To complicate matters, some of these specimens did not leak at the beginning of the hold, but began to leak after a finite hold period. Often, the leak rate increased during the hold period. This type of time-dependent stable rupture of the ligament cannot be predicted by the current flow stress model, which is applicable to ligament rupture under rising pressure loading without hold. However, as will be seen, the flow stress model did predict the failure pressures reasonably well in cases where, during the pressure ramp between the pressure plateaus, the ligament ruptured abruptly resulting in an abrupt and large increase of leak rate.

Test SGL 177: Figure 2a shows the EC +Point data for test SGL-177, which was conducted at RT. Ligament thickness in this specimen was highly non-uniform. The ligament rupture model (Fig. 3) predicts a failure pressure of 30 MPa (4.35 ksi) at an equivalent crack length of 9 mm (0.35 in.). The predicted failure pressure is significantly greater than the experimentally observed 16.9 MPa (2.45 ksi). However, this test exhibited time-dependent ligament rupture, the leak rate being essentially zero for the first 100 min hold at 16.9 MPa (2.45 ksi) before a leak rate of 0.04 L/min (0.01 gpm) was detected. This specimen will be tested to failure in the High Pressure Test Facility in the future.

Test SGL 195: Figure 26a shows the EC +Point data for test SGL-195, which was conducted at RT. The ligament rupture model (Fig. 26b) predicts a failure pressure of 16.5 MPa (2.39 ksi) at an equivalent crack length of 12.3 mm (0.48 in.). In this test, the leak rate abruptly increased to 30 L/min (7.9 gpm) at 15.1 MPa (2.188 ksi), suggesting significant

ligament rupture. The ligament rupture pressure observed during the pressure ramp is comparable to the predicted value.

Test SGL 104: Figures 27a-b show the crack-depth profile (by EC +Point) for specimen SGL-104, which was tested at 282°C, and the calculated ligament rupture pressures corresponding to two equivalent rectangular cracks. The ligament rupture model (Fig. 27b) predicts a failure pressure of 18 MPa (2.61 ksi) at an equivalent crack length of 10 mm (0.39 in.). The experimentally measured failure pressure of 16.2 MPa (2.35 ksi) caused the leak rate to increase abruptly from 0 to 21 L/min (5.6 gpm), suggesting significant ligament rupture.

Test SGL 219: Figures 28a-b show similar plots for test SGL-219, which was conducted at 282°C. Like test SGL-177, this specimen also had a highly nonuniform ligament thickness and may even have been segmented (Fig. 28a). The ligament rupture model (Fig. 28b) predicts a failure pressure of 20 MPa (2.9 ksi) at an equivalent crack length of 10.5 mm (0.41 in.). The predicted failure pressure is significantly greater than the experimentally measured 13.3 MPa (1.925 ksi). This specimen showed extensive time-dependent increase in leak rate and achieved a maximum test pressure of 16.2 MPa (2.35 ksi), which is still lower than the predicted failure pressure.

Test 2-10 (W): An additional pressure and leak rate test was conducted on a Westinghouse-supplied tube with an SCC crack generated in doped steam. Figure 29 shows the pretest crack depth profile by EC +Point. Ligament thickness for this specimen was highly nonuniform, as in test specimen SGL-177. Two equivalent rectangular crack profiles (Figs 30a-b) were used for calculating the ligament rupture pressure. The yield strength and flow stress of the Westinghouse tube were estimated from a few hardness tests at RT to be 240 Mpa (35 ksi) and 485 MPa (70 ksi), respectively. The ligament rupture pressure was calculated to be 22 MPa (3.19 ksi) and 20 MPa (2.9 ksi) at room temperature (Fig. 30a) and 282°C (Fig. 30b), respectively, at an equivalent crack length of 11 mm (0.43 in.). However, as in test SGL-177, this specimen developed a leak rate of 0.04 L/min (0.01 gpm) after a >3 h hold at 17.2 MPa (2.5 ksi) at RT, and the leak rate increased to 0.07 L/min (0.018 gpm) after an overnight hold at the same pressure.

All five specimens will be tested to failure (burst) in the High Pressure Test Facility.

4.2.2 Predicted Leak Rates

As before, predicting the leak rates was challenging because of the time-dependent increase in leak rates observed during constant temperature and pressure holds. However, where the ligament rupture model could estimate the failure pressure within reasonable limits, the predicted leak rates based on the equivalent rectangular crack lengths were close to the observed leak rates. For cases where leakage occurred at much lower pressures than predicted by the ligament rupture model, effective lengths of the throughwall segments of the cracks were estimated with the leak rate model. In most cases, the lengths of the throughwall segments of the cracks, calculated from leak rate data, are close to the lengths of the most open part of the cracks as evident visually from posttest pictures of the specimens. Both lengths correspond approximately to the length over which the pre-test crack depth exceeds 70% wall thickness.

Test SGL 177: As mentioned earlier, the predicted ligament failure pressure of 30 MPa (4.35 ksi) is significantly greater than the experimentally observed 16.9 MPa (2.45 ksi). Therefore, the leak rate was not calculated by using the predicted equivalent rectangular crack length. Instead, the lengths of the throughwall segment of the cracks were estimated from the measured leak rates from the leak rate model (Fig. 31). However, the leak rate in this test was essentially zero for the first 100 min hold at 16.9 MPa (2.45 ksi), after which a leak rate of 0.04 L/min (0.01 gpm) was detected, the rate abruptly increased from 0.04 to 0.26 L/min (0.01 to 0.068 gpm) after a further 60 min hold at the same pressure. The leak rate model (Fig. 31) would imply that the throughwall crack length increased abruptly from 1.5 to 3.7 mm (0.059 to 0.146 in.). The leak rate increased to 1.67 L/min (0.44 gpm) when the pressure was finally increased to 19.3 MPa (2.8 ksi), suggesting that the throughwall crack length increased to 5.6 mm (0.22 in.), which corresponds approximately to the length over which the crack depth exceeds 70% wall thickness (Fig. 2b). A posttest picture of the crack is shown in Fig. 32a and also includes a marker of length 5.6 mm (0.22 in.). A comparison of the posttest crack (Fig. 32a) with its pretest dye penetrant enhanced view (Fig. 32b) shows that although some secondary cracks opened up, the surface length of the main crack did not increase during the test. This specimen was internally pressurized under water with 40 psi (0.27 MPa) air after the test. From the emerging air bubble, it was estimated that the length of the throughwall segment of the crack was ≈ 4 to 4.8 mm (0.16 to 0.19 in.). In view of the additional crack opening due to pressurization, the measured length of the throughwall segment of the crack is reasonably close to the final crack length calculated from the measured leak rate.

Test SGL 195: In this test, the leak rate was <0.04 L/min (0.01 gpm) at 14.7 Mpa (2.129 ksi), suggesting a throughwall crack length of <2 mm (0.08 in.). The leak rate abruptly increased to 30 L/min (7.9 gpm) at 15.1 MPa (2.188 ksi), suggesting significant ligament rupture, and then to 33 L/min (8.6 gpm) at 15.5 MPa (2.25 ksi). The rate did not increase during a 15 min hold at 15.5 MPa (2.25 ksi). Because the ligament rupture pressure was predicted reasonably well by the ligament rupture model, the leak rate was calculated by using the equivalent rectangular crack length (12.3 mm [0.48 in.]), as shown in Fig. 33a. The observed leak rate is very close to the predicted leak rate. A posttest view of the crack at the OD surface is shown in Fig. 33b, which also includes a marker identifying the equivalent rectangular crack length, which as before, is close to the length over which the crack is most open. Also, a comparison with Fig. 26a shows that the equivalent rectangular crack length corresponds to the crack length over which the depth equals or exceeds 70% of the wall thickness.

Test SGL 104: A pressure of 16.2 MPa (2.35 ksi) caused the leak rate to increase abruptly from 0 to 21 L/min (5.6 gpm), suggesting significant ligament rupture. The leak rate increased to 23.6 L/min (6.2 gpm) at a pressure of 17.2 MPa (2.5 ksi) and did not increase during a 15 min constant-pressure hold at 17.2 MPa (2.5 ksi). Since the ligament rupture pressure was predicted reasonably well by the ligament rupture model, the leak rate was calculated using the equivalent rectangular crack length (10 mm [0.39 in.]), as shown in Fig. 34a. The observed leak rate is very close to the predicted rate. A posttest view of the crack at the OD surface is shown in Fig. 34b, which also includes a marker identifying the equivalent rectangular crack length, which as before, is close to the length over which the crack is most open. Also, a comparison with Fig. 27a shows that the equivalent rectangular crack length corresponds to the crack length over which the depth exceeds approximately 70% of the wall thickness.

Test SGL 219: Because this specimen exhibited extensive time-dependent increase of leak rate at constant pressure, the rate was not calculated by using the predicted equivalent rectangular crack length. Instead, the lengths of the throughwall segments of the cracks were estimated from the measured leak rates by using the leak rate model (Fig. 35a). This specimen first had a rate of 3.7 L/min (0.97 gpm) at a pressure of 13.3 MPa (1.93 ksi), and this rate did not increase during a 90 min hold at this pressure. Subsequently, the rate increased to 14 L/min (3.7 gpm) when the pressure was increased to 16.2 MPa (2.346 ksi). Figure 35a suggests that the effective crack length is between 8.4 and 9.2 mm (0.33 to 0.36 in.). During an 11 min constant-pressure hold at 16.2 MPa (2.346 ksi), the rate increased steadily from 14 L/min (3.7 gpm) to 39 L/min (10.3 gpm), which suggests that the effective throughwall crack length increased from 9.2 to 11 mm (0.36 to 0.43 in.) during the hold period. Flow remained constant at 39 L/min (10.3 gpm) for the next 9 min at the same pressure. Although the final estimated throughwall crack length is reasonably close to the equivalent rectangular crack length (Fig. 28b), the predicted rupture pressure (20 MPa [2.9 ksi]) is significantly greater than the experimental maximum pressure. A posttest view of the crack at the OD surface is shown in Fig. 35b, which also includes a marker identifying the estimated throughwall crack length from the leak rate data. A comparison with Fig. 28a suggests that the estimated final crack length corresponds to the length over which the crack depth exceeds 70% of the wall thickness.

Test 2-10 (W): The length of the throughwall segment of the crack was estimated from the measured leak rates with the leak rate model (Fig. 36a). This specimen developed a leak rate of 0.04 L/min (0.01 gpm) after a >3 h hold at 17.2 MPa (2.5 ksi) at RT and this rate increased to 0.068 L/min (0.018 gpm) after are overnight hold at the same pressure. Figure 36a implies that the effective throughwall crack length increased from 1.8 to 2.3 mm (0.071 to 0.091 in.) during this hold period. The leak rate then increased to 0.12 L/min (0.032 gpm) after a >5 h hold at 18.6 MPa (2.7 ksi), implying a final effective throughwall crack length of 2.8 mm (0.11 in.). The same specimen was later pressurized to 18.6 MPa (2.7 ksi) at 282°C and held at constant pressure. The leak rate increased from 0.3 to 0.72 L/min (0.079 to 0.19 gpm) during a 2 h hold. Figure 36a implies that the effective throughwall crack length increased from 3.6 to 4.8 mm (0.14 to 0.19 in.) during that hold period. The equivalent rectangular crack length is much greater (11 mm [0.43 in.]) than the throughwall crack length estimated from the final leak rate, even though the final test pressure is close to the predicted ligament rupture pressure. A posttest view of the crack at the OD surface is shown in Fig. 36b, which also includes a marker identifying the estimated throughwall crack length of 4.8 mm (0.14 in.).

In contrast to the ANL specimens, the estimated posttest throughwall crack length for the Westinghouse specimen from the leak rate data is significantly shorter than that observed visually. A closer examination of Fig. 36b shows that in contrast to the ANL specimens in which none of the ligaments between axial segments survived the test, the crack in the Westinghouse specimen had at least three axial segments (undetected by EC +Point method) separated by 0.4-mm (0.015 in.)-thick surface ligaments that survived the pressure loading. It is not clear whether the ligaments between the segments persist through the full thickness of the tube wall. It is likely that the effective crack length calculated from the leak rate would be much closer to that observed visually if the stiffening effects of the ligaments on the crack opening area were taken into account. Also, the ligament rupture model using the equivalent rectangular crack approximation most likely underestimates the pressure to rupture the through-thickness crack tip ligament significantly (and overestimates the throughwall crack length) in this case for the same reason.

4.2.2.1 Predicted Leak Rates Adjusted for Flow Stress

All of the pressure and leak rate tests on ANL specimens with laboratory-grown ODSCC cracks have been conducted on heat-treated tubes with significantly reduced flow stress properties. As is well known, failure pressures, leak rates, etc., depend on the mechanical properties (primarily the flow stress) of the tubing. The minimum ASME code requirements for yield and ultimate tensile strengths of Alloy 600 steam generator tube are 241 MPa (35 ksi) and 552 MPa (80 ksi), respectively, which correspond to a minimum flow stress of 400 Mpa (58 ksi). Some older steam generators may have tubes with properties close to the code minimum, while others may have significantly higher flow properties. The actual flow stress of steam generator tubes in most current plants can vary widely, depending on the age and heat of material used. Yield strength can range from 275 MPa (40 ksi), to 414 MPa (60 ksi), while the ultimate tensile strength can be 620 MPa (90 ksi) to 758 MPa (110 ksi), potentially covering a range of flow stress from 448 to 586 MPa (65 to 85 ksi). The yield and ultimate tensile strengths of the ANL as-received tubing are 296 MPa (43 ksi) and 675 MPa (98 ksi), respectively, almost exactly in the middle of the ranges reported above. However, because of the annealing and sensitizing heat treatments given to our tubes with laboratory-grown stress corrosion cracks, their yield and ultimate tensile strengths are estimated to be reduced to 180 MPa (26 ksi) and 607 MPa (88 ksi), respectively. Thus, although the yield strength of our heat-treated tubing falls below the code minimum, the ultimate tensile strength is sufficiently above the code minimum to give a flow stress that is close to the code minimum. To compare results on one material with results on a different material, the effect of variations in the mechanical properties must be accounted for, i.e., the results must be normalized in terms of the flow stress. Therefore, the leak rates measured in the ANL tests on tubes with ODSCC were corrected to estimate the leak rates in the as-received material. A procedure for obtaining the correction factor is given in Subsection 4.1.2.1.

However, the calculations are complicated by the time-dependent nature of the leak rates observed in the tests. Currently, we do not have a procedure for converting time-dependent leak rate data from one material to another with different flow properties. For the present, the measured leak rate data at the maximum test pressures were corrected to provide leak rates in the as-received material (Table 4) by assuming that the same crack that existed in the heat-treated material also exists in the as-received material. To determine the correction factors, estimates of the length of the throughwall segments of the cracks are needed, as discussed in Subsection 4.1.2.1. These crack lengths were obtained from the measured leak rates by using the leak rate model and the yield strength property of the heat-treated material. A second correction was also applied to the test pressures in Table 4 to reflect that a 20% higher pressure will very likely be needed to produce final cracks in the as-received material that are similar to those in the ANL test specimens. The final column in Table 4 includes the predicted leak rates at these calculated pressures. Validity of the assumption that cracks, with the same morphology as in the heat-treated material, can be created in the as-received material by applying 20% higher pressures has not yet been determined.

5 Behavior of Electrosleeved Tubes at High Temperatures

A schematic diagram of an Electrosleeved tube is shown in Fig. 37. Either an axial crack of various lengths or a 360° circumferential crack is assumed to exist through the full thickness of the parent tube wall. During a severe accident, the tube is subjected to a time-varying temperature and pressure (Δp) history. The flow stress failure criteria for both the axial and circumferential cracks can be stated as

$$\sigma_{lig} = H(T,t), \tag{45a}$$

where H is the hardness or flow stress (dependent on the temperature history) of the Electrosleeve, and σ_{lig} is the ligament stress, which for the two types of crack is given by

$$\sigma_{lig} = \begin{cases} m_p\sigma_h \text{ for axial cracks} \\ \sigma_A \text{ for circumferential cracks,} \end{cases} \tag{45b}$$

where m_p, which depends on the axial crack length and depth, is the ligament stress magnification factor; σ_h is the hoop stress (calculated by using the mean radius and total thickness of the tube and the sleeve); and σ_A is the axial stress based on the net section of the tube and the sleeve.

5.1 Determination of m_p for Axial Cracks

Initially, the hoop stress magnification factor m_p for the crack tip ligament in the Electrosleeve was estimated from the equation for a single-layer shell used in Ref. 4. However, the m_p factor could be reduced if the flow stress of the Electrosleeve ligament is significantly lower than that of the parent tube. In fact, detailed analyses of available tensile data of the Electrosleeve (to be discussed later) showed that at the temperatures of interest, the flow stress ratio between the parent tube and the Electrosleeve ranges from 2 to 3. To determine the effect of the flow stresses of the Electrosleeve and Alloy 600 on m_p, a series of FEA was conducted for a bilayer tube with a 100% throughwall crack in the outer layer (simulating Alloy 600) under a constant temperature and increasing pressure loading. The ratio between the flow stress of the outer layer and the inner layer (simulating the Electrosleeve) was 1 to 3. For displaying the FEA results, a hoop stress magnification factor m_p' was defined as follows:

$$m_p' = \frac{\text{Average Electrosleeve Ligament Hoop Stress}}{\text{Nominal Hoop Stress in Tube Wall}} \tag{46a}$$

The FEA results, plotted in Figs. 38a-b, confirm that the values of m_p' are reduced significantly when the flow stress ratio is increased. The m_p' factor as computed from FEA results generally varies with pressure. However, the behavior of long cracks is different from that of short cracks, as shown in Figs. 38a-b. For long cracks, m_p' increases with pressure and tends to level off at higher pressure. Behavior for the shorter 0.5 in. (12.5 mm) crack is just the opposite; m_p' decreases with pressure and tends to level off at higher pressure. Note that the m_p' factor for the 0.5 in. (12.5 mm) crack can drop below 1 if the decrease in flow stress of the Electrosleeve is sufficiently large. Although m_p' is decreasing with increasing pressure for short crack (Fig. 38b), the average ligament stress (or plastic strain) is still increasing with increasing pressure because m_p' is obtained by dividing the average ligament

stress by the nominal hoop stress in the uncracked section (Eq. 46a). Nor does a value of $m_p' < 1$ imply that the Electrosleeve/Alloy 600 composite tube wall away from the crack will fail before the crack tip ligament. The average stress in the Electrosleeve ligament relative to its flow stress always remains higher than the average stress in the Electrosleeve/Alloy 600 composite tube wall (away from the crack section) relative to its thickness-weighted flow stress.

For both short and long cracks, m_p' increases rapidly (suggesting onset of failure) with further increase in pressure in a regime where the Electrosleeve experiences significant plastic yielding away from the crack tip ligament. The value of m_p' at the point where it levels off (i.e., just prior to failure) was defined as m_p(FEA). As shown in Fig. 39, the m_p(FEA) (for flow stress ratio = 1) agrees well with that calculated with the ANL correlation for cracks ≤ 1 in. (25 mm), but levels off with increasing crack length beyond 2 in. (51 mm). On the other hand, the m_p calculated by the ANL correlation continues to increase with increasing crack length, although the actual increases are small beyond a crack length of 2 in. (51 mm).

Because the FEA grid may not have been sufficiently fine to obtain highly accurate solutions, the FEA results were used to calculate the ratio between the m_p(FEA) for the Electrosleeved tube and the homogeneous tube as a function of the ratio between the flow stress of the parent tube and the Electrosleeve, as shown in Fig. 40. This m_p ratio was then used to scale the m_p calculated by the ANL correlation for a homogeneous tube to obtain the effective m_p of the Electrosleeved tubes with notches, as indicated in Eq. 46b (FSR denotes flow stress ratio):

$$m_p(\text{eff.}) = \frac{m_p(\text{FEA})}{m_p(\text{FEA}, \text{FSR} = 1)} \times m_p(\text{ANL}). \qquad (46b)$$

5.2 Material Property Data for Electrosleeve

The initial development of the model was based on three sets of material property data contained in a report by FTI and titled "Electrosleeving Qualification for PWR Recirculating Steam Generator Tube Repair," Report No. BAW-10219P, Rev. 03, Oct. 1998. Subsequently, FTI provided two additional sets of data, one describing the time-dependent decrease in flow stress of the Electrosleeve material upon isothermal aging and the other on failure tests on Electrosleeved tubes with cracks under simulated severe accident transients.

The FTI data show that the Electrosleeve material is stronger than the tube material at the reactor operating temperature. However, at high temperatures (≥400°C), the Electrosleeve begins to lose its hardness because of grain growth (Fig. 41). The thermal aging effect is a complicated phenomenon consisting of at least two steps. In the first step, the phosphide precipitates in the grain boundary, which prevent grain growth, are dissolved; in the second step, grain growth occurs. The starting or initial hardness of the FTI isothermal aging specimens show a very large specimen-to-specimen scatter. Therefore, the loss of hardness data for each specimen was normalized with respect to its initial hardness at temperature, as shown in Fig. 41, where the data suggest that the hardness of the material starts to decrease, albeit at a relatively slow rate, beginning very early. The nucleation times for this process for specimens aged at > 425°C are relatively short and are ignored in the nucleation model to be discussed later. The data in Fig. 41 also suggest the existence of a second process with longer

nucleation times that involves very rapid decrease in hardness with time and is very likely linked to rapid grain growth. The reciprocal of the incubation time for the onset of rapid loss of hardness (rapid grain growth) has the temperature-dependent activation energy shown in Fig. 42. For analyses of loss of hardness, the continuously varying activation energy curve Q was replaced by the step function indicated in Fig. 42. Sensitivity studies, which are presented later in the report, showed that the results are not sensitive to the form chosen for Q.

Data for the yield and ultimate tensile strengths of the Electrosleeve material are given in the FTI report from RT to 343°C. Flow stress, which is the average of the yield and ultimate tensile strengths, as a function of temperature is shown in Fig. 43. The single high-temperature Electrosleeve data point in Fig. 43 was estimated from a tensile test conducted on aged material and will be discussed later. Initially, in the absence of any other flow stress data at high temperature, the solid line in Fig. 43 was used as an estimate for the unaged flow stress curve of the Electrosleeve. It should be remembered that during a severe accident, the actual flow stress of the Electrosleeve is reduced from the unaged curve (H_i) shown in Fig. 43 because of grain growth. The high-temperature tests conducted by ANL (to be discussed later) and FTI suggested that the unaged flow stress of the Electrosleeve material is less than that shown in Fig. 43.

FTI also submitted data to the NRC from a series of tensile tests at 343°C on specimens exposed to isothermal preaging treatment at high temperatures for various times (Fig. 44). The single data point at 760°C is from a tensile test conducted at 760°C. This specimen was heated at a slow linear ramp of ≈5.8°C/min from 327°C. The effective aging time at 760°C was estimated from an activation energy of 35 kcal/mole to be 39 min.

FTI also provided failure data from six tests on internally pressurized tubes that were subjected to a variety of temperature ramps simulating those expected during station blackout (SBO) accidents. The initial temperature ramp rate up to ≈500°C ranged from 3 to 5°C/min, which was generally followed by a ramp rate of 7 to 9°C/min until failure. However, in some cases, the ramp rate was gradually decreased to 1.2°C/min above 705°C. Three tests were conducted on unsleeved Alloy 600 tubes with and without degradation and three on Electrosleeved tubes (7/8 in. [22 mm] diameter) with 0.5, 1, and 2 in. (12.5, 25, and 51 mm) throughwall axial notches in the parent tube.

5.3 Analytical Model Based on Hall-Petch Equation

Two analytical models were originally developed for estimating the failure temperature under severe accident transients – a model based on linear damage rule and a model based on the Hall-Petch relationship. Both models gave comparable results for predicted failure temperatures. Because the Hall-Petch model was more mechanistically based, it was selected for use in failure prediction. In both models, a basic assumption is the existence of a temperature-dependent unaged (i.e., without grain growth) flow stress curve of the Electrosleeve. This unaged flow stress curve is largely a theoretical construct of the models because to establish it directly from tensile tests at high temperatures would be difficult due to the grain growth that would inevitably occur in the specimens unless the specimens could be heated, stabilized, and tested very rapidly. Therefore, it was calculated from high-temperature failure data by using the models. Ideally, high-temperature failure tests on specimens subjected to severe accident temperature and pressure ramps should be used to derive the

flow stress curve of the Electrosleeve. Since such test data were not available when the models were first developed, the unaged flow stress curve of the Electrosleeve was derived initially from analyses of the FTI tensile test data at various temperatures on specimens preaged at 760°C. Subsequently, the flow stress curve of the Electrosleeve was recalculated on the basis of high-temperature failure tests conducted at ANL.

In the model based on Hall-Petch equation, the "nucleation" phase is explicitly separated from the "growth" phase of the grain growth phenomenon. As mentioned earlier, it was assumed that the Electrosleeve has an initial "unaged" flow stress curve $H_i(T)$, e.g., Fig. 43. The hardness or flow stress (at a sufficiently high strain rate) of the Electrosleeve material was assumed to depend on the grain size by the Hall-Petch relationship, i.e.,

$$H(T) = Ad^{-n}f(T), \tag{47}$$

where H(T) is the flow stress at any temperature T, d is the grain diameter, n is the Hall-Petch exponent, and f(T) is a correction factor for temperature. During high-temperature exposure, the growth rate of grain diameter ($\dot{d}$) was assumed to be

$$\dot{d} = \begin{cases} 0 \text{ for } t < t_n \\ \dfrac{B}{d}\exp\left(\dfrac{-Q_g}{RT}\right) \text{ for } t \geq t_n, \end{cases} \tag{48}$$

where t_n is the nucleation time to loss of flow stress (i.e., onset of grain growth), B is a constant, Q_g is the activation energy for grain growth, and R = 1.987 cal/mole/°C. Recrystallization due to plastic straining was ignored. The form of the grain growth rate equation was chosen such that, under isothermal aging, the grain growth follows a parabolic law. Under isothermal aging, the reciprocal of the nucleation time ($1/t_n$), which has an activation energy Q_n, is given by the following equation:

$$\frac{1}{t_n} = C\exp\left(\frac{-Q_n}{RT}\right), \tag{49}$$

where C is a constant. The variation of Q_n with T is given in Fig. 42.

The tensile data reported by FTI on preaged specimens of Electrosleeve material were used to calculate the values of various parameters in Eqs 47-49. Integrating Eq. 48, using Eq. 49 and assuming $Q_n = Q_g = Q$,

$$d(t) = \left[d_i^2 - \frac{2B}{C} + 2Bt\exp\left(\frac{-Q}{RT}\right)\right]^{1/2}, \tag{50}$$

where d_i is the grain diameter of the as-received material and T is the aging temperature. Substituting Eq. 50 into Eq. 47, denoting the tensile testing temperature as T_o, the initial "unaged" flow stress at T_o as H_o and solving,

$$t\exp\left(\frac{-Q}{RT}\right) = \frac{d_i^2}{2B}\left[\left(\frac{H_o}{H}\right)^{2/n} - 1\right] + \frac{1}{C}, \tag{51a}$$

where

$$H_o = Ad_i^{-n} f(T_o). \tag{51b}$$

Results from the FTI tensile data (T_O=343°C) on preaged specimens are plotted in Figs 45a-b for assumed values of n = 0.33 and n = 0.4, respectively. Both fits are quite good and reasonably close to the conventional value of 0.5. Values of $d_i 2/2B$, and 1/C were obtained from the slope and intercept of the linear fits. As mentioned earlier, the specimen that was aged for 30 min at 760°C was also tensile tested at 760°C. Because this specimen was ramped from 327 to 760°C at the slow rate of 5.8°C/min before the constant-temperature aging, an analysis using an activation energy of 35 kcal/mole gave an effective aging time at 760°C of 39 min. A reduction factor for the flow stress at 760°C compared to that at 343°C was obtained by fitting the data, excluding the 760°C data, and extrapolating the best-fit line to the value of the time-temperature parameter of the test, as shown by dotted lines in Figs. 45a-b. The two flow stress curves (Figs. 43 and 46) correspond to the two estimated values of flow stress at 760°C by the two fits. The difference between the two flow stress curves is negligible.

Nucleation times to onset of loss of flow stress (i.e., grain growth) under isothermal aging were calculated by using Eq. 49 and the stepwise varying approximation to the activation energy data shown in Fig. 42. The results, plotted in Fig. 47 for two Hall-Petch exponents, show that the two exponents give widely varying estimates for nucleation times. The nucleation times for the rapid loss of hardness as derived from the FTI data (Fig. 41), also plotted in Fig. 47, show that n = 0.33 fits the data better. The calculated curves of loss of hardness (for n = 0.33 and 0.4) with time under various isothermal aging are compared with the FTI data in Fig. 48. Although the model does not simulate the initial low rate of loss of hardness, it does represent the subsequent rapid loss of hardness reasonably well for both values of n.

Under a variable temperature history, Eq. 49 can be generalized to give the time to nucleation as follows:

$$C\int_0^{t_n} \exp\left(\frac{-Q}{RT(t)}\right)dt = 1. \tag{52}$$

Similarly, Eq. 48 can be integrated to give the grain diameter at any time t:

$$d(t) = \begin{cases} d_i & \text{for } t < t_n \\ \left[d_i^2 + 2B\int_{t_n}^{t} \exp\left(\frac{-Q}{RT(t)}\right)dt\right]^{1/2} & \text{for } t \geq t_n \end{cases} \tag{53}$$

Substituting Eqs 52-53 into Eq. 47 and solving for the flow stress H at any time,

$$H(t) = \begin{cases} H_i(t) & \text{for } t < t_n \\ \left[1 + \frac{2B}{d_i^2}\int_{t_n}^{t} \exp\left(\frac{-Q}{RT(t)}\right)dt\right]^{-n/2} H_i(t) & \text{for } t \geq t_n, \end{cases} \tag{54}$$

where $H_i(t)$ is the initial "unaged" flow stress at T(t). Ligament failure is predicted to occur when Eq. 45a is satisfied.

5.4 Initial Analytical Results

The model using the Hall-Petch equations to represent the changes in the flow stress was used to calculate failure temperatures. The studies in Ref. 5 showed that SBO represents a severe challenge to the integrity of steam generator tubes in which the secondary system dries out and the primary system fails to depressurize (a "high–dry" sequence). In this case, the Δp across the tube wall is a constant 2.35 ksi. The time–temperature history was taken as bilinear with an initial 5°C/min segment to 670°C, followed by 2°C/min segment until failure (Fig. 49). This temperature ramp is a simplified version of those used in Ref. 5 for the severe accident tests on flawed tubes without repairs. It is even more conservative than the Ref. 5 versions because the slower segment starts at a lower temperature. Additional sensitivity studies were done with simple 1°C/min and 5°C/min ramps. Results are reported for both Electrosleeved and unsleeved tubes so that the relative strengths can be compared.

5.4.1 Results for Unsleeved Tubes

The data and the flow stress model presented in Ref. 4 showed that the failure temperature of an unflawed Alloy 600 tube is 840°C, which is greater than the tube temperature at the time of surge line failure. Thus, an unflawed tube is predicted to survive the scoping ramp.

An unsleeved Alloy 600 tube with the deepest cracks that can survive a Δp equal to three times the Δp during normal operation ($3\Delta p_{NO}$) was also considered; for these calculations $3\Delta p_{NO}$ was taken as 3.84 ksi. The maximum depths of 0.5-, 1-, and 2-in.-long cracks that satisfy this criterion are 76.6, 67.1, and 62%, respectively. The corresponding maximum depth for a 360° circumferential crack is 80%. Note that $m_p = 2.32$ for all these cracks, which will be collectively referred to as the $3\Delta p_{NO}$ crack. For this value of m_p the ligament stress σ_{lig} = 45 ksi. The corresponding failure temperature for both the axial and circumferential cracks by the flow stress criterion is 681°C (see, e.g., Fig. 43). The creep rupture model, which is more accurate than the flow stress model, predicts a failure temperature of 728°C.

5.4.2 Predicted Results for Electrosleeved Tubes

Figures 50a-b show the calculated reduction of flow stress of the Electrosleeve during the scoping ramp, as well as at 1°C/min for Hall-Petch exponents n = 0.33 and 0.4, respectively. Note that for each transient, the variations of flow stress with temperature are almost identical for the two exponents. Further, for each exponent, there is a difference in the flow stress curves initially for the two transients. Although the two curves ultimately converge, the convergence occurs at a much higher temperature than any of the predicted failure temperatures.

Figures 51a-b show the variation of the predicted failure temperatures (for n = 0.33 and 0.4) with axial crack length for an Electrosleeved tube with a throughwall crack in the parent tube subjected to the scoping ramp, as well as two other constant-temperature ramp rates. Note that the predicted failure temperatures corresponding to n = 0.33 and n = 0.4 differ by ≈5°.

The variation of failure temperature with the constant temperature ramp rate is shown in Fig. 52 for an Electrosleeved tube with a throughwall 360° circumferential crack in the parent tube. As before, the differences in the predicted failure temperatures using n = 0.33 and n = 0.4 are small.

5.4.3 Predicted vs. Observed Failure Temperatures for FTI Tests

As mentioned earlier, FTI performed tests on 7/8-in. (22 mm)-diameter unsleeved tubes, both degraded and undegraded, and on Electrosleeved tubes with 100% deep axial notches in the parent tube. All tests were conducted under a constant internal pressure of 2.35 ksi (16.2 MPa) and a variety of temperature ramps with the initial rate (at <500°C) ranging from 3 to 5°C/min. Above 500°C, the notched Electrosleeved specimens were ramped at 7-9°C/min to failure, except for the test with a 0.5 in. (12.5 mm) notch. For this test, the ramp rate was gradually reduced to 1.2°C/min above 705°C. Failure temperatures were calculated using the temperature ramps for each specimen supplied by FTI (Figs. 53a-c). Since a flow stress model was used for prediction, the predicted failure temperatures for the notched unsleeved Alloy 600 tubes were independent of the temperature history. The comparison between the predicted and observed failure temperatures is shown in Table 5. The details of the notch and tube geometry of the specimens are included in Table 6. The predictions in Table 5 were made using a high-temperature flow stress curve for the Electrosleeve material that was based on limited high-temperature tensile test data provided by FTI. The predictions are in much better agreement with the observed values, if a modified flow stress curve that includes the results of additional ANL tests is used, as will be discussed later.

The predicted failure temperatures overestimate the experimentally observed failure temperatures of the Electrosleeved tubes in all cases. The failure temperatures of the two degraded Alloy 600 tubes were predicted quite well by the flow stress model of Ref. 4. Note that these two tests are consistent with each other because the m_p value for a 50% deep 2 in. (51 mm) crack is approximately 2, which is also the hoop stress magnification factor for a 50% uniformly thinned tube. The test on undegraded Alloy 600 involved a hold at constant temperature – a loading history for which the flow stress model is inapplicable. However, the creep rupture model presented in Ref. 4 can predict the failure time within a factor of 2.

5.5 ANL Test Results

As mentioned earlier, FTI provided twelve Electrosleeved specimens, three of which were notched. Eight additional specimens were notched (≈0.0075 in. [0.2 mm] wide) at ANL by EDM. Eleven tests were conducted at ANL. The time/temperature history for these tests consisted of holding the pressure constant at 2.35 ksi (16.2 MPa) while ramping the temperature from 300 to 545°C at 4.2°C/min, followed by a 12.5°C/min ramp until failure (Figs. 54a-b). This ramp closely simulates the SBO sequence identified as Case 6RU in Ref. 5 and is felt to be a more realistic representation of the sequences of interest than the scoping ramp used for the initial analytical studies. A summary of all the tests conducted by ANL as well as by FTI is given in Table 6. Note that the FTI tests were conducted using different temperature ramps, as discussed in section 5.4.3.

In all the ANL specimens with 2- and 3-in. (51 and 76 mm) long flaws, both the unsleeved tubes and the Electrosleeves failed with large (fish-mouth) flaw openings. Although the specimens without repairs also failed with large flaw openings, the Electrosleeve tubes with

0.5 and 1 in. (12.5 and 25 mm) flaws failed without a visible openings. Similar failure modes were also observed by FTI.

5.5.1 Revised Unaged Flow Stress Curve of Electrosleeve

The failure temperatures for the ANL tests were used to recalculate the unaged flow stress curve of the Electrosleeve material by using the Hall-Petch model (with n = 0.33) and the effective m_p factor (as a function of crack length and flow stress ratio) from Fig. 40 and Eq. 46b. The revised unaged flow stress curve is compared with the previously estimated unaged flow stress curve (Fig. 43) in Fig. 55. Note that the revised curve has a different shape and falls below the earlier estimated curve. This revised unaged flow stress curve is used for all failure predictions in the remainder of this paper.

5.5.2 Predicted Failure Temperatures

5.5.2.1 ANL Tests

An examination of Table 6 shows that the geometries of the Electrosleeved tubes have some variations. An upper bound to the predicted failure temperatures was obtained by using the following:

Tube thickness = 0.051 in. (1.30 mm), sleeve thickness = 0.04 in.(1.02 mm) and notch depth = 0.048 in. (1.22 mm),

and a lower bound was obtained by using

tube thickness =0.049 in. (1.24 mm), sleeve thickness = 0.035 in. (0.89 mm), and notch depth = 0.049 in. (1.24 mm).

In cases where the notch depth was less than the full thickness of the parent tube wall, an effective flow stress for the ligament (average flow stress weighted by thickness) was used. The two bounds, together with the test data. are plotted in Fig. 56. Both the test data and the model indicate that the decrease in failure temperature with crack length saturates at a notch length of ≈76 mm (3 in.) and no significant additional decrease of failure temperature should occur at longer crack lengths. The tube-to tube variations in geometry give rise to a significant difference (60°C) between the two bounds. A much better correlation (within ±15°C) between the predicted and the observed failure temperatures is obtained if the actual geometry for each specimen is used in calculating the predicted failure temperatures (Fig. 57).

Finite-element analyses (FEAs) were conducted for an Electrosleeved tube (see Fig. 37) with 0.5-, 1-, and 2-in. (12.5-, 25-, and 51- mm) long cracks that are 100% throughwall and subjected to the Case 6RU temperature ramp (Fig. 54a) at a constant pressure Δp = 2.35 ksi (16.2 MPa). The grain-growth model discussed in Subsection 5.3.1 was used to estimate the flow stress curve of the Electrosleeve as a function of temperature during the Case 6RU ramp. The INEEL flow stress curve was used for the Alloy 600 tube. Stress-strain curves for both materials were approximated by bilinear curves (Figs. 58a-b) with low tangent modulus (strain hardening). The tangent moduli were determined by a linear fit between the yield and ultimate tensile strengths.

Figure 59a-c show the calculated variations of the average ligament hoop stress and average ligament plastic strain with temperature during the ramp for a specimen with a 13-mm (0.5 in.)-, 25-mm (1 in.)-, and 51-mm (2 in.)-long, 100% throughwall cracks, respectively. Also shown are the variations of the yield stress and flow stress of the Electrosleeve during the transient. In each case, the FEA predicts a rapid rise in the Electrosleeve ligament plastic strain after the average ligament stress exceeds the yield stress of the Electrosleeve. The temperatures needed to accumulate 2% average creep strain in the ligament of the 13, 25, and 51 mm (0.5, 1, and 2 in.) cracks are 780, 720 and 675°C, respectively. These temperatures agree fairly well with the test failure temperatures, which ranged from 806 to 807°C, 714 to 722°C, and 650 to 680°C for the 13, 25, and 51 mm (0.5, 1, and 2 in.) cracks, respectively.

5.5.2.2 FTI tests

Figure 60 shows a comparison of the failure temperatures as reported by FTI and the two bounds based on the same geometrical assumptions as in Fig. 56. All the tests tend to fall near the lower bound curve, which is not surprising because the thicknesses of the Electrosleeve were close to the lower bound thickness assumed for the curve. The predicted failure temperatures (using actual geometry and actual temperature ramp) are within 15°C of the observed values. The failure temperatures of the Electrosleeved tubes with throughwall notches appear to vary almost linearly with notch length (the curve is actually slightly concave downward), as shown in Fig. 60, which is quite different from the predicted concave-upward shape of the bounds.

Figure 61 shows typical failure temperature data for Alloy 600 tubes with part-throughwall notches reported in Ref. 4, together with predicted values using a flow stress model. For the notch depths chosen, the predicted failure temperatures by the flow stress model are close to those predicted by the creep rupture model, which was shown to be the more accurate of the two in Ref. 4. In all cases the predicted curves, which have been validated at ANL by many high-temperature tests, are concave upward, which is the shape predicted by all other available correlations also. However, as mentioned earlier, the FTI test failure temperatures of the Electrosleeved tubes appear to vary almost linearly with notch length. The difference can be traced to the fact that specimen BTF-23 (13 mm [0.5 in.] notch) had a relatively slow temperature ramp at high temperature (>705°C), while the other two specimens did not. Also, the notch in specimen R.5.2 (51 mm [2 in.] notch) penetrated into the Electrosleeve. For comparison purposes, the test failure temperatures were adjusted by using the flow stress model so that all specimens had identical (as those of BTF-25) tube wall thickness, Electrosleeve thickness, and notch depth and were subjected to the same temperature ramp as that used for specimen BTF-25. The adjusted failure temperature curve is concave upward, as shown in Fig. 62. Note that the upward shift of the adjusted failure temperature for the 13 mm (0.5 in.) notched specimen (primarily due to adjusting the ramp rate) is much greater than that for the 51 mm (2 in.) notched specimen.

5.5.3 Part-Throughwall Cracks

Initially, the failure temperatures of part-throughwall cracks were calculated by using the same approach as that for 100% throughwall cracks, i.e., by replacing the ligament stress and flow stress by their thickness averaged values. Since then, FTI has reported results from tests conducted on specimens with nominally 80% deep, 51-mm-long notches. The above approach

overestimated the failure temperatures of these tests significantly. Therefore, a series of FEA was conducted on part-throughwall cracks with the same reference tube wall and Electrosleeve thicknesses shown in Fig. 37 and subjected to the Case 6RU ramp.

Figures 63a-c show the calculated variations of the ligament-averaged hoop stress and plastic strain with temperature during the ramp for specimens with a 13-mm (0.5 in.), 25-mm (1 in.), and 51-mm (2 in.)-long, 80% throughwall cracks, respectively. Also shown are the variations of the ligament-averaged yield stress and flow stress during the transient. In contrast to the 100% deep cracks, the FEA-predicted rapid rise in the ligament-averaged plastic strain for the 80% deep cracks does not correlate with the ligament-averaged stress exceeding the ligament-averaged yield stress or flow stress. Figures 64a-c show the variations of the ligament-averaged plastic strains with temperature for 80, 90, and 100% deep, and 13-, 25-, and 51-mm (0.5-, 1-, and 2-in.)-long cracks under Case 6RU loading. The increases in failure temperature compared to those of a tube with 100% deep, 13-, 25-, and 51-mm (0.5-, 1-, and 2-in.)-long cracks are 10, 25, and 30°C for 90% deep cracks and 40, 60, and 80°C for 80% deep cracks, respectively. These incremental temperatures were added to the predicted failure temperatures for the 100% deep cracks to obtain the failure temperatures of the Electrosleeved tubes with part-throughwall cracks (Fig. 65).

5.5.3.1 Simplified Prediction Model for Shallow Flaws

Figure 66a compares the accumulation of plastic strain with temperature in the ligament of a 100% throughwall crack with that in the Alloy 600 portion of the ligaments of 80% and 90% part-throughwall, 13-mm (0.5 in.)-long cracks. Similar plots for 25- and 51-mm (1 and 2 in.)-long cracks are shown in Figs. 66b-c. It is possible that because of the relatively high ductility of the Electrosleeve at high temperatures compared to that of Alloy 600, the Alloy 600 portions of the ligaments of the part-throughwall cracks may run out of ductility and fail first. Under this scenario, because the failure temperatures of the ligament of 100% throughwall cracks are less than or equal to those of the Alloy 600 ligaments of the part-throughwall cracks, the Electrosleeve ligaments will fail immediately after the collapse of the Alloy 600 portion of the ligaments. Such a two-step failure process implies that the increases in failure temperature compared to those of a tube with 100% deep, 13-, 25-, and 51-mm (0.5-, 1-, and 2-in.)-long cracks are 0, 10, and 25°C for 90% deep cracks and 30, 45, and 75°C for 80% deep cracks, respectively. These increases are somewhat smaller than those estimated earlier on the basis of total collapse of the full ligament.

As the Alloy 600 portion of the ligament becomes larger compared to the Electrosleeve thickness (i.e., as the crack depth decreases), the hoop load carried by the Alloy 600 ligament begins to dominate that carried by the Electrosleeve ligament, particularly at high temperatures. Figure 67a shows the calculated variation of the m_p for the Alloy 600 ligament at the tip of a 13-mm (0.5 in.)-long, 80 and 90% deep crack. Similar plots for 25- and 51-mm (1 and 2 in.)-long cracks are shown in Figs. 67b-c. The values of m_p at the failure temperatures are much closer to those of the same cracks in an unsleeved tube [i.e., m_p (ANL)] for the 80% deep cracks than for the 90% deep cracks. This is consistent with the fact that the hoop stress generated by the pressure loading in the ligament is carried mostly by the Alloy 600 tube ligament at high temperatures.

For the simplified model, the following two-step procedure is followed to calculate the failure temperature of the ligament of the Electrosleeved tube with a part-throughwall crack.

First, the failure temperature of the Alloy 600 ligament is calculated, ignoring the contribution of the Electrosleeve ligament and using the m_p for the same crack in an unsleeved tube. After the failure of the Alloy 600 ligament, the crack becomes 100% throughwall. If the failure temperature of an initially 100% throughwall crack is less than the failure temperature of the Alloy 600 ligament, the full ligament of the initially 80% throughwall crack will fail immediately upon failure of the Alloy 600 ligament. On the other hand, if the failure temperature of an initially 100% throughwall crack is greater than the failure temperature of the Alloy 600 ligament, the full ligament of the initially 80% throughwall crack will fail at the same temperature as the initially 100% throughwall crack. The predicted failure temperatures for Case 6RU loading are shown in Fig. 68. The simplified model predicts no increases in failure temperatures for 90% deep cracks from those of 100% throughwall cracks, which is not surprising since it is not applicable for deep cracks. The predicted failure temperatures for 80% deep, 25 to 51-mm (1 to 2 in.)-long cracks are about 10-20°C lower than those predicted by FEA (Fig. 65). It is expected that the accuracy of the simplified model will improve for shallower cracks.

5.5.3.2 Tests on Part-Throughwall Notched Specimens

A summary of the ANL and FTI tests on Electrosleeved specimens with part-throughwall notches are given in Table 8. The depth profiles of the FTI notches (Figs. 69a-b) show that one of the notches was trapezoidal in shape (Fig. 69b). As before, the FTI tests were conducted with different temperature ramps than those of the ANL tests (Figs. 70a-b). The predicted failure temperatures for all the tests are given in the last column of Table 8. The predicted failure temperature for the test conducted at ANL was based on the FEA analysis of part-throughwall cracks and is also shown in Fig. 65. Because FEA results for the FTI specimens subjected to the FTI ramps were not available, the simplified model was used to estimate the failure temperatures which, as mentioned earlier, tend to be ≈10–20°C lower than the FEA results. The predicted failure temperatures are within 10-15°C of the experimentally observed values.

5.6 Predicted Failure Temperatures for Postulated SBO Severe Accidents

As mentioned earlier, calculations were done for the temperature and pressure histories shown in Figs. 54a-b that closely simulate Case 6RU of Ref. 5. Failure calculations were performed for the reference 7/8 in.- (22-mm)-diameter tube (wall thickness = 0.05 in. [1.27 mm] and Electrosleeve thickness = 0.038 in. [0.97 mm]) with 90% and 100% throughwall cracks of various lengths in the parent tube. The results, plotted in Fig. 65, show that failure temperatures for 100% throughwall cracks measuring 76, 51, 25, and 13 mm (3, 2, 1, and 0.5 in.) in length are 640, 650, 690, and 795°C, respectively.

5.7 Sensitivity Analyses

5.7.1 Creep Effect

In this report, a flow stress model was exclusively used to predict failure under severe accident transients. However, as was concluded in Ref. 4, a creep rupture model can predict the failure temperatures under severe accident transients more accurately than a flow stress model. A comparison between the predicted failure temperatures by the two models are shown in Table 7 for the case of an unsleeved tube with a $3\Delta p_{NO}$ crack, i.e., a 0.5 in. (13 mm)

by 76.6%, a 1 in. (25 mm) by 67.1%, or a 2 in. (51 mm) by 62% crack, or an 80% deep 360° circumferential crack.

Note that the failure temperature predicted by the flow stress model agrees well with that by the creep rupture model for the 1°C/min ramp, but is conservative for the other three ramps. In particular, the faster the ramp rate the more conservative the prediction. Because the unaged flow stress of the Electrosleeve was calculated from tests conducted with a temperature ramp of 12.5°C/min, it is expected that the flow stress model will overestimate the failure temperatures for tests at slower ramp rates unless grain growth effects predominate creep effects. Also, it should be noted that the failure times under constant temperature holds cannot be calculated with the flow stress models presented in this report unless grain growth effects predominate over creep effects. To accurately predict failure of Electrosleeved tubes under an arbitrarily varying temperature history (including constant temperature holds), a creep rupture model analogous to that presented in Ref. 4 and coupled with a grain growth model must be developed.

5.7.2 Thickness of Electrosleeve

The effect of an increase of Electrosleeve thickness from 0.038 to 0.043 in. (0.97 to 1.09 mm) on the ligament failure temperature under the reference Case 6RU SBO ramp is shown in Fig. 71. There is a ≈20°C increase in the failure temperature for all crack lengths.

5.7.3 Crack Depth

In most of the analyses, the crack depths were assumed to be 100% of the parent tube wall. Limited analyses were also carried out for Electrosleeved tubes with part-throughwall cracks, as discussed in section 5.5.3. The predicted failure temperatures, plotted in Fig. 65 (which also includes a test data point), show that the increase in ligament failure temperature from that for a 100% deep crack ranges between 10-30°C for a 90% deep crack and 40-80°C for a 80% deep crack, with the larger increases occurring for longer cracks. Additional tests with part-throughwall cracks are needed to verify the predicted failure temperatures.

5.7.4 Crack Length

In all the calculations and tests, the maximum crack length considered was 76 mm (3 in.). The test data shown in Fig. 56 clearly suggest a leveling-off of the failure temperature with increasing crack length beyond 76 mm (3 in.). However, a question arises as to whether there could be a significant reduction in failure temperature if crack length were much longer. This is particularly of concern because although the m_p values calculated by the ANL correlation and by FEA agree remarkably well for crack lengths ≤ 25 mm (1 in.), there is some discrepancy between the two for crack lengths > 25 mm (1 in.) (Fig. 39). In Fig. 39, it is evident that for a flow stress ratio of 1, although the ANL correlation shows a slight increase of m_p from 2.0 to 2.1 as the crack length is increased from 51 to 76 mm (2 to 3 in.), the FEA shows virtually no change in m_p from 1.85. In a similar fashion, for a flow stress ratio of 2, the FEA shows no increase in m_p from 1.6 when the crack length is increased from 51 to 76 mm (2 to 3 in.). The FEA results suggest that there should be no change in failure temperature beyond a crack length of 51 mm (2 in.), and the test data in Fig. 56 may be interpreted to support this. On the other hand, ANL correlation implies a further decrease in failure temperature with crack length. To be conservative, the ANL correlation for m_p modified

by flow stress correction factors derived from FEA was used. To estimate the magnitude of reduction in failure temperature with crack length, a plot of the ligament failure temperature with crack length up to 152 mm (6 in.) is shown in Fig. 72. Note that the reduction is 5°C in failure temperature going from a crack length of 51 to 76 mm (2 to 3 in.) and an additional 5°C from 76 to 152 mm (3 to 6 in.). Thus, although the ANL correlation suggests that the failure temperature continuously decreases with increasing crack length, from a practical standpoint the additional decrease beyond a crack length of 76 mm (3 in.) is negligible.

5.7.5 Variation of Activation Energy with Temperature

For all analyses in this report, the variation of the activation energy with temperature has been idealized by a step function, as shown in Fig. 42. To check the sensitivity of the calculated flow stress on the shape of the activation energy curve, the step function was replaced by plateaus at high and low temperature connected by a ramp. Figure 73 shows that while the choice of Q does affect the shape of the transition of the flow stress, it seems to have little real effect on the predicted behavior in severe accidents at high temperatures.

5.7.6 Failure Criterion

The failure criterion (Eq. 45a) was originally developed for cracks in homogeneous single layer shells and has been shown to be valid for a wide variety of ductile materials at low temperatures. FEA calculations for various ligament averaged stresses and plastic strain with pressure in a homogeneous tube with a 0.088 in. (2.24 mm) wall thickness containing a 3-in. (76-mm)-long, 0.05-in. (1.27-mm)-deep crack are shown in Fig. 74. This geometry corresponds to a crack in an Electrosleeved tube with a flow stress ratio = 1. Because the flow stress for the tube was assumed to be 414 MPa (60 ksi), Eqs. 45a-b would predict a failure pressure of ≈55 MPa (8 ksi), which is close to the failure pressure (48 MPa [7 ksi]) predicted by the ANL correlation for m_p. Note that the failure pressure correlates better with the average hoop stress rather than with either the average von-Mises effective stress or the average plastic strain in the ligament. In fact, the failure pressure corresponds to a calculated average ligament plastic strain of only ≈3%, which is much less than the uniaxial ductility of Alloy 600. However, Fig. 74 shows that the average ligament plastic strain is rising steeply with pressure. This rapid rise of plastic strain with pressure, together with the high average hydrostatic stress (which generally reduces ductility) in the ligament, are probably the reasons for the success of the criterion. Although different materials may have different uniaxial strains to failure, they would result in only modest changes in the failure pressure.

The corresponding case of a bilayer tube (simulating an Electrosleeved tube at high temperature) with a flow stress ratio = 2 is shown in Fig. 75. Since the flow stress of the softer inner layer (simulating the Electrosleeve) is 207 MPa (30 ksi), the current procedure with Fig. 75 would predict a failure pressure of 33 MPa (4.8 ksi), which again corresponds to an average ligament plastic strain of ≈3%. As before, the average plastic strain in the ligament is rising rapidly with pressure at this load level. Figure 75 shows results (using infinitesimal strain and displacement theory) up to a ligament plastic strain of 25%. A more appropriate finite-deformation analysis would have indicated an even more rapidly rising plastic strain with pressure. Thus, even if the ductility of the inner layer (Electrosleeve) is greater than that of the outer layer (Alloy 600), the additional pressure capability of the tube beyond that corresponding to an average ligament plastic strain of 3% would be low.

At room temperature, where failure is controlled by time-independent plastic deformation, FEA results suggest that Eq. 45a would be a reasonable failure criterion for Electrosleeved tubes. At high temperatures, tests on notched Alloy 600 tubes have shown that the flow stress criterion is less successful and that failure is better described by a creep damage criterion, particularly for deep notches (≥80%). But the flow stress model was still reasonably successful for shallower notches (≤66%), and it might be expected that the relative estimates of strength provided by the model are accurate even if the absolute failure temperatures are somewhat less so. Failure temperatures for tests on notched unsleeved and notched Electrosleeved tubes conducted by ANL and by FTI have been predicted with reasonable success with the flow stress model, except for a single test on an unnotched Alloy 600 tube that was subjected to a constant-temperature hold. It is expected that the current flow stress model will overestimate the failure temperatures if the temperature ramp rates are significantly slower than those used in the tests at ANL and if creep effects were to predominate grain growth effects.

5.7.7 Reduction of Flow Stress with Aging

In this report, aging has been simulated with a grain growth model, together with the hardness data supplied by FTI on Electrosleeve specimens aged at high temperatures. Thus, there is reason to expect some uncertainty in the calculated loss of flow stress with aging. FTI has suggested that the flow stress of Ni-200 at high temperature should provide a reasonable estimate for the flow stress of the Electrosleeve after grain growth. A comparison of flow stress data of Ni-200 and Ni-201 with the calculated flow stress of the Electrosleeve for the Case 6RU ramp rate (including the effect of aging) is shown in Fig. 76. The data for Ni-201 extend only to 649°C. The two FTI data points at 593°C and 760°C on aged Electrosleeve fall quite close to the Ni-200 curve. In the temperature area of interest for severe accidents, i.e., >650°C, the calculated aged flow stress curve is close to but slightly below the Ni-200 flow stress curve. The FTI data at 760°C on aged Electrosleeve falls below the Ni 200 curve and is closer to the calculated flow stress curve. Thus, the present estimates for loss of flow stress with aging are consistent with the FTI assumption for the severe accident transient.

6 Discussions and Conclusions

6.1 Transversely Supported SG Tubes with Circumferential Cracks

An approximate model has been developed for calculating crack opening area and failure pressure of laterally supported steam generator tubes with a throughwall circumferential crack at a clamped edge (e.g., top of tube sheet). The results show that the critical crack tip opening displacement as well as the span and the boundary conditions are important determining factors for the pressure at onset of crack extension. For typical mechanical properties and spans that are expected in PWR steam generators, tubes with throughwall cracks behave as if fully constrained against rotation, and plastic deformation is confined to the section containing the crack. Crack opening areas during normal operation and design-basis accidents are small when compared with the tube cross-sectional area for a steam generator tube with ≤ 240° throughwall crack at the top of the tube sheet.

A model that allows for plastic deformation away from the crack plane is also proposed. The plasticity constitutive law is assumed to be a power-law hardening stress-strain curve. Comparison with finite-element analysis (FEA) shows that the FEA results are closer to those predicted by the model if plasticity is not artificially confined to the crack plane but is allowed to occur away from crack plane also. The predicted shapes of the crack initiation pressure versus crack angle plots by the power-law-hardening model do not generally show the minimums predicted to occur if plasticity is confined to the crack plane.

Although plasticity is confined to the crack section for normal operating and design-basis accident conditions of PWRs, in leak rate and failure tests of steam generator tubes in the laboratory, significant plastic deformation usually occurs away from the crack section. The simplified model, which can account for plastic deformation away from the crack plane, predicts failure pressure curves that are similar to curves derived from test data. The model also predicts a significant increase in the applied tearing modulus with the onset of plastic deformation away from the crack plane; however, failure by unstable tearing is more likely with short cracks (<180°) than with long cracks.

For typical steam generator tubes (span ≈ 24-48 in. [0.6 – 1.2 m]) with critical crack tip opening displacement δ_c >0.03 in. (0.76 mm) (K_{JC} > 200 ksi$\sqrt{in}$ [220 MPa$\sqrt{m}$]) and containing a circumferential throughwall crack at the top of tube sheet, any crack of 180° or less does not reduce the failure pressure from the burst pressure of an unflawed tube. Also, tubes with throughwall cracks ≥ 240° will behave as if they were fully constrained against bending and will have significantly greater failure pressures than the same tubes under free bending condition. Thus, for typical mechanical properties of steam generator tubes, the longest throughwall circumferential cracks at the top of tube sheet that are predicted to experience onset of crack initiation during normal operation and design basis accident conditions are 340° and 310°, respectively. A further conservative factor in the current model is the assumption that the tubes are free to expand or contract in the axial direction at the tube support plates. If, as some experience with real steam generators suggests, the tubes are locked in at the tube support plates and require significant axial loads to pull them during removal from service, the axial tensile force due to internal pressure must first overcome this lock-in force before the circumferential cracks are subjected to any driving force for crack initiation and growth.

6.2 Failure and Leak Rate Tests on SG Tubes with EDM Notches and Stress Corrosion Cracks

Failure and leak rate tests have been conducted on SG tubes with OD part-throughwall EDM notches both at room temperature and at 282°C. Notch length in these tests ranged from 6 mm (0.25 in.) to 38 mm (1.5 in.), and notch depths of 60, 80, and 90% (in addition to 100% throughwall) were tested. These limited tests have shown that the following ANL m_p correlation for predicting ligament rupture pressure of rectangular part-throughwall flaws is valid for tests on tubes with axial notches, either shallow or deep, although more tests with short and deep notches are needed to fully validate the ANL correlation.

$$m_p(\text{ANL}) = \frac{1-\alpha\frac{a}{mh}}{1-\frac{a}{h}} \tag{4a}$$

$$\alpha = 1+0.9\left(\frac{a}{h}\right)^2\left(1-\frac{1}{m}\right), \tag{4b}$$

Further, the leak rates for these tests can be predicted reasonably well using the following formula for smooth circular orifices by simply replacing the orifice area by the notch area (the symbols are explained after each equation in the main body of the report).

$$Q = 0.6A\sqrt{\frac{2\Delta p}{\rho}} \tag{44a}$$

where for axial cracks, A is given by

$$A = 2\pi c_e^2 V_o \sigma / E, \tag{2}$$

and for circumferential cracks, A is given by

$$A = \frac{\pi p R^2}{E} B, \tag{38a}$$

The above set of equations can predict the ligament rupture pressures and leak rates for rectangular EDM notches at both room temperature and 282°C if the appropriate densities of water are used.

An initial series of tests has been performed on laboratory-degraded tubes containing 10-14 mm (0.39–0.55 in.)-long axial ODSCC in 7/8-in. (22-mm)-diameter Alloy 600 tubing. All five flaws tested were very tight and had regions of pretest throughwall penetration as determined by bubble testing. However, in the high-pressure tests, none of the flaws exhibited detectable water leakage until pressures substantially greater than 8.3 MPa (1.2 ksi) were reached. None of the specimens experienced unstable burst up to the maximum system pressure capability of 19.3 MPa (2.8 ksi). Four of the five flaws exhibited crack tip ligament tearing under constant temperature and pressure conditions, which caused the leak rate to increase. Three of the five flaws that had pretest BC voltages of 6-10 V were more rectangular in shape (as indicated by EC + point) than the other two flaws with lower BC voltages (≈4 V),

which had a more triangular shape (as indicated by EC + point). The three specimens with higher voltages tore open along their entire OD length at pressures ≤17.2 MPa (2.5 ksi) and exhibited flow rates in the range 23-38 L/min (6–10 gpm) or more. This behavior suggests that ligament failure with significant leakage rate of an SCC flaw may occur at ≤17.2 Mpa (2.5 ksi) if the crack is sufficiently long and deep. In contrast, the two flaws with lower BC voltages exhibited leak rates of 1.7 L/min (0.45 gpm) or less and did not experience ligament rupture over their full OD axial length.

A procedure for defining an equivalent rectangular crack for an ODSCC with arbitrarily morphology, based on EC +point data, has been developed. Structural and leak rate analyses of the flaws and comparison with experimental data have shown that the ligament failure pressure in laboratory-grown cracks can be predicted reasonably well, using a flow stress model that is strictly applicable to rectangular part-throughwall cracks, by replacing the actual crack profile by an equivalent rectangular crack if failure occurs during the pressure ramp. In these tests, the full ligament ruptured abruptly at the failure pressure and the leak rate did not increase during a constant-pressure hold. Further, the leak rates for these tests could be predicted reasonably well by using the same formula that was used for rectangular notches by simply replacing the notch area by the equivalent rectangular crack area (allowing for change in crack area with pressure). Such a procedure works both at room temperature and at 282°C if the appropriate densities of water are used.

In contrast, initial leakage occurred at a pressure significantly less than that predicted by the equivalent rectangular crack approach if, instead of ramping, the pressure is held constant over a period of time. The experimental evidence of time-dependent initiation and increase of leak rate under constant pressure at both 282°C and at room temperature highlights the fact that a criterion for predicting time-dependent ligament rupture is currently lacking.

6.3 Electrosleeved Tubes under Simulated Severe Accident Loading

Two flow stress-based models have been developed for predicting failure of Electrosleeved tubes under expected severe accident transients. Both models account for the loss of flow stress of the Electrosleeve with aging and predict comparable failure temperatures for both axial and circumferential cracks during a postulated station blackout (SBO) transient. The predicted flow stresses after accounting for aging agree reasonably well with those of Ni 200 at high temperatures. The Hall-Petch model, which is the more mechanistic of the two approaches, was adopted for calculating the failure temperatures of Electrosleeved Alloy 600 tubes with axial and circumferential throughwall cracks subjected to an SBO (Case 6RU) severe accident transient.

Finite-element analyses were conducted to validate the m_p factor used in the model for calculating average ligament stress in single-layer shells with part-through axial cracks. The same model showed that the m_p factor for the Electrosleeve ligament in a 100% throughwall axial crack is reduced when the flow stress of the Electrosleeve is reduced compared to that of the parent tube. The reduction is greater for shorter cracks. To determine the effective m_p factor, the following flow stress and crack length-dependent correction factor (Fig. 40) was applied to the m_p factor calculated with the ANL correlation (Eqs. 4a-b).

$$m_p(\text{eff.}) = \frac{m_p(\text{FEA})}{m_p(\text{FEA}, \text{FSR} = 1)} \times m_p(\text{ANL}). \tag{46b}$$

Failure under any prescribed temperature T and hoop stress σ_h history is predicted when the following equations are satisfied

$$m_p(\text{eff.})\sigma_h = H(t) \tag{45a-b}$$

where

$$H(t) = \begin{cases} H_i(t) & \text{for } t < t_n \\ \left[1 + \frac{2B}{d_i^2}\int_{t_n}^{t} \exp\left(\frac{-Q}{RT(t)}\right)dt\right]^{-n/2} H_i(t) & \text{for } t \geq t_n, \end{cases} \tag{54}$$

$H_i(T)$ is given in Fig. 55, Q in Fig. 42, and the nucleation time t_n is obtained from

$$C\int_0^{t_n} \exp\left(\frac{-Q}{RT(t)}\right)dt = 1. \tag{52}$$

Eleven high-temperature tests simulating an SBO (Case 6RU) pressure and temperature ramp have been conducted on notched Electrosleeved tubes supplied by FTI. The test results indicate a leveling-off of failure temperature with notch length beyond 51 to 76 mm (2 to 3 in.), which is consistent with the FEA results. The flow stress data supplied by FTI, together with the ANL test results, were used to derive an unaged flow stress curve of the Electrosleeve from room temperature to high temperatures. The unaged flow stress curve was used in the model for predicting failure. All of the test data fall within the upper and lower bounds calculated on the basis of limiting geometrical parameters observed in the specimens. Also, high-temperature test data on notched unsleeved, as well as on notched Electrosleeved, tubes reported by FTI can be predicted reasonably well by the flow stress model.

A sensitivity analysis showed that the predicted failure temperatures are increased significantly if the depth of the crack in the parent tube is <90% throughwall. The temperature will also increase if the thickness of the Electrosleeve is increased. FEA calculations and ANL tests suggest that the adverse-crack-length effect should level off at 51 to 76 mm (2 to 3 in.). The model predicts a continuing reduction of failure temperature with increasing crack length. However, the additional reduction in predicted failure temperature from a crack length of 76 to 152 mm (3 to 6 in.) is only 5°C.

The proposed model with the unaged flow stress curve of the Electrosleeve reported here is valid for temperature ramps that are not significantly different from the ramp rate (12.5°C/min) used in the ANL tests because creep effects are neglected in the model. The rate effect that is predicted by the model is due to grain growth only. Predicted failure temperatures at ramp rates significantly different from 12.5°C/min will be accurate if grain growth effects predominate over creep effects.

The ligament rupture criterion based on flow stress of the ligament used in the present report was developed from analyses and tests on part-throughwall cracks in single-layer shells. The application of the flow stress criterion to a composite structure by using the flow

stress of the weaker Electrosleeve without any credit given to the stronger parent tube may be conservative, particularly for a highly ductile material such as the Electrosleeve. However, all of the ANL and FTI tests that did not include constant-temperature holds are consistent with the flow stress failure criterion. If prediction of failure under an arbitrarily varying temperature history is of interest, a creep-rupture-based model coupled with a grain growth model may be needed.

References

1. J. F. Kiefner, W. A. Maxey, R. J. Eiber, and A. R. Duffy, "Failure stress levels of flaws in pressurized cylinders," in *Progress in Flaw Growth and Fracture Toughness Testing*, Kaufman, J. G., ed., National Symposium on Fracture Mechanics (6th : 1972 : Philadelphia), American Society for Testing and Materials, Committee E–24 on Fracture Testing of Metals, American Society for Testing and Materials, ASTM Special Technical Publication 536, Philadelphia, 1973.

2. B. Flesch and B. Cochet, "Crack stability criteria in steam generator tubes," *Int. Cong. On Pressure Vessel Technology*, Beijing, Sept. 1988.

3. J. M. Alzheimer, R. A. Clark, C. J. Morris, and M. Vagins, Steam Generator Tube Integrity Program Phase I Report, NUREG/CR–0718, PNL-2937, Richland, WA, Sept., 1979.

4. S. Majumdar, W. J. Shack, D.R. Diercks, K. Mruk, J. Franklin, and L. Knoblich, "Failure Behavior of Internally Pressurized Flawed and Unflawed Steam Generator Tubing at High Temperatures – Experiments and Comparison with Model Predictions," NUREG/CR–6575, ANL–97/17, Argonne, IL, 1998.

5. SGTR Severe Accident Working Group, "Risk Assessment of Severe Accident-Induced Steam Generator Tube Rupture," NUREG-1570, U.S. Nuclear Regulatory Commission, Washington DC, 1998.

6. S. Ranganath and H. S. Mehta, "Engineering methods for the assessment of ductile fracture margin in nuclear power plant piping," Fracture Resistance Curves and Engineering Applications, ASTM STP 803, Philadelphia, 1983.

7. P. Hernalsteen, "Structural and Leakage Integrity of Tubes Affected by Circumferential Cracking," Proc. of the CNRA/CSNI Workshop on Steam Generator Tube Integrity in Nuclear Power Plants, Oak Brook, IL, Oct. 30-Nov. 2, 1995, NUREG/CP-0154, 1997.

8. G. M. Wilkowski et al., "Degraded-Piping Program – Phase II," Semiannual Report, NUREG/CR-4082, Vols. 1-8, USNRC, Washington, DC, 1984-1989.

9. G. M. Wilkowski et al., "Short Cracks in Piping and Piping Welds," Semiannual Report, NUREG/CR-4599, Vols. 1-3, USNRC, Washington, DC, 1991-1994.

10. H. Tada, P. C. Paris, and R. M. Gamble, "A stability analysis of circumferential cracks for reactor piping systems," Fracture Mechanics, ASTM STP 700, Philadelphia, 1980.

11. E. Smith, "The effect of axial forces on the conservatism of the net-section stress criterion for the failure of cracked stainless steel piping," SmiRT-12, Vol. G, pp. 57-62, 1993.

12. E. Smith, "Leakage via a through-wall circumferential crack in a piping or tubing system under accidental loading conditions," Int. J. Pressure Vessels and Piping, Vol. 75, pp. 121-124, 1998.

13. E. Smith, "Factors influencing the crack-system compliance of a piping system," Int. J. Pressure Vessels and Piping, Vol. 75, pp. 125–129, 1998.

14. G. T. Hahn, M. Sarrate, and A. R. Rosenfield, "Criteria for crack extension in cylindrical pressure vessels," Int. J. Fracture Mech. **5**, No. 3, pp. 187–210, 1969.

15. F. Erdogan, "Ductile failure theories for pressurized pipes and containers," Int. J. of Pres. Ves. & Piping, Vol. **4**, pp. 253–283, 1976.

16. A. Zahoor, *Ductile Fracture Handbook*, Electric Power Research Institute, Palo Alto, CA, 1989.

17. M. F. Kanninen, A. Zahoor, G. M. Wilkowski, I. Abou-Sayed, C. Marschall, D. Broek, S. Sampath, C. Rhee, and J. Ahmad, "Instability Predictions for Circumferentially Cracked Type 304 Stainless Steel Pipes under Dynamic Loading," EPRI NP–2347 (Vol. 1: Summary; Vol. 2: Appendices), Electric Power Research Institute, Palo Alto, CA, April 1982.

18. B. Cochet, J. Engstrom, and B. Flesch, "PWR Steam generator tube and tube support plate plugging criteria," Paper 4.1, Steam Generator Tubes Mechanical, LBRB, and Probabilistic Studies, EDF, France, 1990.

19. G. Wilkowski, J. Ahmad, D. Barnes, F. Brust, N. Ghadiali, D. Guerrieri, J. Kiefner, G. Kramer, M. Landow and C. Marschall, "Degraded Piping Program – Phase II Progress," 13th Water Reactor Safety Research Information Meeting, Oct 22-25 1985, Gaithersburg, MD, Nucl. Eng. and Des., Vol. 98, pp. 195-217, 1987.

20. P. Hernalsteen, presented at the NEA/CNRA/CSNI Workshop on Steam Generator Integrity in Nuclear Power Plants, Oak Brook, IL, Oct. 30-Nov. 2, 1995.

21. P. C. Paris and H. Tada, "The application of fracture proof design methods using tearing instability theory to nuclear piping postulating circumferential throughwall cracks," NUREG/CR-3464, USNRC, Washington, DC, 1983.

22. R. Kurihara, S. Ueda, and D. Sturm, "Estimation of the ductile unstable fracture of pipe with a circumferential surface crack subjected to bending," Nucl. Eng. Design, Vol. 106, 1988.

23. K. E. Kasza, S. Majumdar, and J. Muscara, "Steam Generator Tube Integrity Testing/Analysis," Presented at SmiRT-15 Conference in Seoul, Korea, 1999.

Table 1. *Effective lengths of tubes for several circumferential crack locations and edge conditions*

Edge conditions and crack location	Effective length
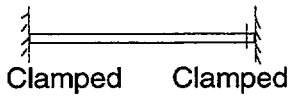	$L_e = L/4$
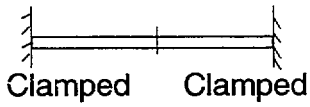	$L_e = L$
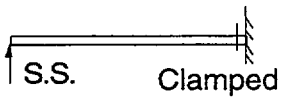	$L_e = L/3$

Spec. No.	Material Condition	Flaw Length (in./mm)	Flaw Depth (%)	Test Temp. (°C)	Failure Pressure (ksi/MPa)	Pres. During Leak Rate Meas. (ksi/MPa)	Leak Rate (gpm/[L/min])
T4E	As-Received	1.5/38	80	20	2.5/17.2[a]	1.75/12.2	388/1474
T7E	As-Received	1.5/38	80	20	2.4/16.5[a]		384/1459
T14E	As-Received	1.0/25	100	20	-	2.0/13.8	80/303
				20	2.3/15.9[a]	1.85/12.8	290/1102
T2E	As-Received	0.5/13	100	20		1.5/10.3	2.9/11.0
				20		2.0/13.8	5.9/22.4
				20		2.8/19.3	7.7/29.3
TE1	As-Received	0.5/13	100	282	-	2.0/13.8	6.4/24.3
T13E	As-received	0.35/9	91	20		2.8/19.3	0
				282		2.8/19.3	0
T3E	Heat-Treated	1.5/38	80	20	2.0/13.8[a]	1.5/10.3	424/1611
TE2	Heat-Treated	0.5/13	100	20	-	2.0/13.8	13/49.4
T24	As-Received	2 x 0.25/6.0	100	20		2.1/14.5	3.9/14.8
		Lig.=0.01/0.25		20		2.5/17.2	4/9/18.6
T25	As-Received	2 x 0.25/6.0	100	282	-	2.1/14.5	4.5/17.1
		Lig.=0.01/0.25		282	2.25/15.5	2.5/17.2	8.5/32.3
				282	[b]	2.6/18.0	9.4/35.7
OM 118	As-Received	0.25/6	60	20	6.9/47.6[a]		
OM 116	As-Received	0.25/6	80	20	5.5/37.9[b]	6.4/44.1	11.9/45.2
OM 138	As-Received	0.25/6	90	20	4.35/30.0	6.26/43.2	11.8/45.0
OM120	As-Received	0.5/13	80	20	3.9/26.9[b]		
OM121[c]	As-Received	0.5/13	80	20	4.2/29.0[a]		
OM107	As-Received	0.75/19	80	20	3.1/21.4[b]		
OM123[c]	As-Received	0.75/19	80	20	3.18/21.9[a]		

[a]Unstable burst pressure [b]Ligament failure pressure [c]Tested with bladder

Table 2. Summary of notched (EDM) specimens tested in Pressure and Leak Rate Facility and High-Pressure Test Facility (last 7 tests)

Test no.	Initial OD Flaw Length (in/mm)	Test Temp. (°C)	Initial Leakage Conditions		Constant Pressure Hold Conditions			Final Test Conditions	
			Pressure (ksi/MPa)	Flow Rate (gpm/[L/min])	Pressure (ksi/MPa)	Flow Rate (gpm/[L/min]) Initial	Flow Rate (gpm/[L/min]) Final	Pressure (ksi/MPa)	Flow Rate (gpm/[L/min])
177	0.48/12.2	RT	2.45/16.9	No leakage	2.45/16.9	0.01/ 0.04[a]	0.26	2.8/19.3	0.44/1.7
195	0.54/13.7	RT	2.13/14.7	No leakage	2.13/14.7	<0.01/ 0.04	<0.01/ 0.04	2.25/15.5	8.6/32.7[b]
104	0.41/10.4	282	2.35/16.2	5.6/21.3	2.35/16.2	5.6/ 21.3	5.6/ 21.3	2.5/17.2	6.2/23.6
219	0.55/14.0	282	1.93/13.3	1.0/3.8	2.35/16.2	3.7/ 14.1	10.3/ 39.1	2.35/16.2	10.3/39.1
2-10 (W)	0.49/12.4	RT	2.5/17.2	No leakage	2.5/17.2	0.01/ 0.04[c]	0.018/ 0.068[c]	2.5/17.2	0.018/ 0.068
2-10 (W)[d]	0.49/12.4	282	2.7/18.6	0.03/0.12	2.7/18.6	0.03/ 0.12	0.19/ 0.72	2.7/18.6	0.19/0.72

[a] Leakage started after 100 min hold.

[b] Flow rate increased abruptly

[c] Leakage started after 3 h hold and increased gradually for additional 24 h hold

[d] Same specimen tested at 282°C

Table 3. Summary of tests on specimens with ODSCC tested in Pressure and Leak Rate Test Facility

Test No.	Final test pressure MPa (ksi)	Meaured leak rate L/min (gpm)	Estimated final throughwall crack length mm (in.)	Corrected leak rate at test pressure L/min (gpm)	Test pressure adjusted for flow stress MPa (ksi)	Predicted leak rate at adjusted pressure L/min (gpm)
177[a,b]	19.3 (2.8)	1.67 (0.44)	5.61 (0.22)	0.70 (0.18)	23.2 (3.4)	1.2 (0.31)
195[a]	15.5 (2.25)	32.7 (8.6)	12.1 (0.48)	7.9 (2.1)	18.6 (2.7)	15.7 (4.1)
104[b]	17.2 (2.5)	23.6 (6.2)	9.7 (0.38)	5.5 (1.4)	20.7 (3.0)	11.1 (2.9)
219[b,c]	16.2 (2.35)	39.1 (10.3)	11.1 (0.44)	8.5 (2.3)	19.4 (2.8)	17.5 (4.6)

[a]This test was conducted at 20°C.

[b]This test showed evidence of time-dependent ligament rupture.

[c]This test was conducted at 282°C.

Table 4. Summary of estimated leak rates, corrected for flow stress, of ANL tests on heat-treated Alloy 600 steam generator tubes with laboratory-grown SCC cracks.

	Electrosleeved Alloy 600 tube 100%TW crack length			Unsleeved Alloy 600 tube		
	13 mm (0.5 in.)	25 mm (1 in.)	51 mm (2 in.)	50% TW 51 mm (2 in.)	50% uniform thinning	Undegraded
Observed failure temp.	731°C	691°C	611°C	727°C	724°C	82 min[a]
Predicted failure temp.	766°C	728°C	682°C	738°C	726°C	164 min[b]

[a]This test was held at 764°C until it failed after 82 min.

[b]Predicted by creep rupture model of Ref. 4.

Table 5. Observed and initial predictions of failure temperatures for FTI severe-accident tests on unsleeved and Electrosleeved tubes.

Test No.	Notch length mm (in.)	Notch depth mm (in.)	Tube wall thickness mm (in.)	Electrosleeve thickness mm (in.)	Failure temperature (°C)
BTF-21	13 (0.5)	1.24 (0.0490)	1.24 (0.0490)	1.04 (0.0410)	807
BTF-13	13 (0.5)	1.25 (0.0492)	1.30 (0.051)	1.02 (0.0400)	806
BTF-4	25 (1.0)	1.22 (0.0482)	1.30 (0.051)	0.99 (0.0390)	722
BTF-10	25 (1.0)	1.27 (0.0500)	1.32 (0.0520)	0.97 (0.0380)	724
BTF-14	25 (1.0)	1.24 (0.0490)	1.27 (0.0500)	0.99 (0.0390)	714
BTF-19	51 (2.0)	1.24 (0.0490)	1.30 (0.051)	1.02 (0.0400)	680
BTF-22	51 (2.0)	1.26 (0.0495)	1.27 (0.0500)	0.97 (0.0380)	653
BTF-20	51 (2.0)	1.24 (0.0490)	1.30 (0.051)	0.94 (0.0370)	653
BTF-18	76 (3.0)	1.28 (0.0503)	1.28 (0.0505)	1.00 (0.0395)	643
BTF-17	76 (3.0)	1.25 (0.0493)	1.30 (0.051)	0.89 (0.0350)	630
BTF-5[a]	76 (3.0)	1.24 (0.0490)	1.24 (0.0490)	1.12 (0.0440)	673
BTF-23[b]	13 (0.5)	1.24 (0.0490)	1.27 (0.0500)	0.89 (0.0350)	731
BTF-25[b]	25 (1.0)	1.30 (0.051)	1.30 (0.051)	0.91 (0.036)	691
R.5.2[b]	51 (2.0)	1.30 (0.051)	1.27 (0.0500)	0.91 (0.036)	611

[a]One tip of notch in this specimen was ≈0.1 in. from end of Electrosleeve.

[b]These tests were conducted by FTI.

Table 6 Summary of simulated severe accident tests conducted at ANL and FTI on notched Electrosleeved tubes

Ramp rate (°C/min)	Flow stress model (°C)	Creep rupture model (°C)
1	681	683
5	681	728
5 to 670°C, then 2	681	707
4.2 to 545°C, then 12.5	681	756

Table 7. Predicted failure temperatures by flow stress model and creep rupture model for unsleeved tube with $3\Delta p_{NO}$ crack subjected to various temperature transients and constant internal pressure of 2.35 ksi (16.2 MPa)

Test No.	Tube wall thickness mm (in.)	Electrosleeve Thickness mm (in.)	Crack length mm (in.)	Crack depth mm (in.)	Test failure temp. (°C)	Predicted failure temp. (°C)
BTF-3[a]	1.27 (0.050)	0.99 (0.039)	44.7 (1.76)[b]	1.04 (0.041)[b]	689	692
BTF-7[a]	1.32 (0.052)	0.97 (0.038)	51 (2)[b]	1.09 (0.043)[b]	699	678
BTF-16	1.32 (0.052)	0.97 (0.038)	51 (2)	1.14 (0.045)	675	678

[a]These tests were conducted by FTI.

[b]Equivalent crack length and depth of trapezoidal flaws.

Table 8. Summary of simulated severe accident tests conducted at ANL and FTI on part-throughwall notched Electrosleeved tube

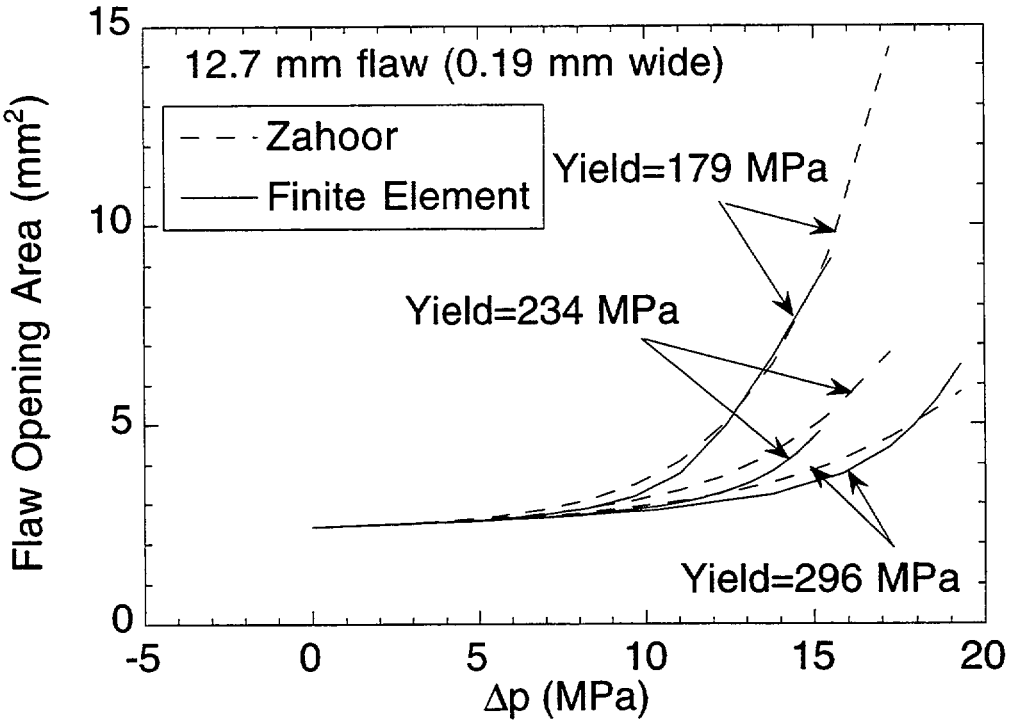

Fig. 1. Predicted crack opening areas by FEA (finite deformation) vs. those predicted by the Zahoor model of 12.7 mm (0.5 in.) long throughwall axial crack for yield stress values of 179 MPa (26 ksi), 234 MPa (34 ksi) and 296 MPa (43 ksi)

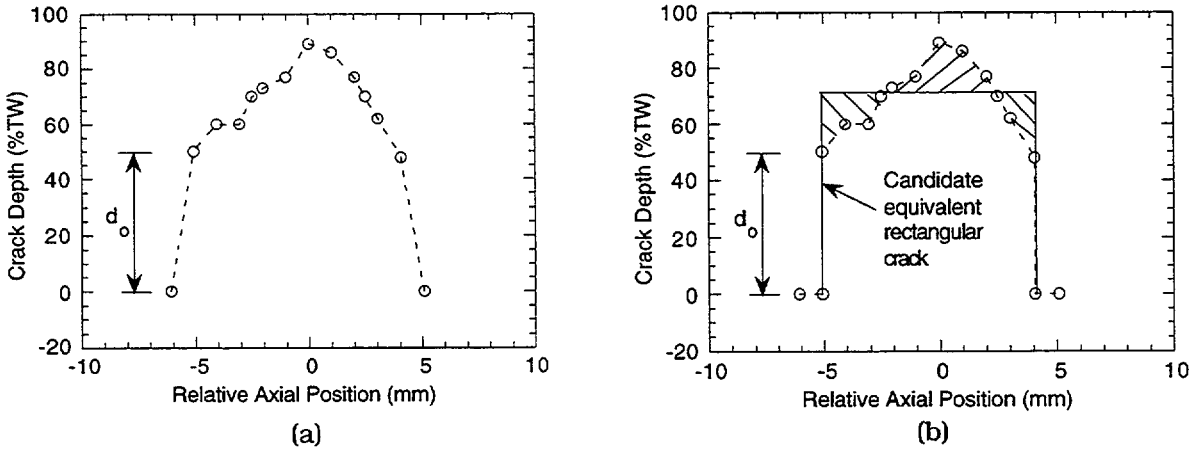

Fig. 2. (a) Crack depth profile in Specimen SGL-177 as measured by Eddy Current +Point and (b) a candidate equivalent rectangular crack corresponding to depth d_o = 50%.

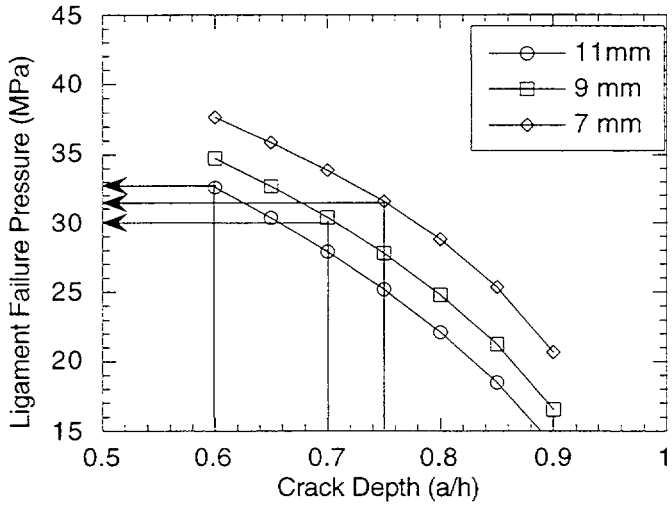

Fig. 3. Ligament rupture pressures corresponding to three candidate equivalent rectangular cracks, 11 mm by 60%, 9 mm by 70%, and 7 mm by 75%. Equivalent rectangular crack for SGL-177 is 9 mm by 70% because it corresponds to lowest ligament rupture pressure (30 MPa).

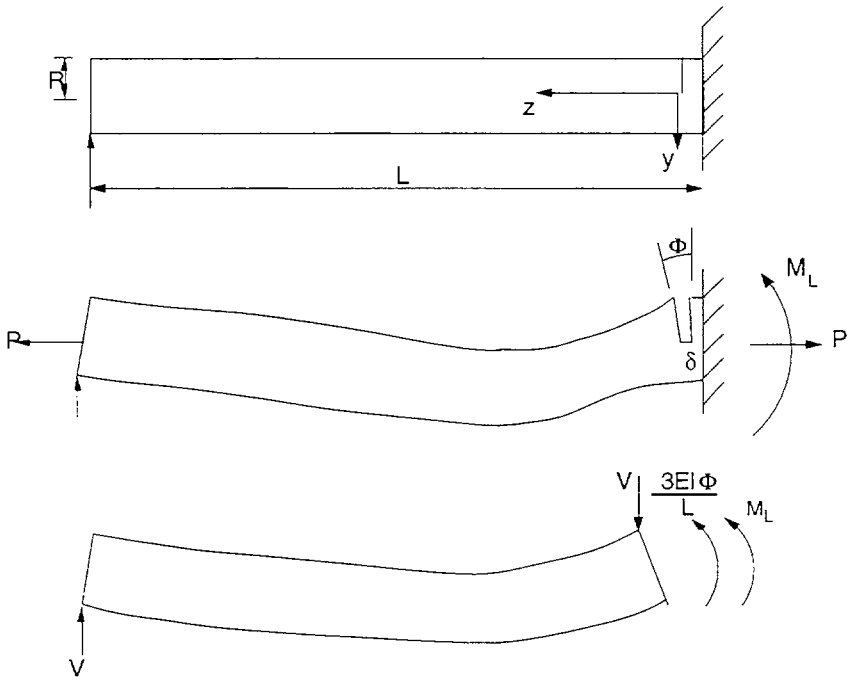

Fig. 4. Geometry, loading, and idealized deformation of tube with single throughwall circumferential crack

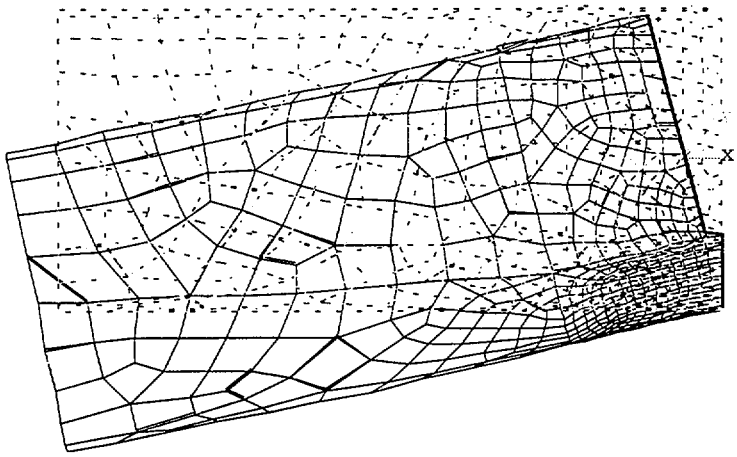

Fig. 5. Calculated (by FEA) displaced (solid line) and original (dashed line) shape of laterally supported tube (L/R=26) with single 240° throughwall circumferential crack at clamped edge.

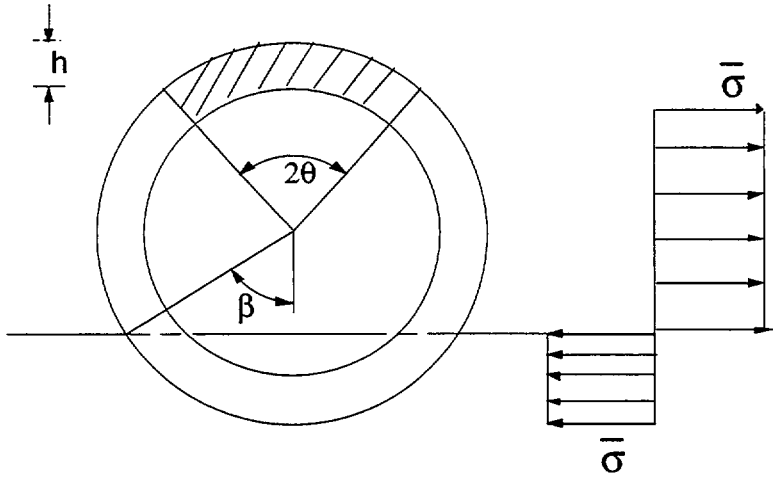

Fig. 6. Stress distribution through section at collapse of tube with single throughwall circumferential crack

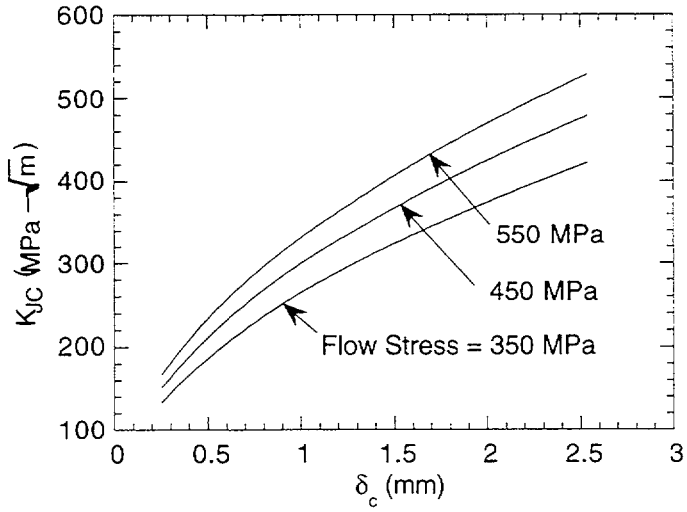

Fig. 7. Variation of fracture toughness with critical crack tip opening displacement for material with $E = 2 \times 10^5$ MPa.

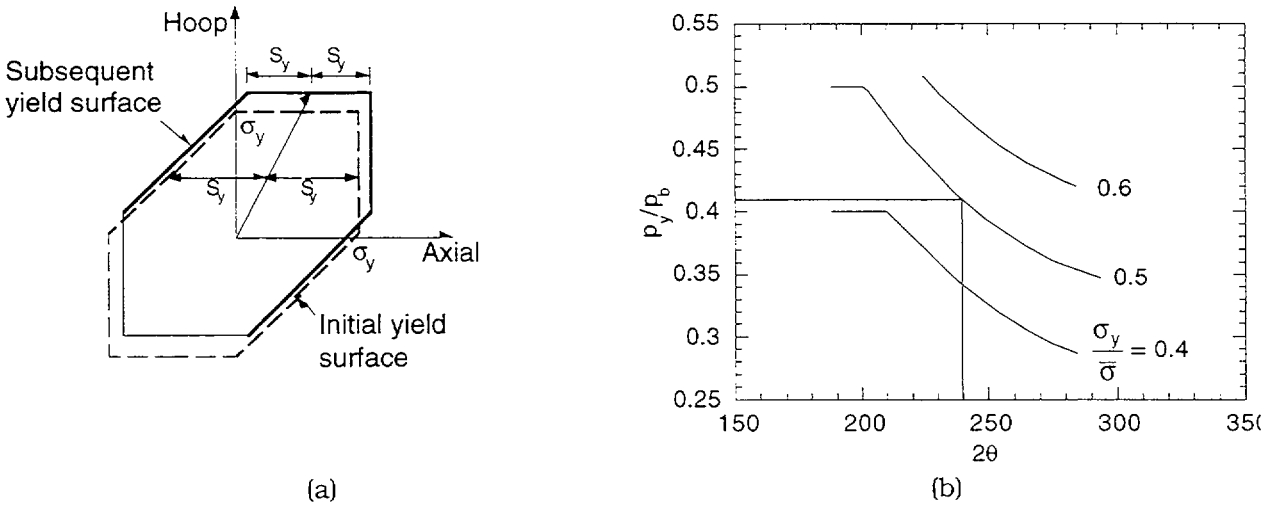

Fig. 8. (a) Determination of axial yield strength S_y for bending analysis using Tresca criterion and (b) predicted variation of pressure to cause initial yielding of the tube away from the crack plane with crack angle as a function of ratio between yield to flow stress

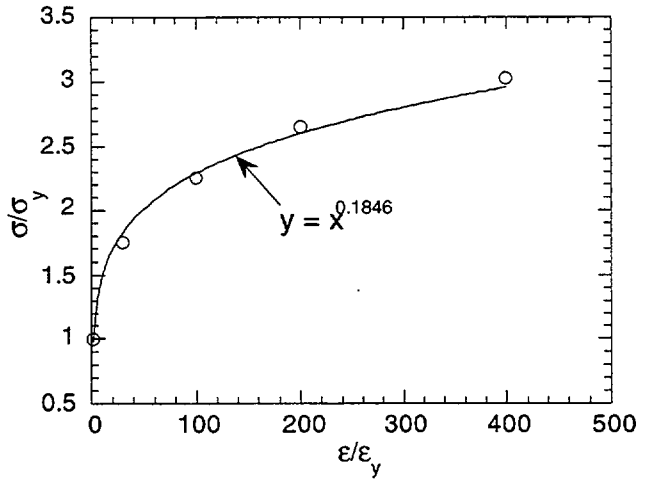

Fig. 9. Normalized uniaxial stress-strain curve (symbols used in FEA) and power-law fit.

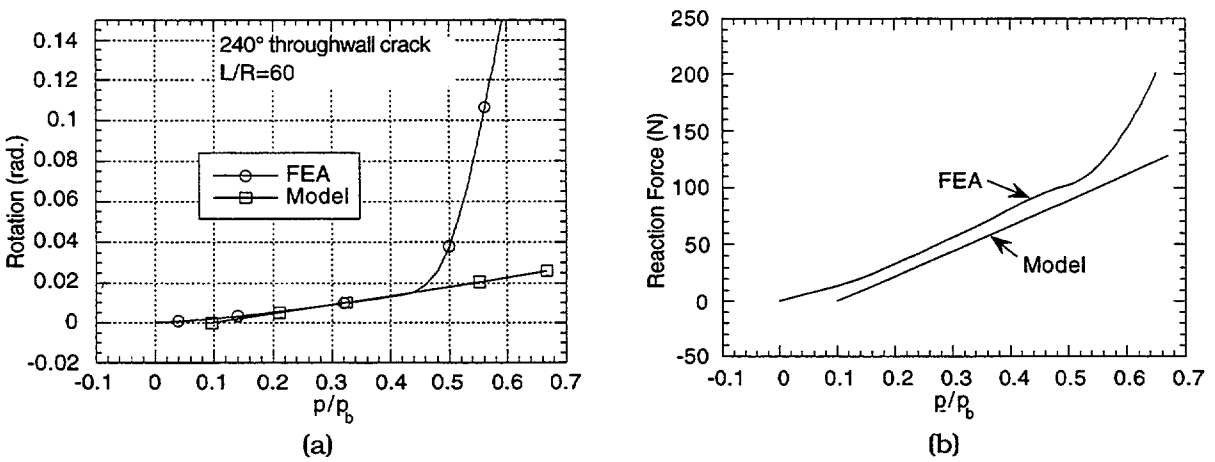

Fig. 10. Comparison of model prediction and elastic-plastic FEA results ($\sigma_Y / \bar{\sigma} = 0.5$) for (a) crack section rotation and (b) support reaction force of tube simply supported at one end and clamped at the other (as in Fig. 4) at various normalized pressures.

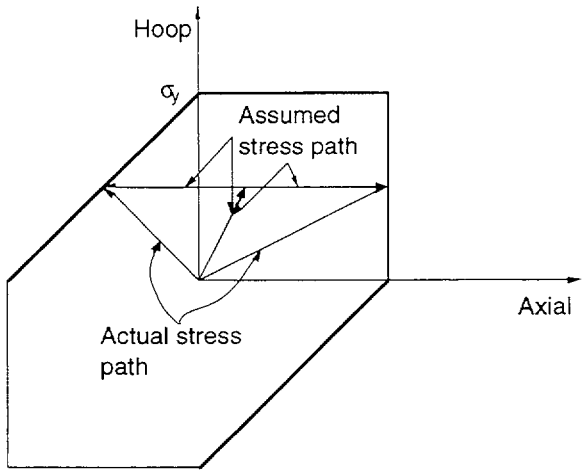

Fig. 11. Radial loading path used in FEA is replaced in model by nonradial path consisting of loading to final pressure (at 2 to 1 stress ratio) followed by applying axial bending stress at constant hoop stress.

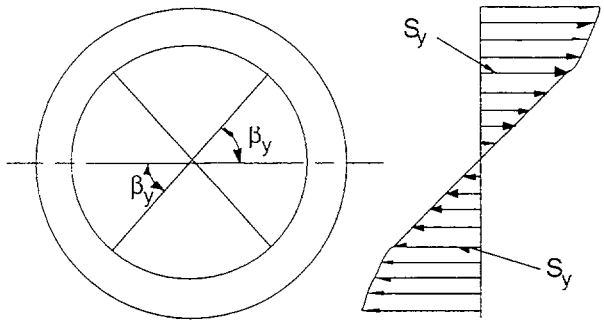

Fig. 12. Nonlinear stress distribution through section away from crack section after yield for power-law hardening material.

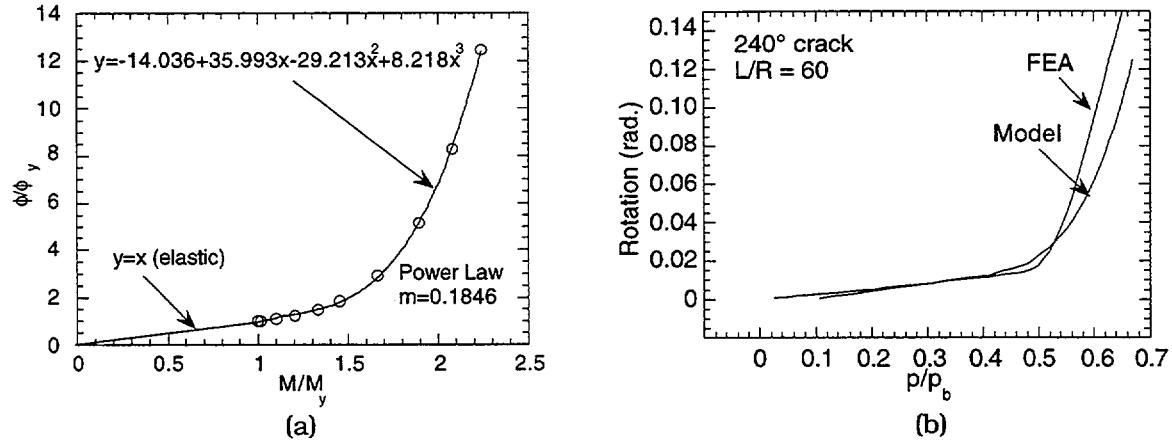

Fig. 13. (a) Model-calculated normalized rotation vs. applied bending moment for configuration of Fig. 4 and a polynomial fit to results, and (b) variation of crack section rotation with normalized pressure as calculated by FEA (σ_y / $\bar{\sigma}$ = 0.5) and those calculated by model that allows for plastic yielding away from crack plane.

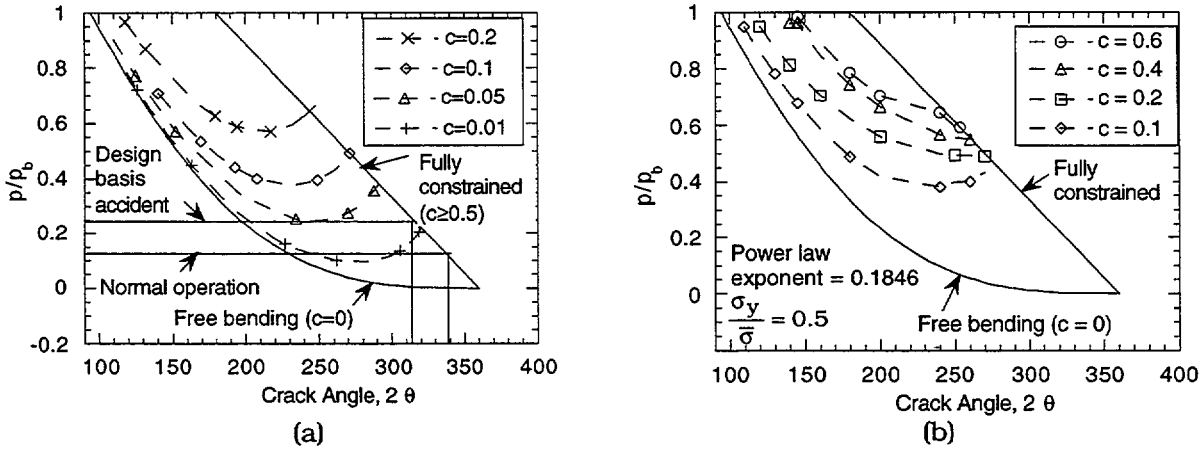

Fig. 14. Variation of failure pressure, normalized by unflawed burst pressure, of tube with crack angle of single throughwall circumferential crack (a) with plasticity confined to crack plane and (b) allowing for plastic yielding away from crack plane.

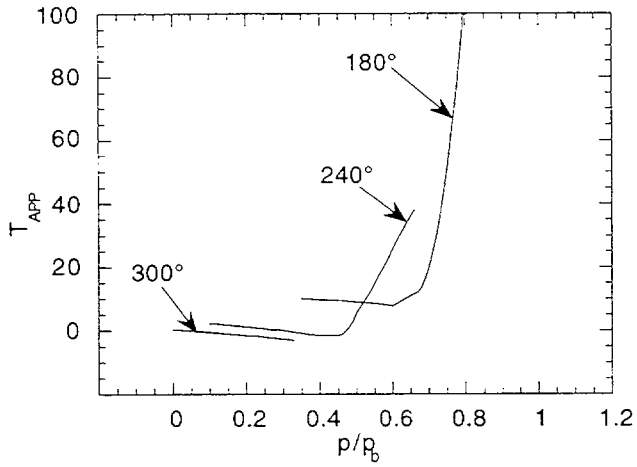

Fig. 15. Calculated variation of applied tearing modulus with pressure, normalized by unflawed burst pressure, for single 180°, 240°, and 300° throughwall circumferential cracks in a tube, using power-law hardening stress-strain curve.

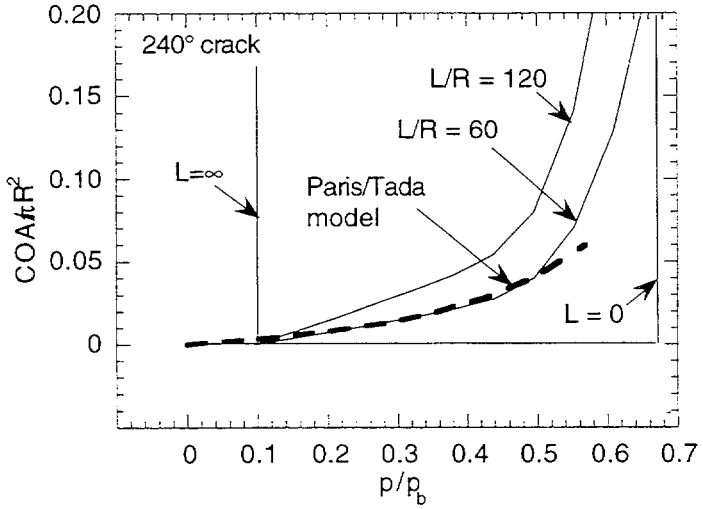

Fig. 16. Normalized crack opening area vs. pressure plots calculated by Paris/Tada model (dashed line) and by current model (solid lines) for L/R = 0 (fully constrained), 60, 120, and infinitely (free-bending) long simply-supported-clamped tube with 240° crack at clamped edge.

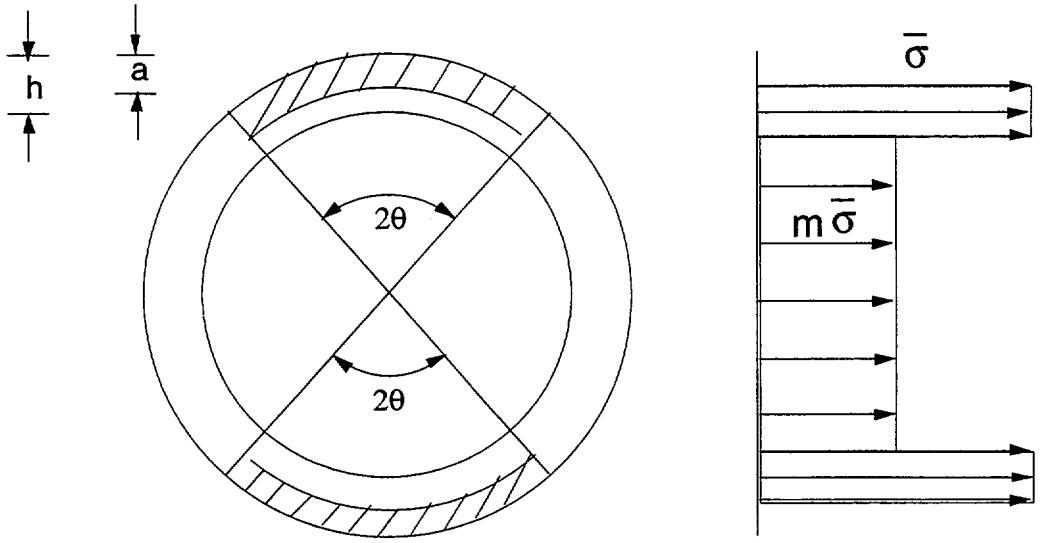

(a)

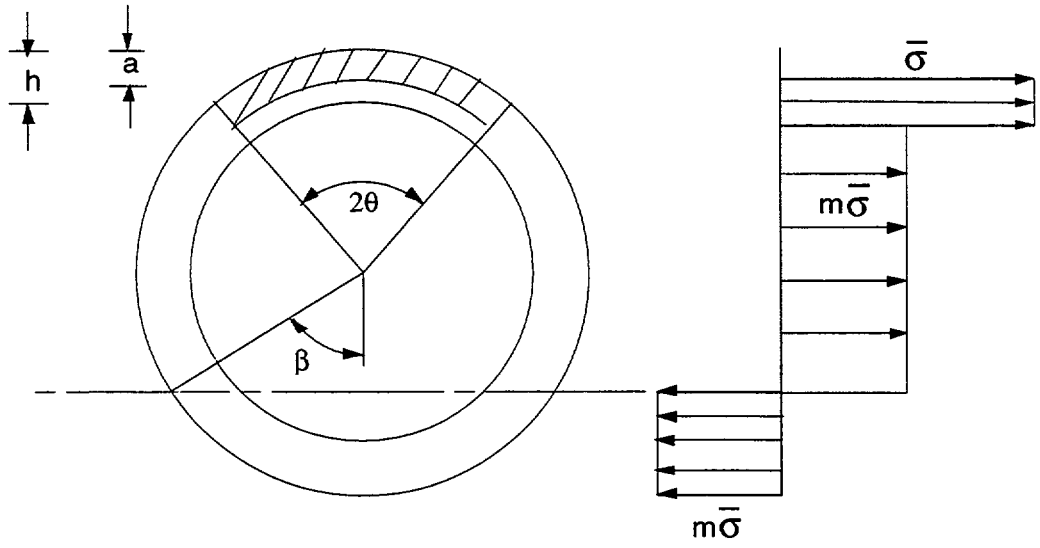

(b)

Fig. 17. Stress distributions through section at failure of tubes with (a) two symmetrically located part-through circumferential cracks and (b) single part-through circumferential crack.

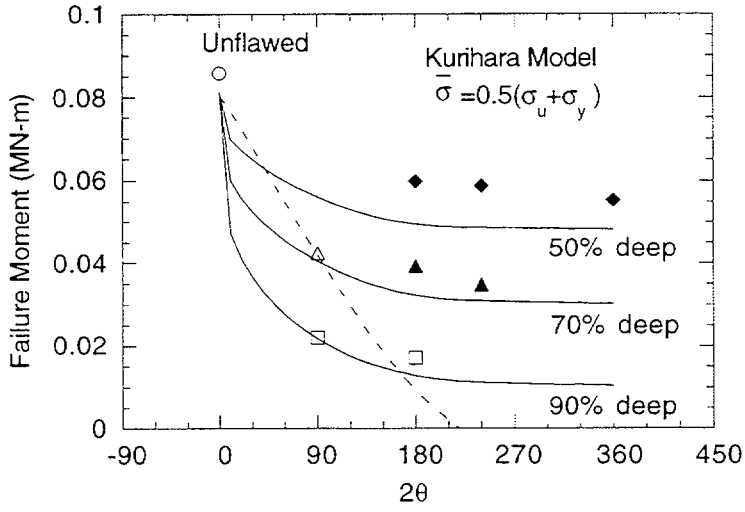

(a)

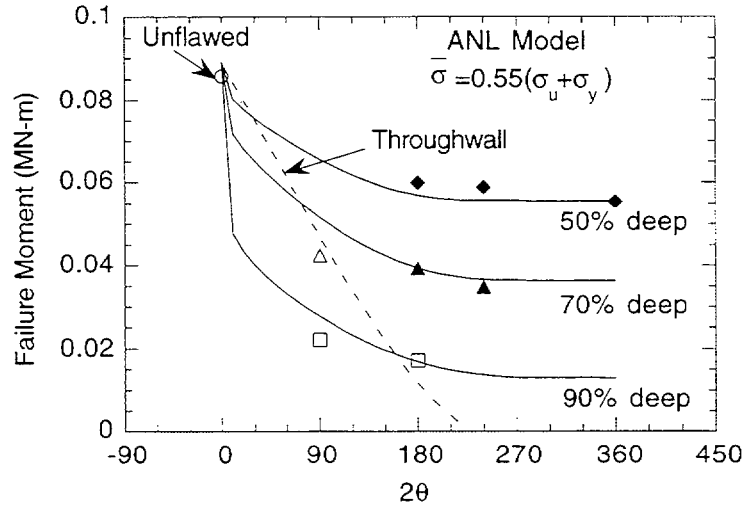

(b)

Fig. 18. Variations of experimental failure bending moments with crack angle and those predicted by (a) Kurihara model and (b) ANL model for unsymmetrical part-through circumferentially cracked 165.2-mm-diameter (11-mm wall thickness) pipe specimens subjected to four-point bend test with constant internal pressure of 6.9 MPa (1000 psi) at room temperature. Dashed lines denote predicted failure bending moments for throughwall cracks; open symbols denote tests that failed by leakage, and filled symbols denote those that failed by breaking into two pieces.

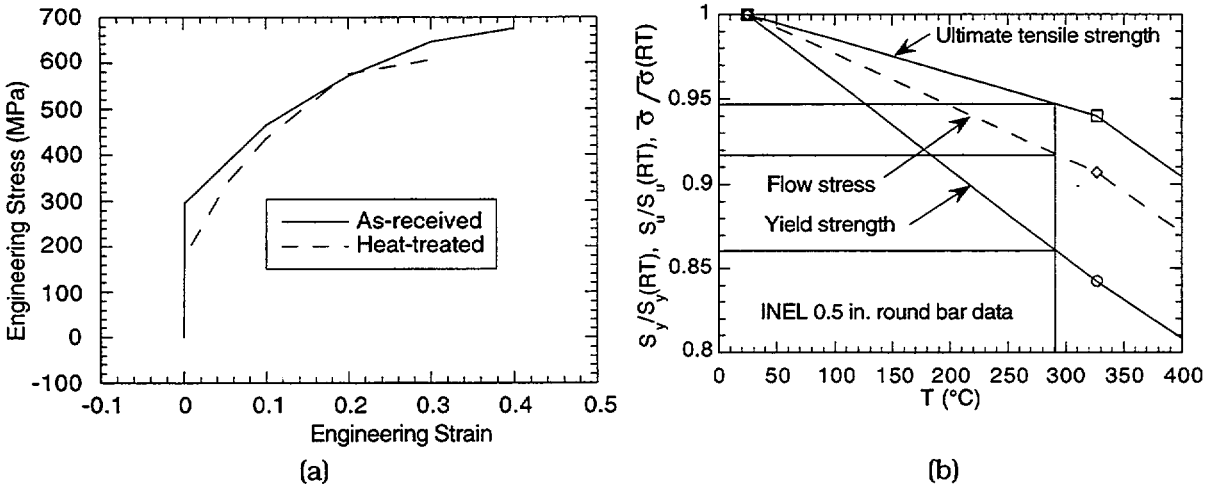

Fig. 19. (a) Engineering stress-strain curves for as-received and heat treated Alloy 600 at room temperature and (b) estimated reduction of flow properties with temperature.

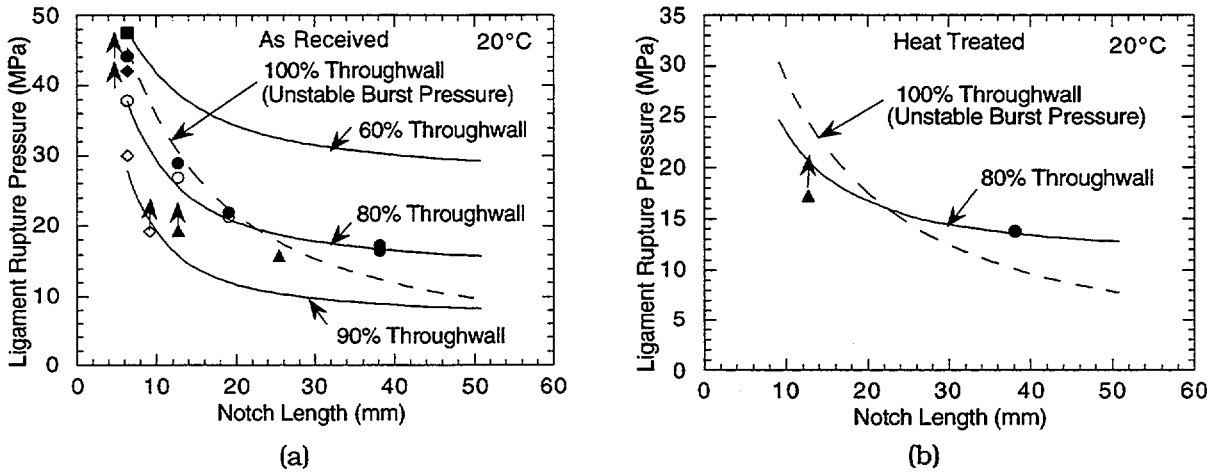

Fig. 20. Predicted vs. observed ligament rupture pressures for notched (a) as-received and (b) heat-treated tubes tested at 20°C. Arrows indicate no failure. Square, circles, diamond, and triangles indicate specimens with 60%, 80%, 90%, and 100% throughwall notches, respectively. Open symbols denote ligament rupture, and filled symbols denote unstable burst.

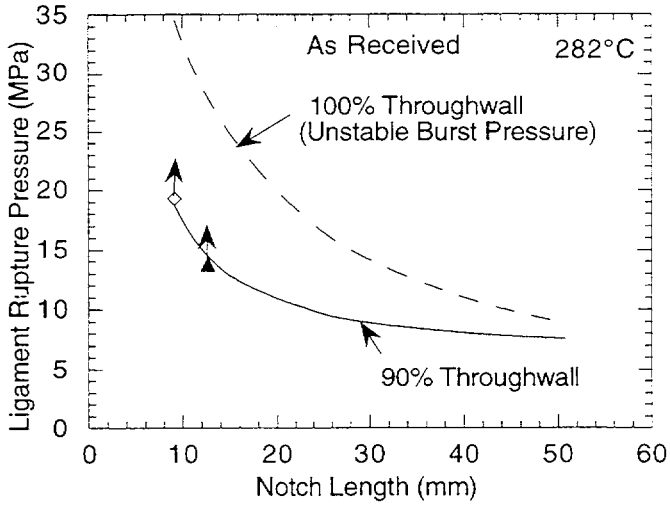

Fig. 21. Predicted vs. observed ligament rupture pressures for notched as-received tubes tested at 282°C. Arrow indicates no failure. Diamond and triangle indicate specimens with 90% and 100% throughwall notches, respectively. Open symbol denotes ligament rupture, and filled symbol denotes unstable burst.

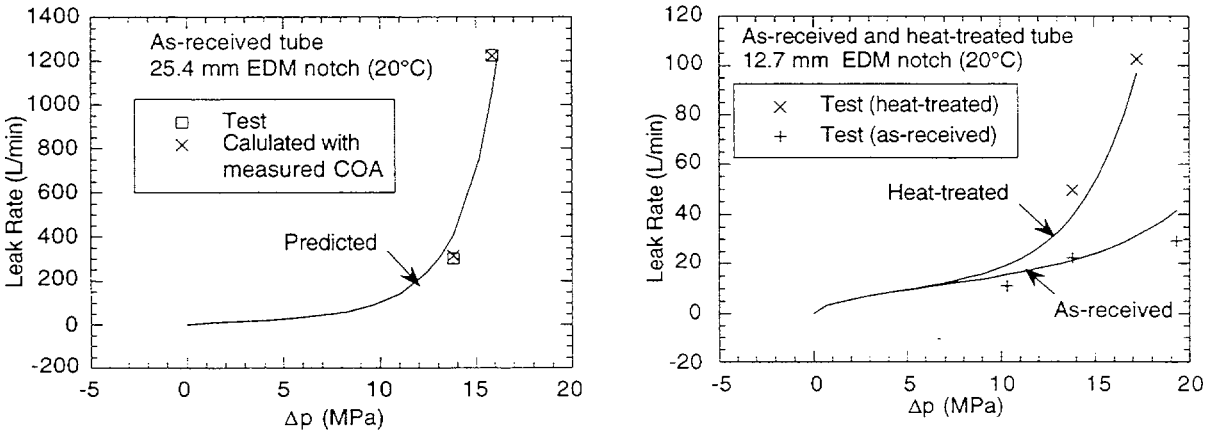

Fig. 22. Comparison of calculated (solid line) vs. experimentally measured (symbols) leak rates at 20°C for as-received and heat-treated 22-mm (7/8 in.)-diameter tubes with (a) 25.4 mm (1 in.) and (b) 12.7 mm (0.5 in.) throughwall axial EDM notches. Cross symbols (x) in Fig. 22a denote calculated leak rates using posttest measured crack opening areas.

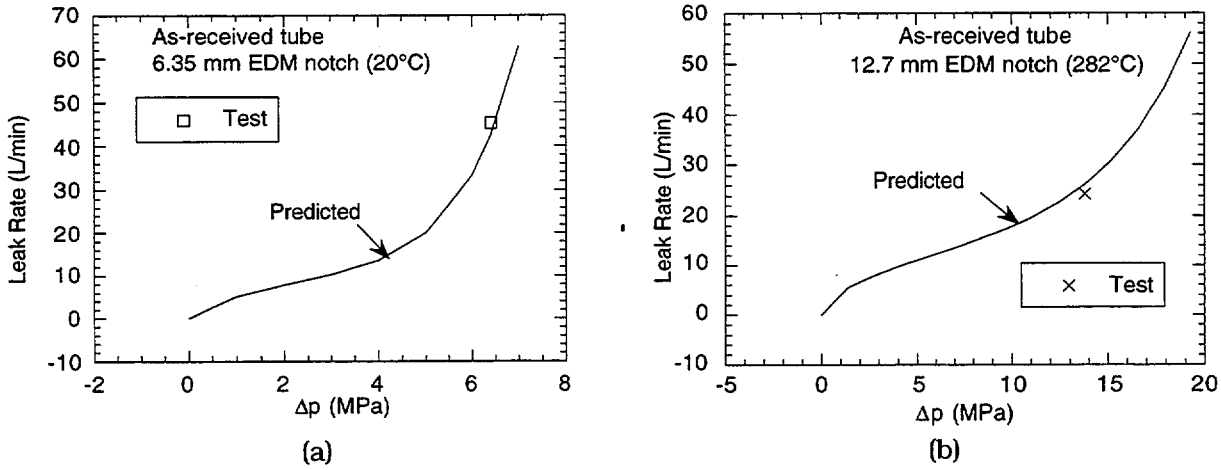

Fig. 23. Calculated (solid line) vs. experimentally measured (symbol) leak rates in as-received 22-mm (7/8 in.)-diameter tubes with (a) 6.35 mm (0.25 in.) flaw at 20°C and (b) 12.7 mm (0.5 in.) flaw at 282°C.

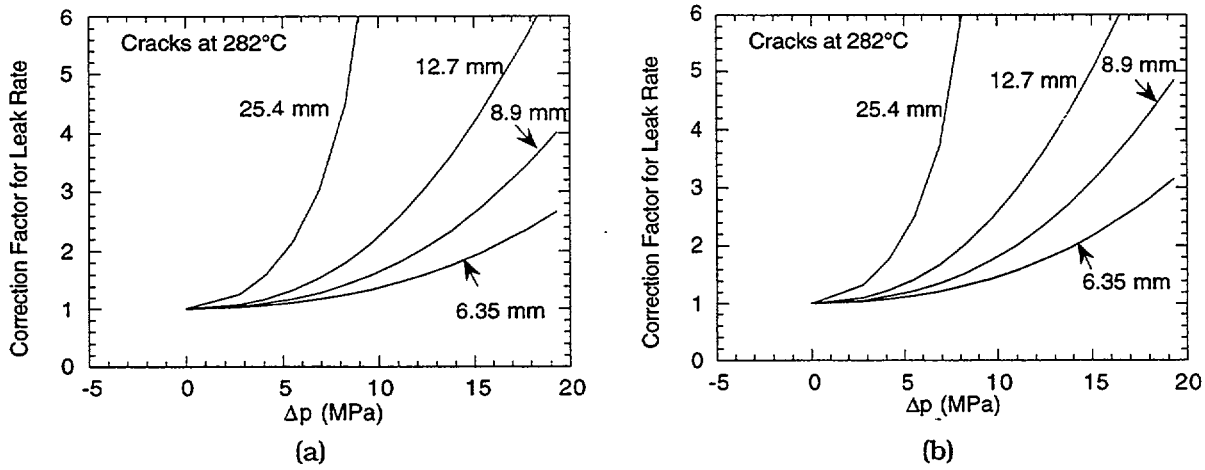

Fig. 24. Correction factors for obtaining leak rates in as-received Alloy 600 tubes with single throughwall axial cracks from heat-treated tube data at (a) 20°C and (b) 282°C.

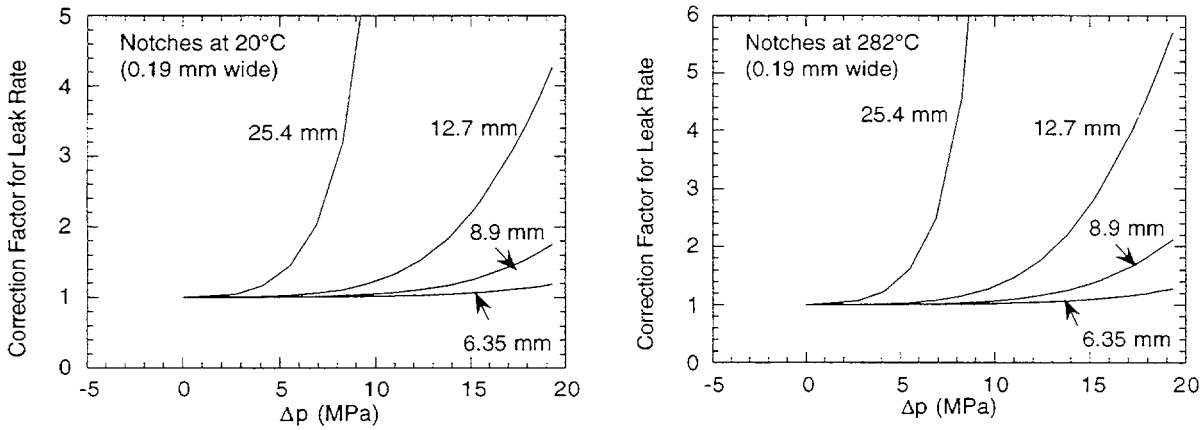

Fig. 25. Correction factors for obtaining leak rates in as-received Alloy 600 tubes with single throughwall axial EDM notches from heat-treated tube data at (a) 20°C and (b) 282°C.

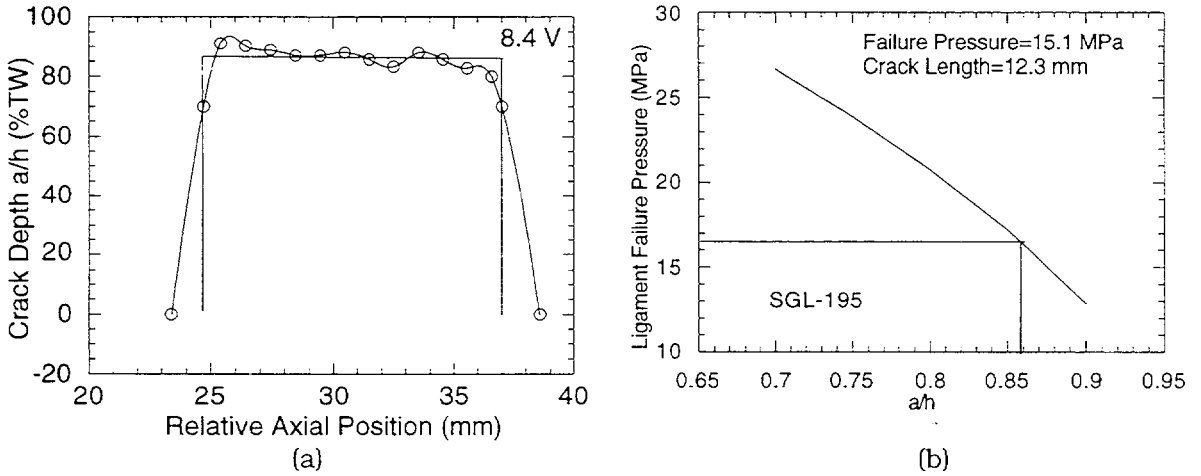

Fig. 26. (a) Estimated crack depth profile from Eddy Current +Point data for specimen SGL-195 tested at 20°C and (b) calculated ligament failure pressure of 16.5 MPa for equivalent rectangular crack length of 12.3 mm.

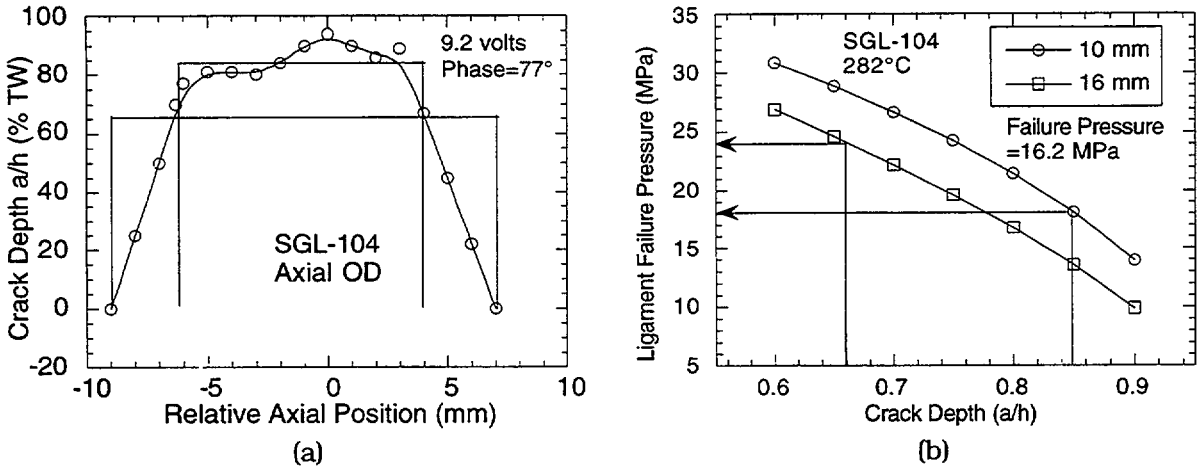

Fig. 27. (a) Estimated crack depth profile from Eddy Current +Point data for specimen SGL-104 tested at 282°C and (b) calculated ligament failure pressure of 18 MPa at an equivalent rectangular crack lengths of 10 mm.

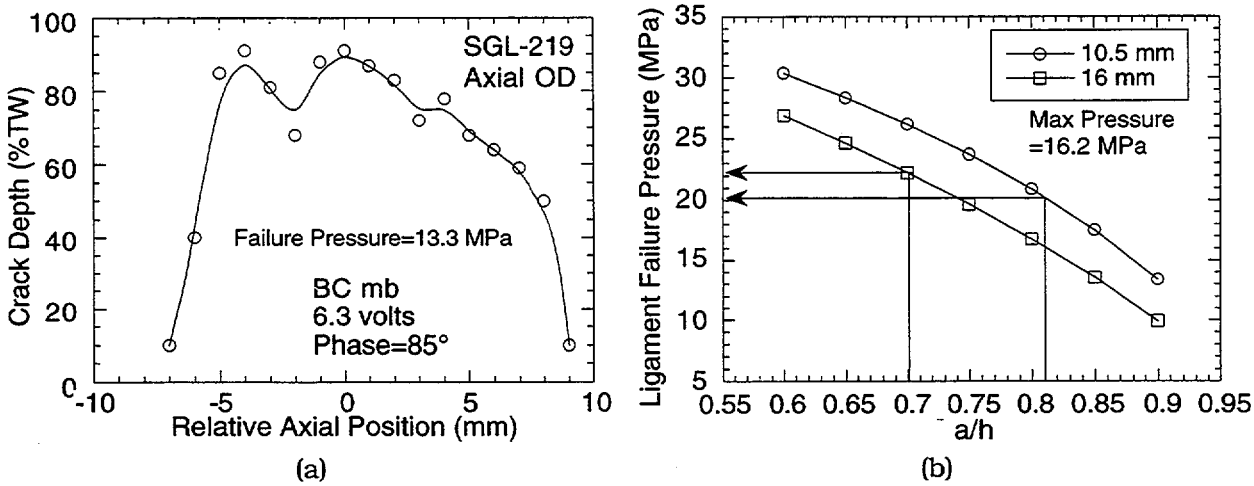

Fig. 28. (a) Estimated crack depth profile from Eddy Current +Point data for specimen SGL-219 tested at 282°C and (b) calculated ligament failure pressure of 20 MPa at equivalent rectangular crack lengths of 10.5 mm.

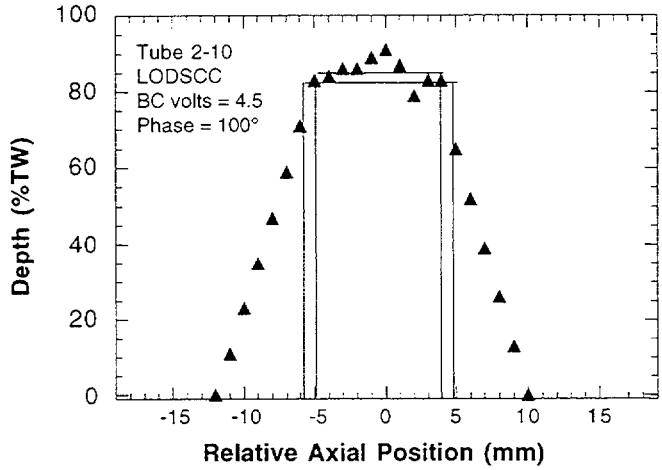

Fig. 29. Estimated crack depth profile from Eddy Current +Point data for Westinghouse tube 2-10.

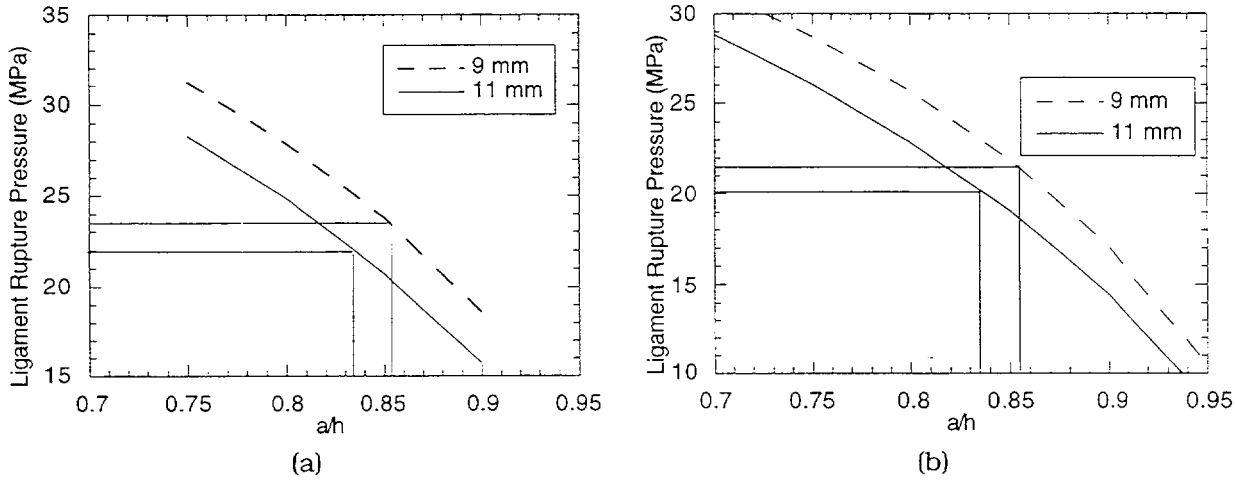

Fig. 30. Calculated ligament rupture pressure for two equivalent rectangular cracks in Westinghouse tube 2-10 at (a) room temperature and (b) 282°C.

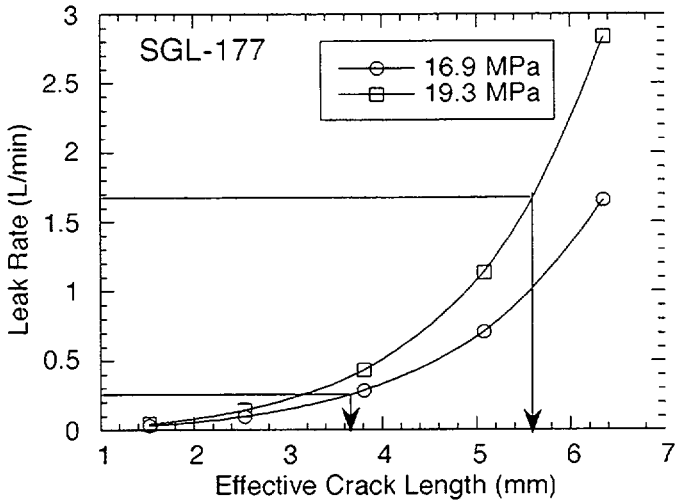

Fig. 31. Effective throughwall crack length estimated from leak rate data for test SGL-177.

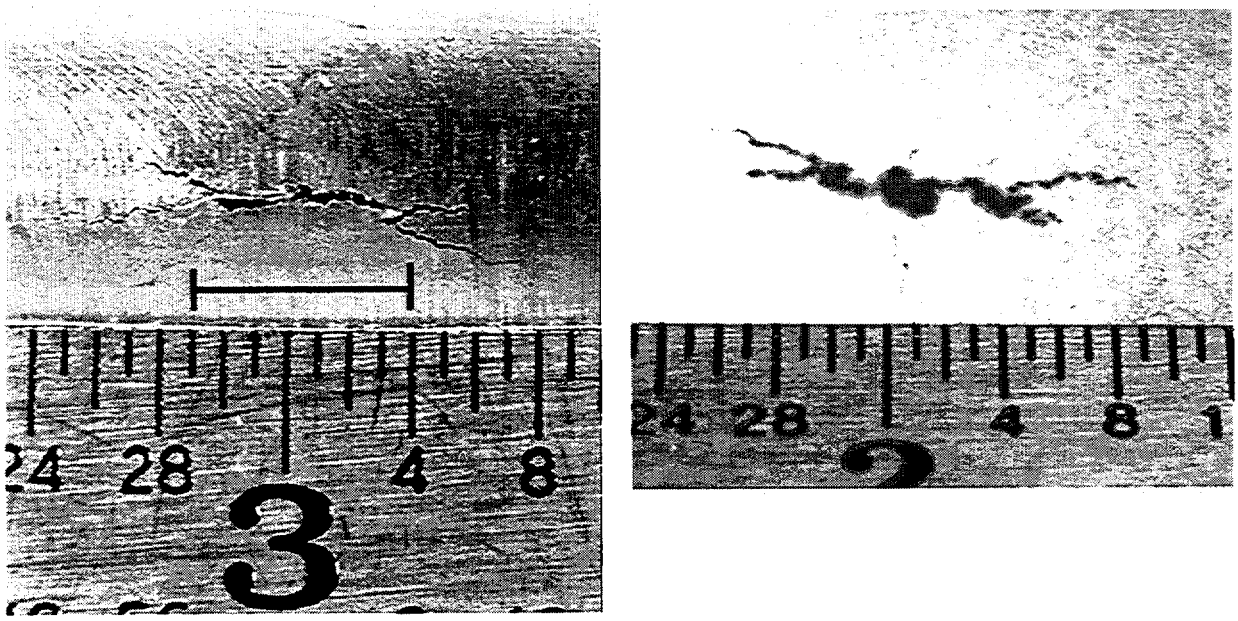

(a) (b)

Fig. 32. (a) Posttest and (b) pretest dye-penetrant-enhanced views of crack in test specimen SGL-177. Marker in (a) indicates effective throughwall crack length (5.6 mm) estimated (Fig. 31) from measured leak rate.

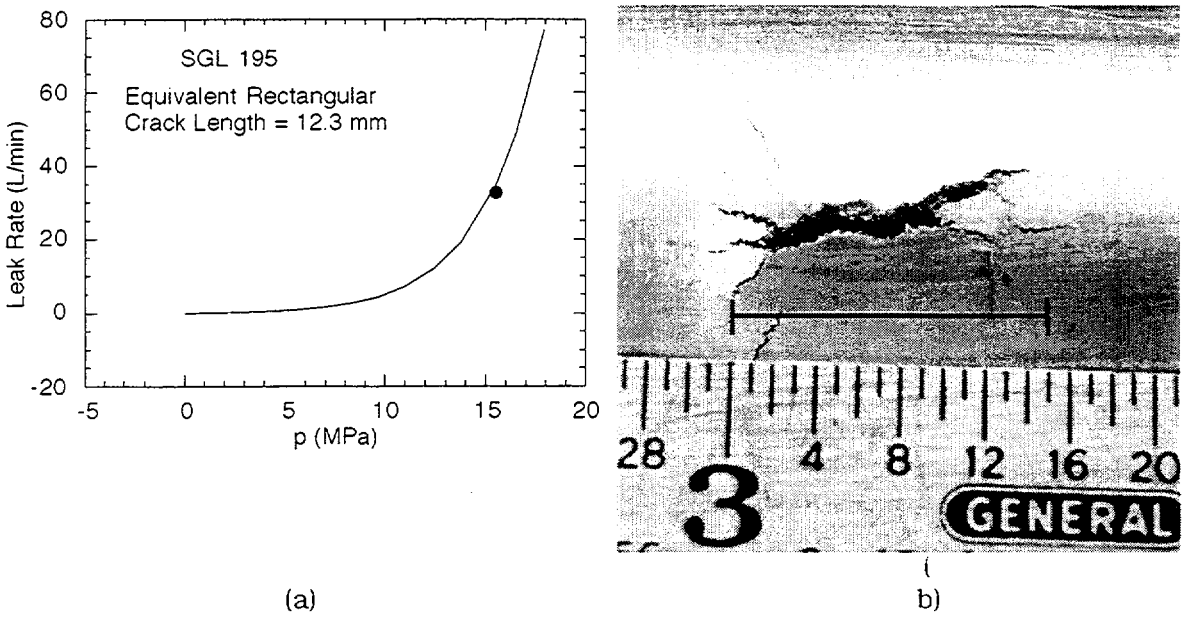

(a) b)

Fig. 33. (a) Predicted leak rate vs. pressure plot for test SGL-195; symbol represents measured leak rate at maximum test pressure after abrupt increase of leak rate. (b) Posttest view of OD crack of specimen SGL-195; marker indicates equivalent rectangular crack length (12.3 mm).

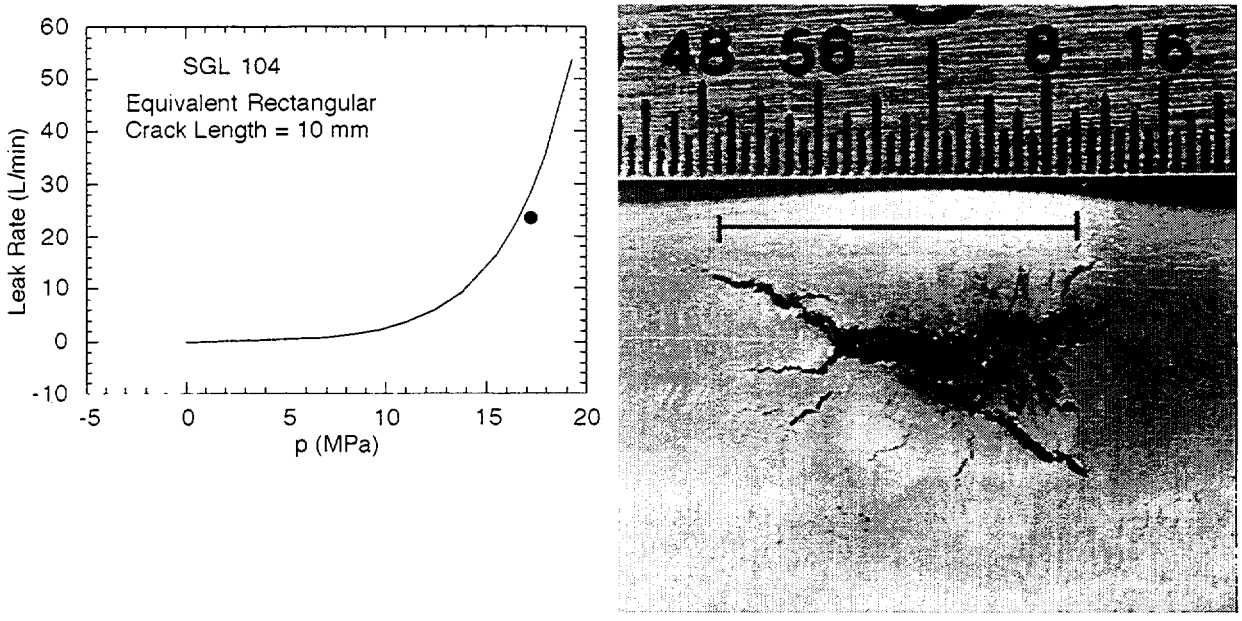

(a) (b)

Fig. 34. (a) Predicted leak rate vs. pressure plot for test SGL-104; symbol represents measured leak rate at maximum test pressure after abrupt increase of leak rate. (b) Posttest view of OD crack of specimen SGL-104; marker indicates equivalent rectangular crack length (10 mm).

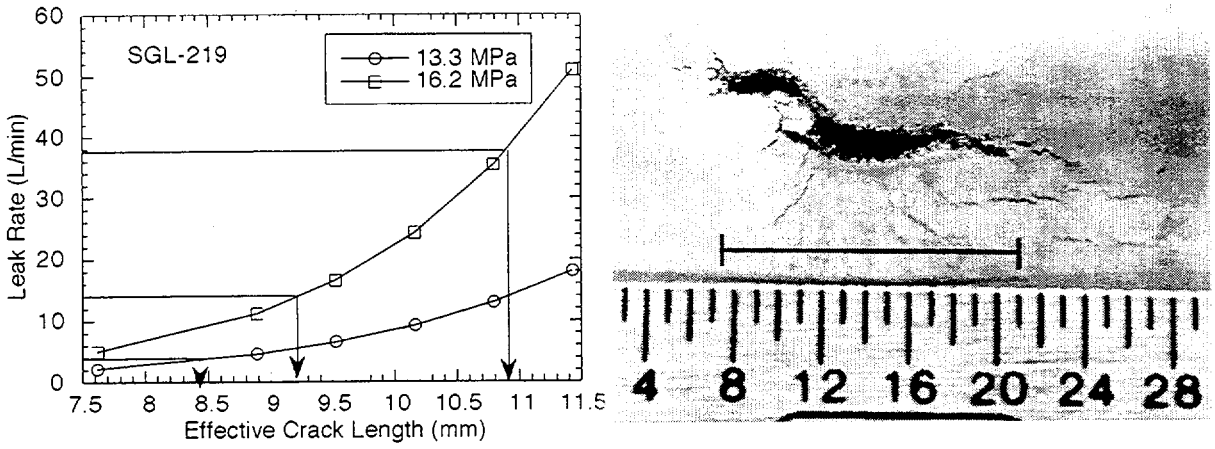

(a) (b)

Fig. 35. (a) Effective throughwall crack lengths estimated from leak rate data for test SGL- 219 and (b) posttest view of OD crack of specimen SGL219. Marker indicates final effective throughwall crack length (11 mm) calculated from measured leak rate.

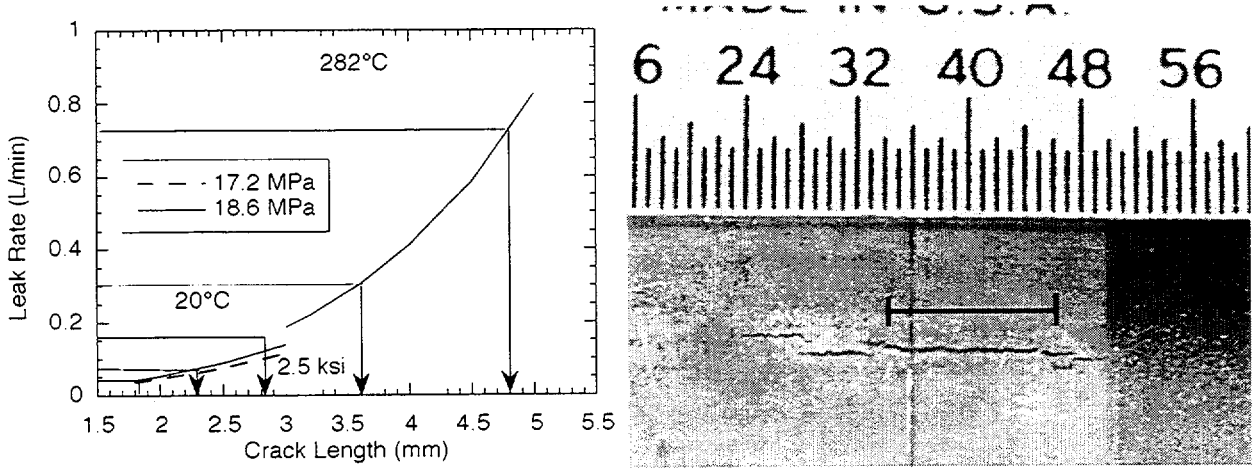

(a) (b)

Fig. 36. (a) Calculated leak rate in Westinghouse tube 2-10 vs. crack length at 17.2 and 18.6 MPa at room temperature and at 18.6 MPa at 282°C. (b) Posttest view of OD crack of Westinghouse specimen 2-10. Marker indicates effective throughwall crack length (4.8 mm) calculated from measured leak rate.

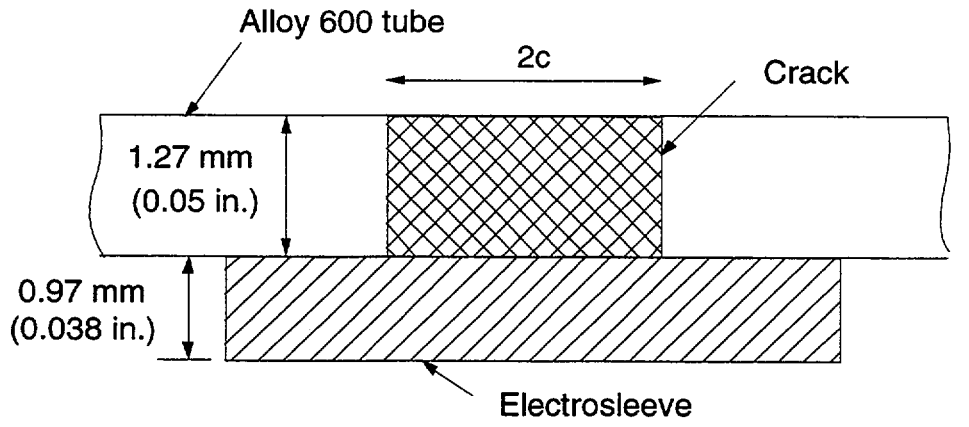

Fig. 37. Reference geometry for Electrosleeved steam generator tube with axial crack.

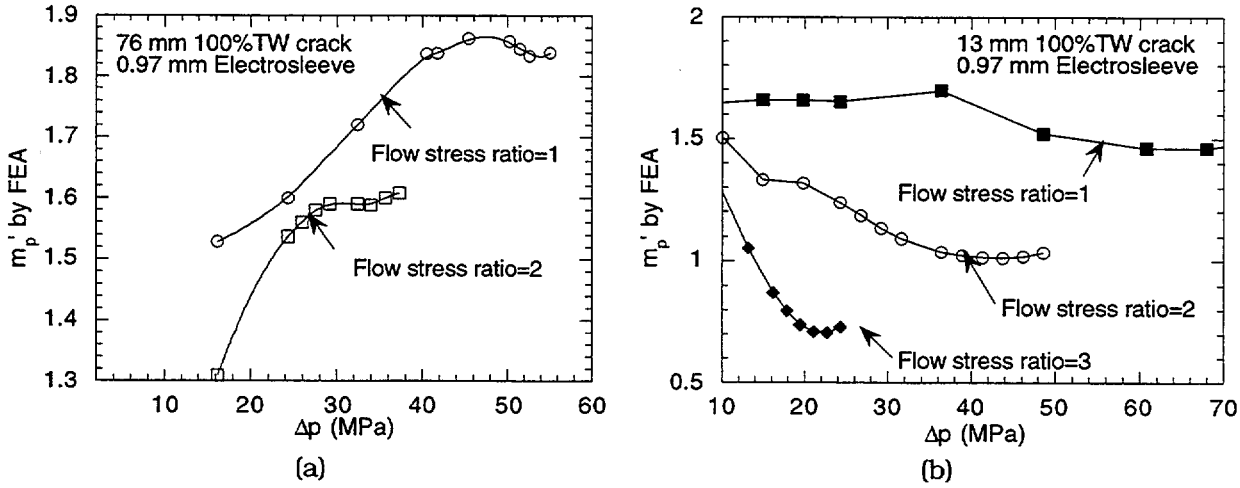

Fig. 38. Variation of m_p' factor with pressure for (a) 76-mm (3 in.)-long and (b) 13-mm (0.5 in.)-long cracks for various values of flow stress ratios between tube and Electrosleeve.

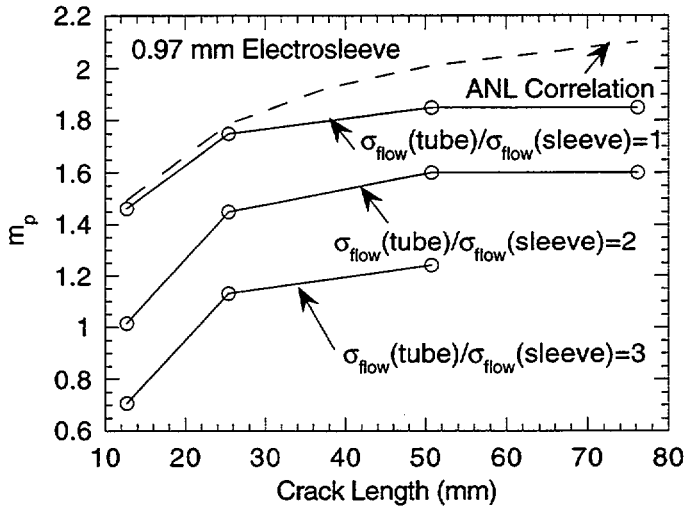

Fig. 39. Comparison of m_p values calculated by ANL correlation for single layer shell (dashed line) with those by FEA (solid lines with symbols) for ratios of flow stress of Alloy 600 and Electrosleeve of 1, 2, and 3. Tube wall thickness was assumed equal to 1.27 mm (0.050 in.).

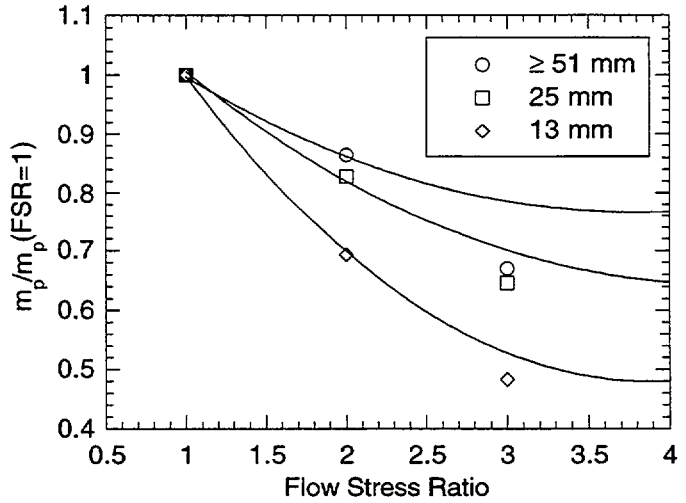

Fig. 40. Variation of m_p reduction factor with flow stress ratio (FSR) as calculated from FEA results for various crack lengths.

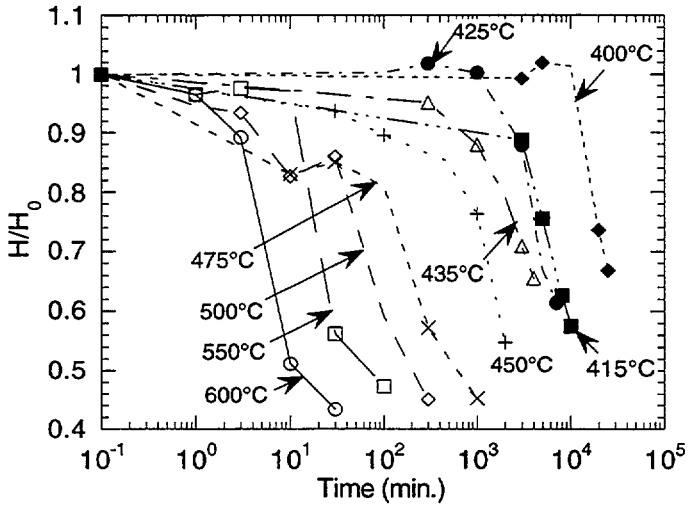

Fig. 41. Variations of normalized Vickers Hardness Number (VHN) of Electrosleeve material with time under isothermal aging at various temperatures.

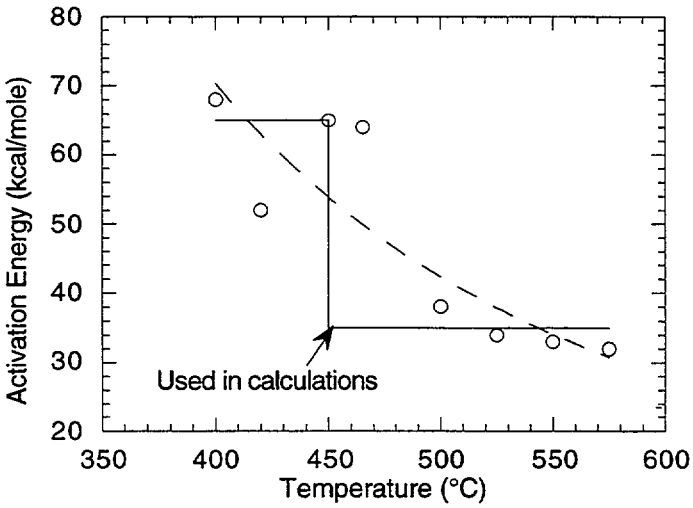

Fig. 42. Variation of activation energy for reciprocal of time to onset of rapid reduction of flow stress (or grain growth) with temperature.

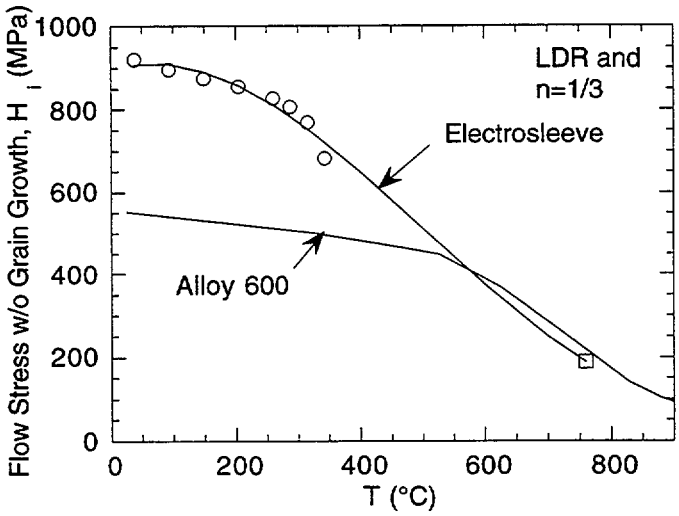

Fig. 43. Flow stress (without aging) vs. temperature plot for Electrosleeve material and Alloy 600. Electrosleeve data (square symbol) at 760°C were estimated from tensile data on single specimen preaged and tested at 760°C, using n = 0.33. This flow stress curve of Electrosleeve was subsequently modified on the basis of ANL tests.

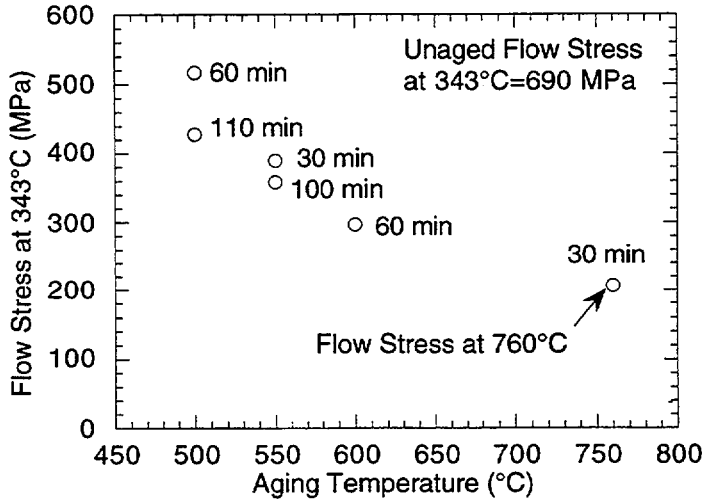

Fig. 44. Flow stress data on Electrosleeve material preaged for various times at high temperatures. All tensile tests were conducted at 343°C, except for test on specimen preaged at 760°C, which was conducted at 760°C.

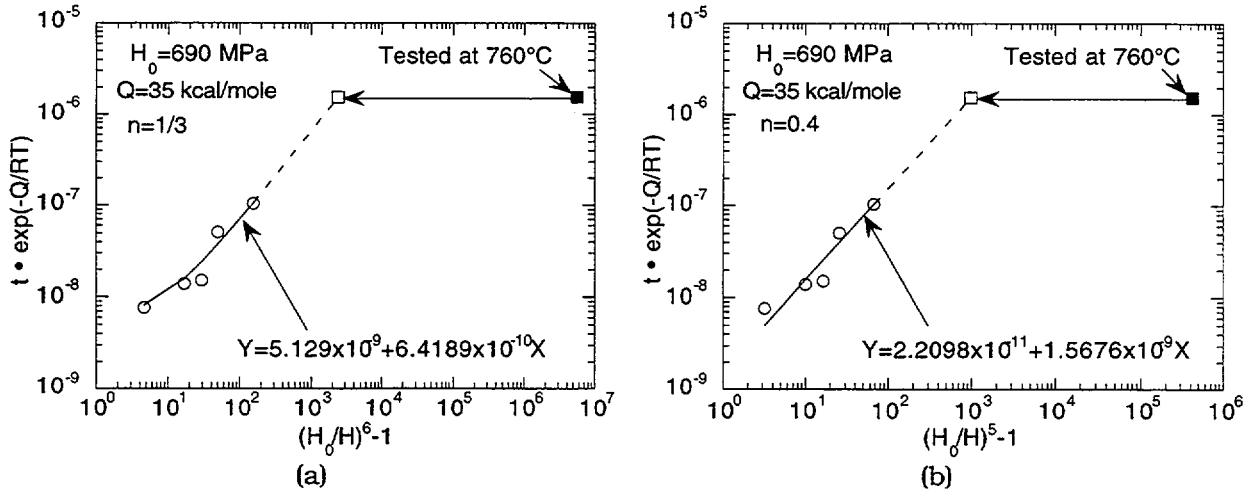

Fig. 45. Flow stress ("unaged") parameter vs. temperature plot for Electrosleeve material. Data (open square symbol) at 760°C were estimated from tensile data (filled square symbol) on specimen aged and tested at 760°C, using a Hall-Petch exponent (a) n = 0.33 and (b) n = 0.40.

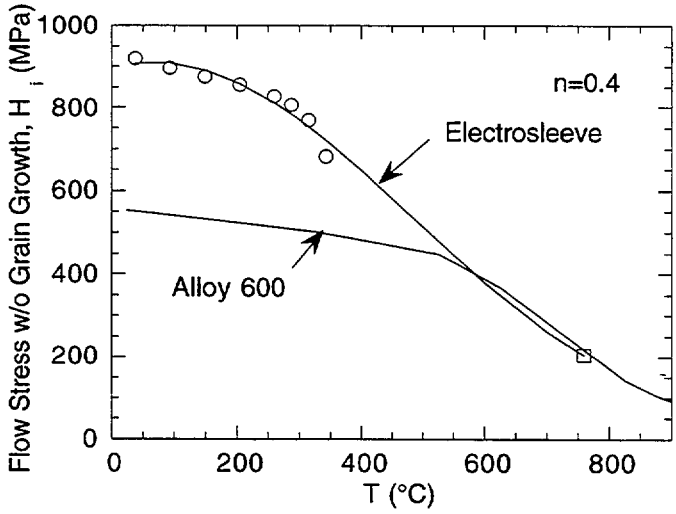

Fig. 46. Flow stress ("unaged") vs. temperature plot for Electrosleeve material and Alloy 600. Electrosleeve data (square symbol) at 760°C were estimated from tensile data on single specimen preaged and tested at 760°C, using n = 0.4.

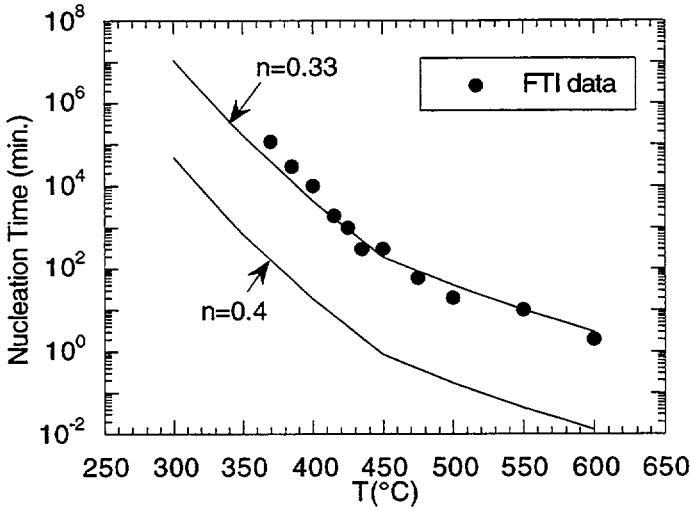

Fig. 47. Variation of calculated "nucleation" times to onset of rapid loss of flow stress (or grain growth) under isothermal aging with aging temperature for Hall-Petch exponents of n = 0.33 and n = 0.40, using a temperature-dependent activation energy given by step function in Fig. 42. Also shown are nucleation times for rapid loss of flow stress derived from FTI data shown in Fig. 41.

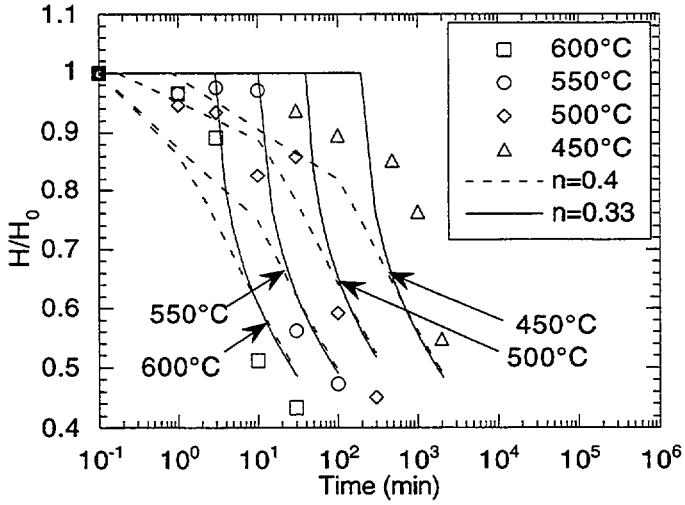

Fig. 48. Comparison of calculated variations of normalized Vickers Hardness Number (VHN) of Electrosleeve, using Hall-Petch model with n = 0.33 and n = 0.4. with experimentally measured variations under isothermal aging at various temperatures.

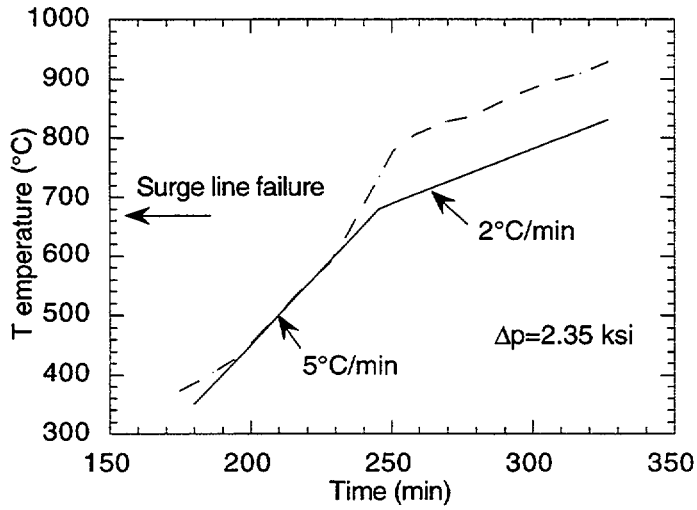

Fig. 49. Time temperature history for tests reported in Ref. 5 (dashed line represents a simplified version) and simplified scoping ramp (solid line). Internal pressure = 16.2 MPa (2.35 ksi).

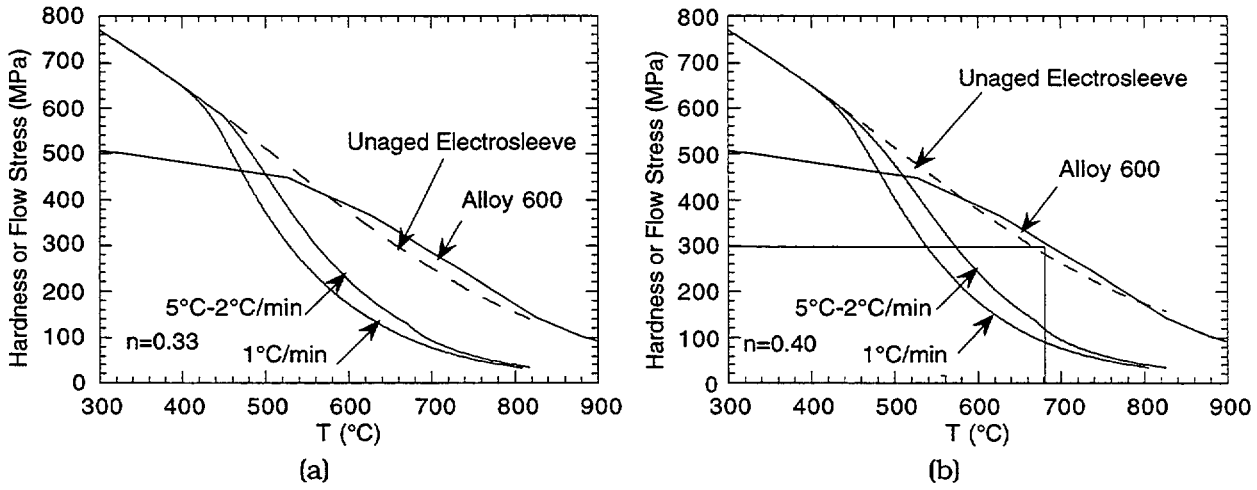

Fig. 50. Calculated variations of flow stress of Electrosleeve material with temperature, using Hall-Petch exponent (a) n = 0.33 and (b) n = 0.40, for scoping ramp (Fig. 49) and constant ramp rate of 1°C/min.

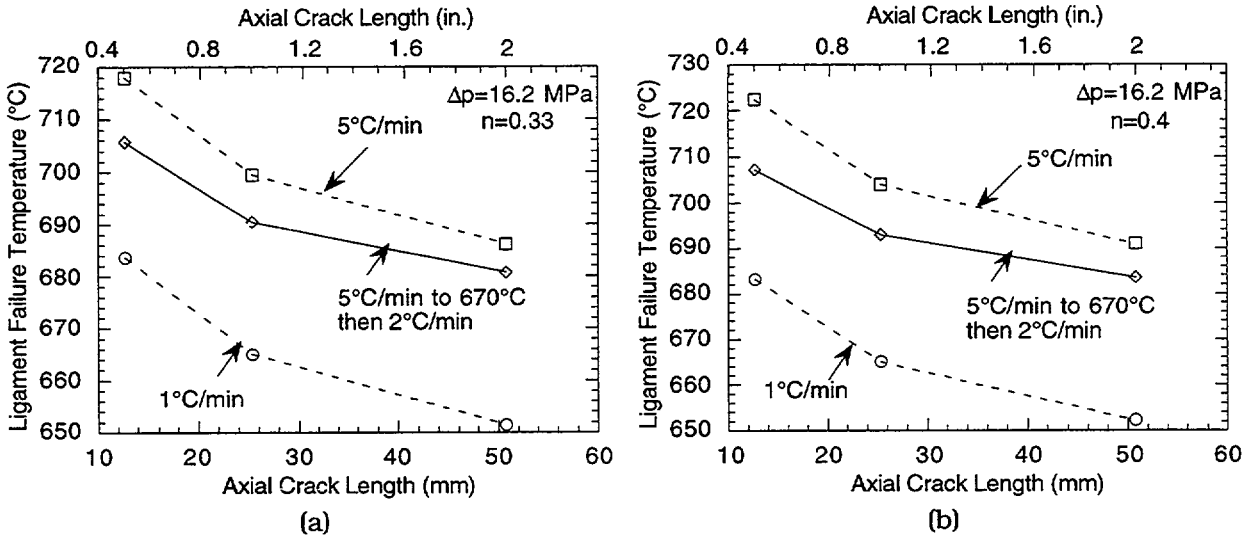

Fig. 51. Predicted ligament failure temperatures by Hall-Petch model for Electrosleeved tubes with throughwall axial cracks under scoping ramp (Fig. 49) and constant-temperature ramp rates of 1 and 5°C/min and constant internal pressure of 16.2 MPa (2.35 ksi), using (a) n = 0.33 and (b) n = 0.4.

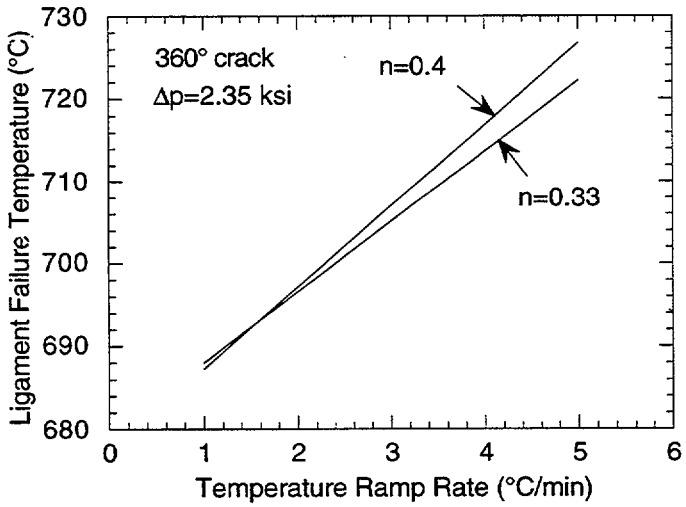

Fig. 52 Predicted ligament failure temperatures by Hall-Petch model for Electrosleeved tubes with throughwall 360° circumferential crack under various temperature ramps with constant internal pressure of 16.2 MPa (2.35 ksi).

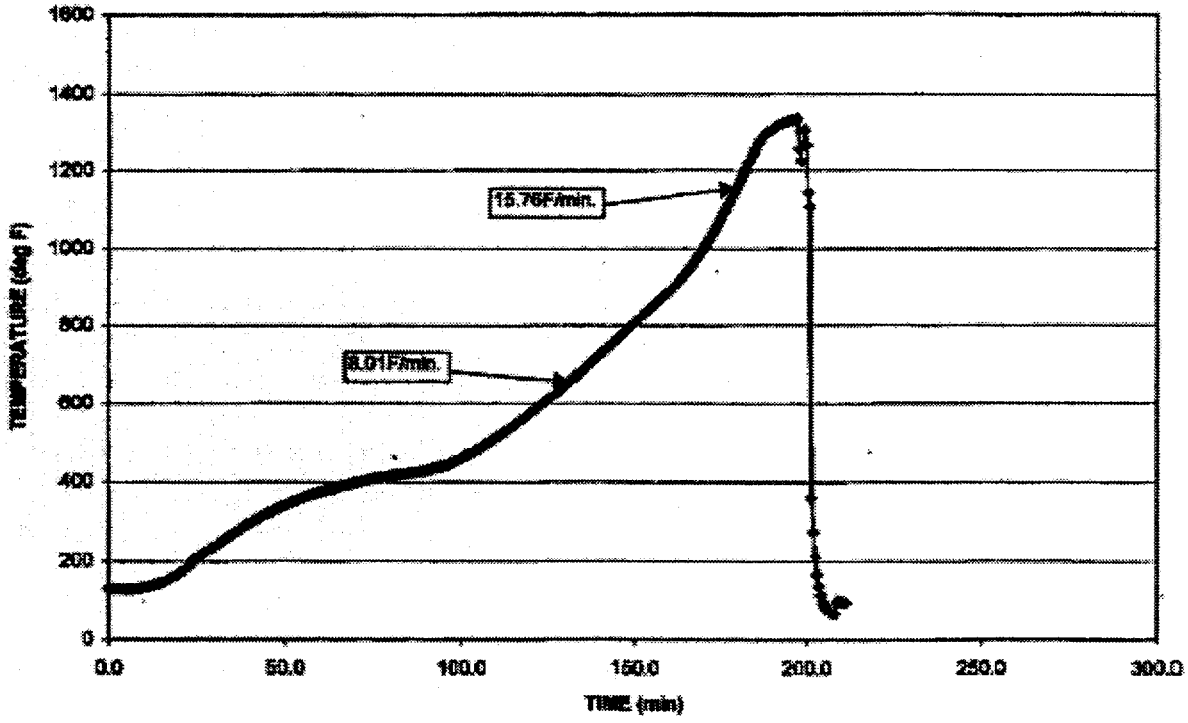

(a)

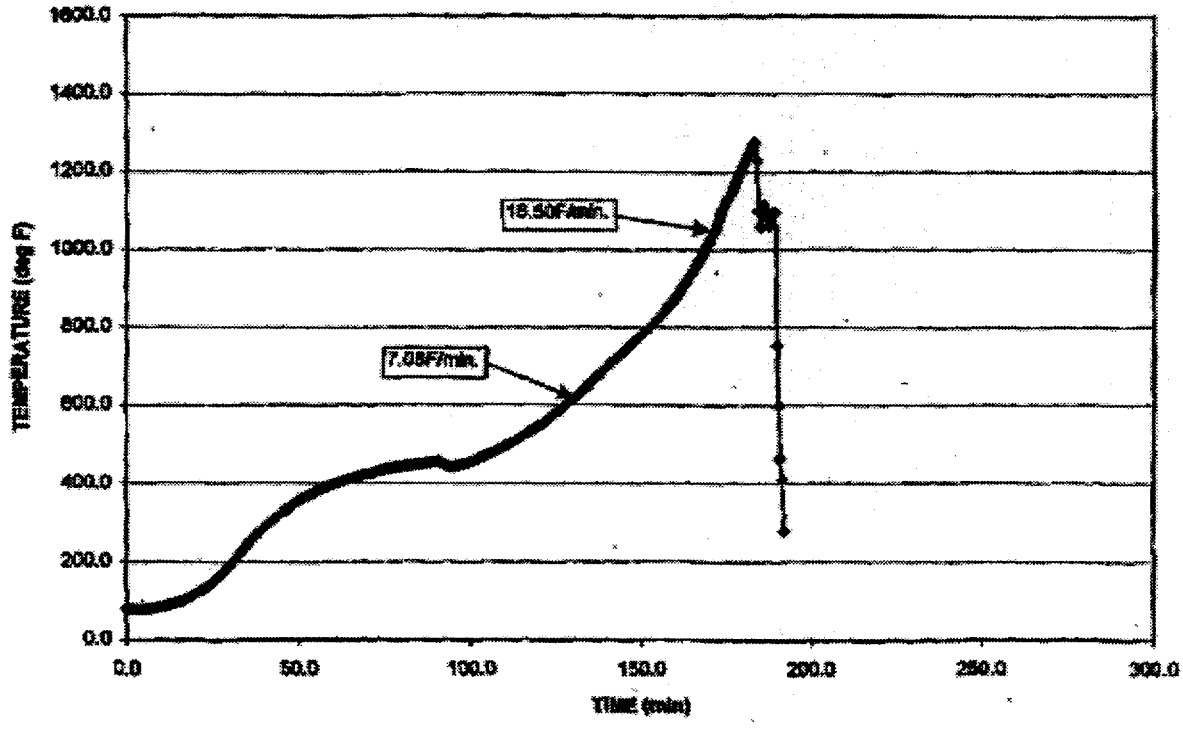

(b)

Fig. 53. Temperature ramps used in FTI tests on Electrosleeved specimens (a) BTF-23, (b) BTF-25, and (c) R.5.2

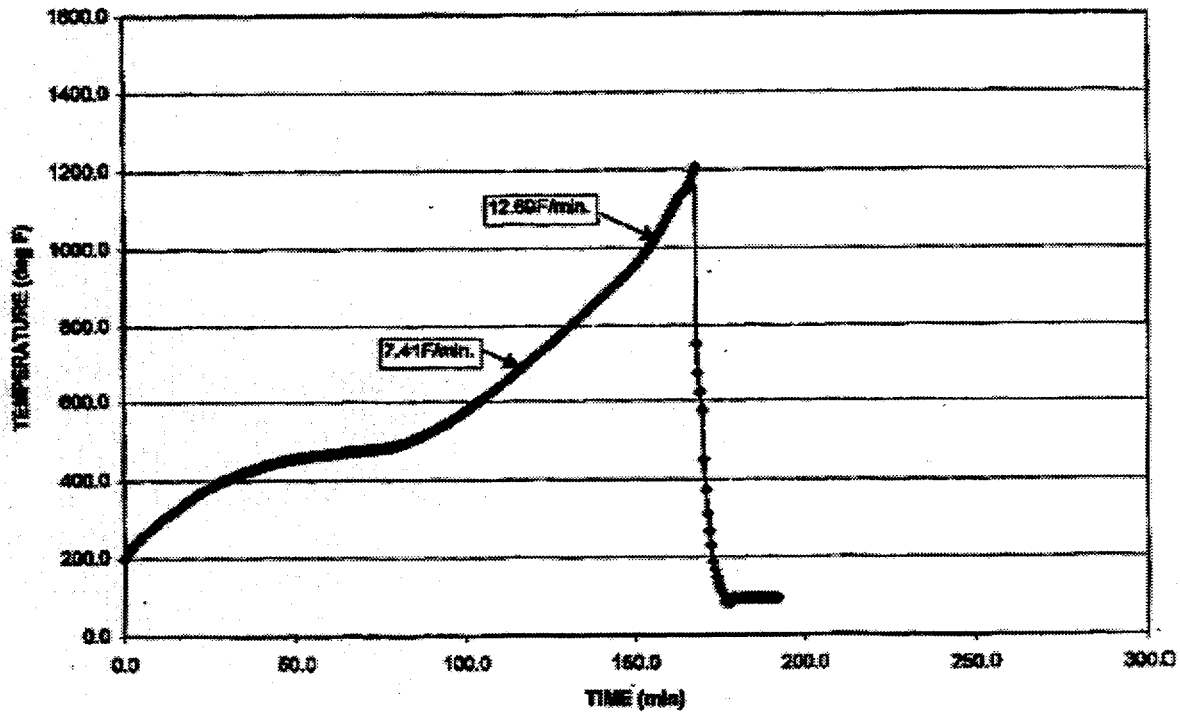

(c)

Fig. 53 (Cont'd)

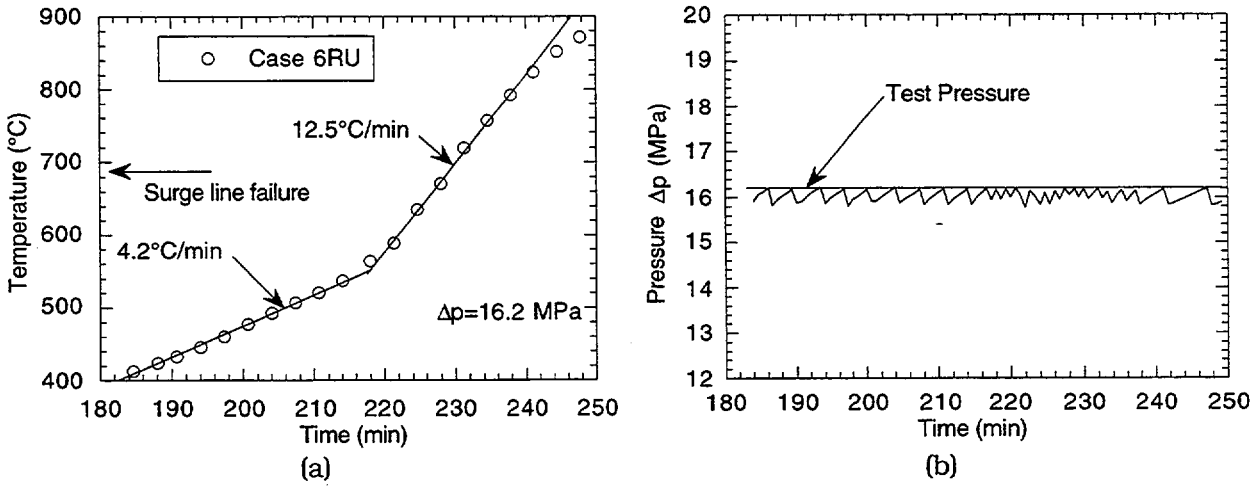

Fig. 54. Calculated variation and ANL test simulation of (a) temperature and (b) pressure differential during SBO (Case 6RU) severe accident transient.

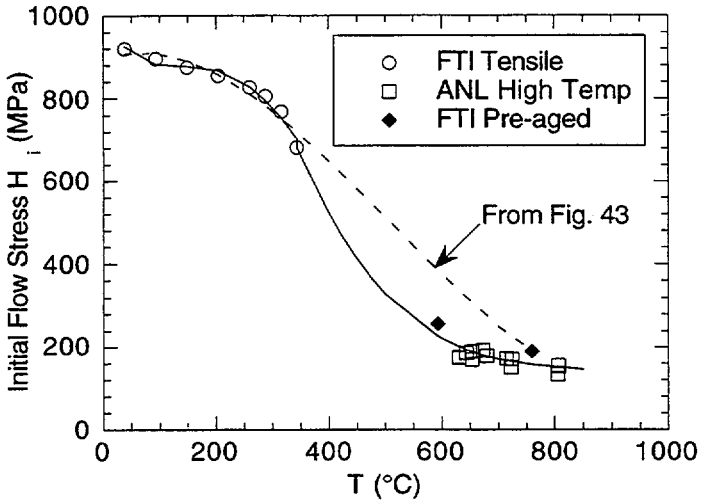

Fig. 55. Original unaged flow stress curve (dashed line) of Electrosleeve estimated from FTI tensile data before ANL tests were conducted and revised unaged flow stress curve (solid line) of Electrosleeve calculated using the ANL tests.

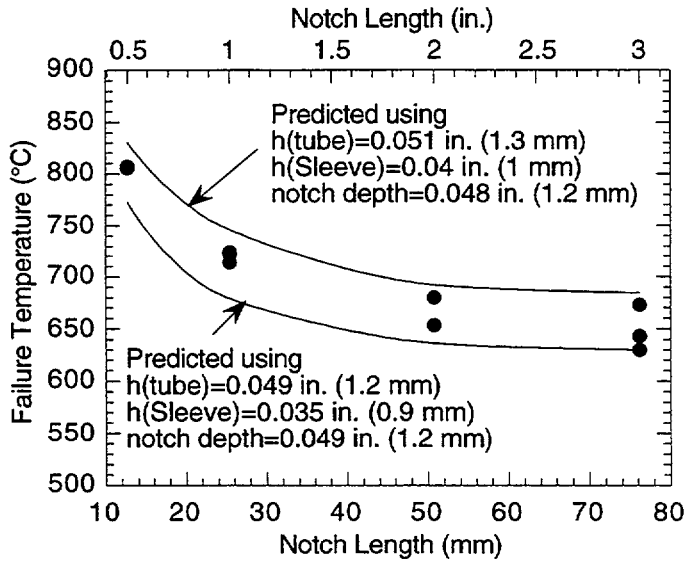

Fig. 56. Variation of ANL test failure temperatures (symbols) and predicted upper and lower bounds to the failure temperatures with notch length.

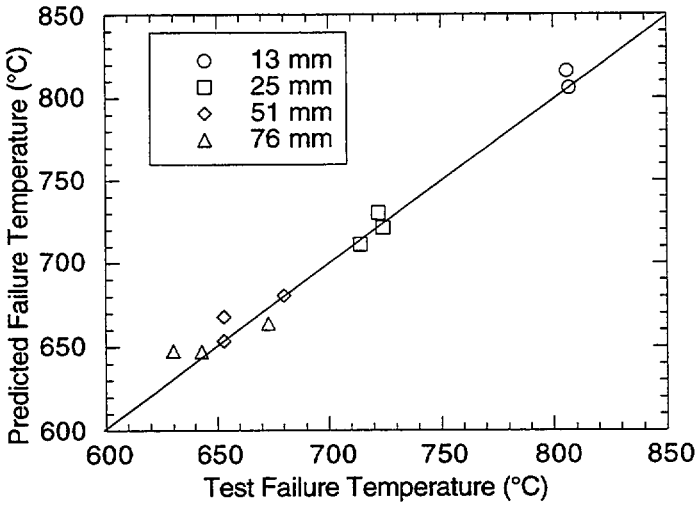

Fig. 57. Predicted vs. observed failure temperatures of ANL tests.

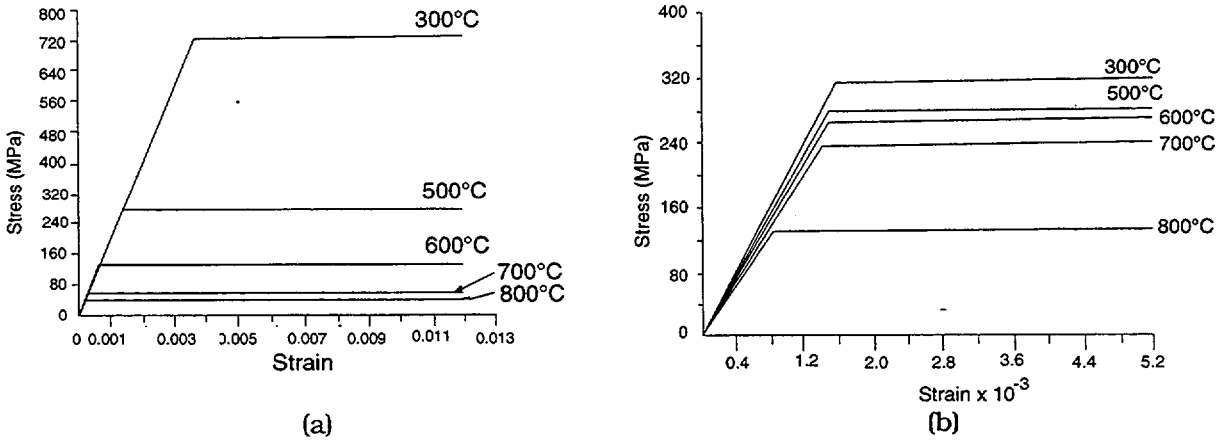

Fig. 58. Stress-strain curves used for (a) Electrosleeve (Case 6RU ramp) and (b) Alloy 600.

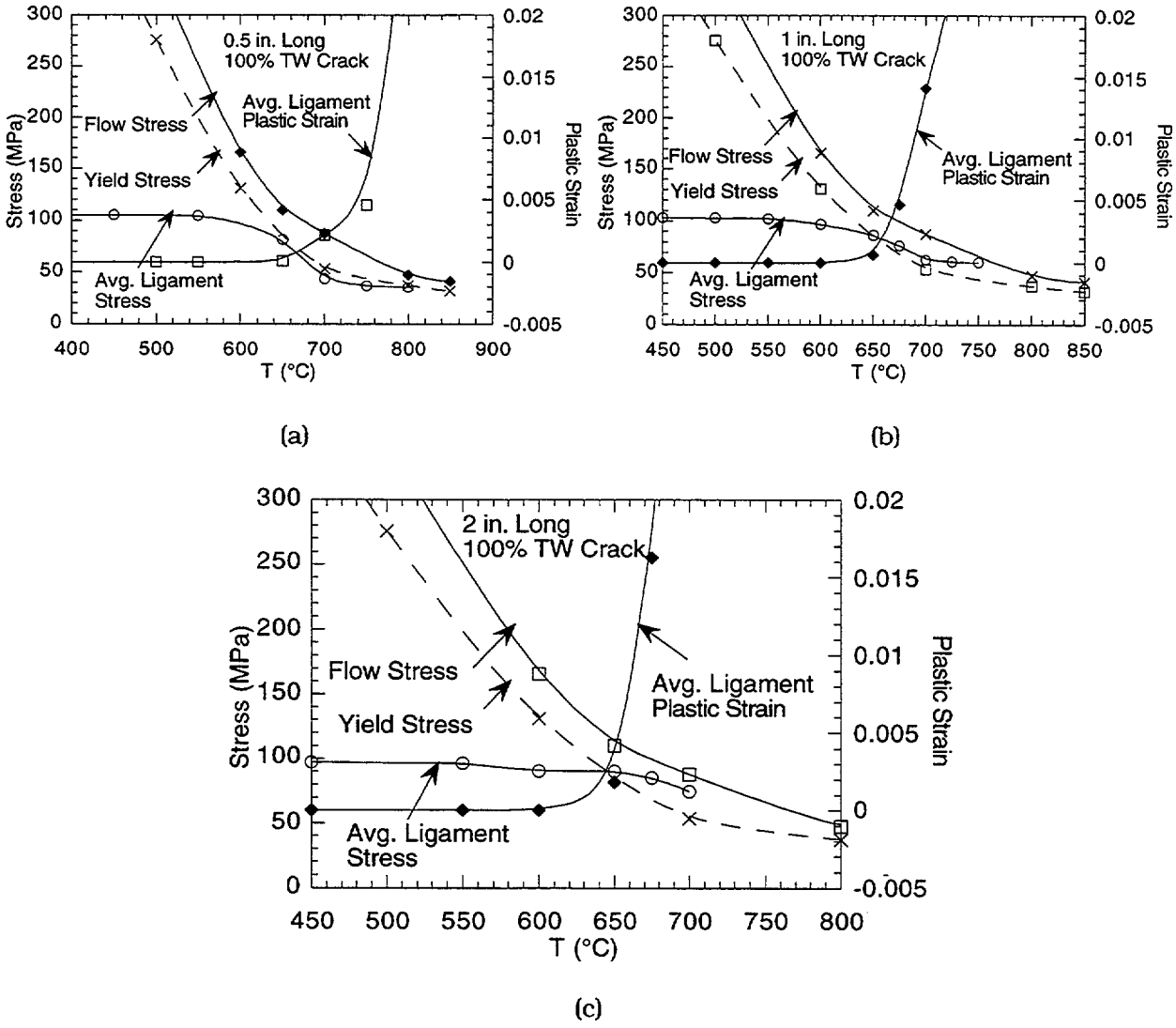

Fig. 59. Calculated variations of average ligament stress, average ligament plastic strain, yield stress and flow stress of Electrosleeve with temperature under Case 6RU loading on tube with (a) 13-mm (0.5 in.), (b) 25-mm (1 in.), and (c) 51 mm (2 in.)-long 100% throughwall cracks.

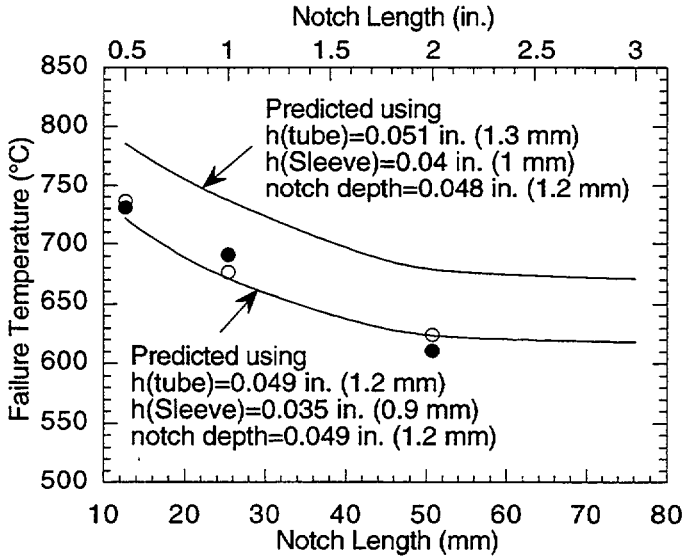

Fig. 60. Predicted (open symbols) and observed (filled symbols) failure temperatures vs. notch length of FTI tests; the predicted points are based on actual geometry and actual temperature ramp for each specimen.

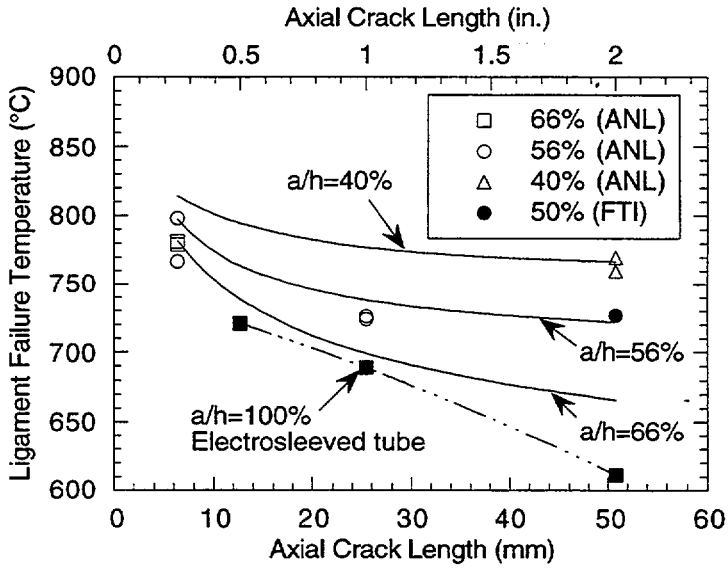

Fig. 61. Comparison of experimental ligament failure temperatures (open symbols from Ref. 4) with predicted values (solid lines using flow stress model) for unsleeved Alloy 600 tube with part-throughwall axial notches under EPRI ramp. Also shown are FTI data (filled circle) for unsleeved tube with 51 mm (2 in.)/50% TW notch and Electrosleeved tubes (filled squares) with throughwall cracks in parent tubes.

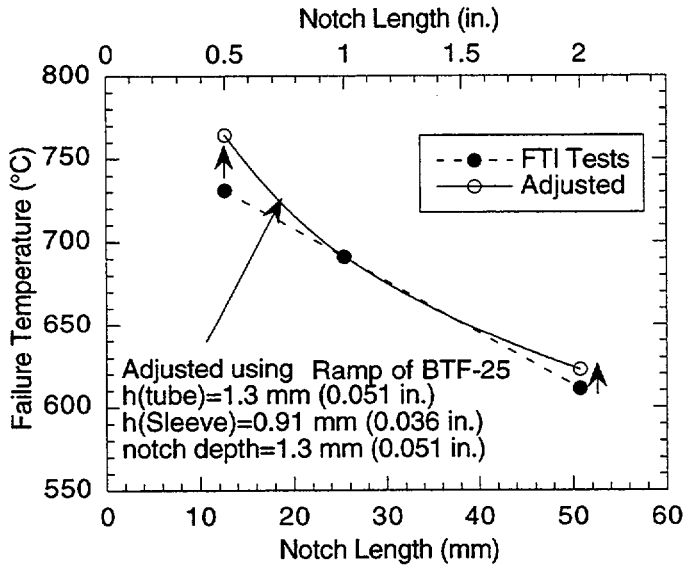

Fig. 62. Comparison of FTI test failure temperatures of Electrosleeved tubes with those adjusted by using flow stress model so that all specimens have identical geometry, except for notch length, and are subjected to same temperature ramp as BTF-25 (Fig. 53b).

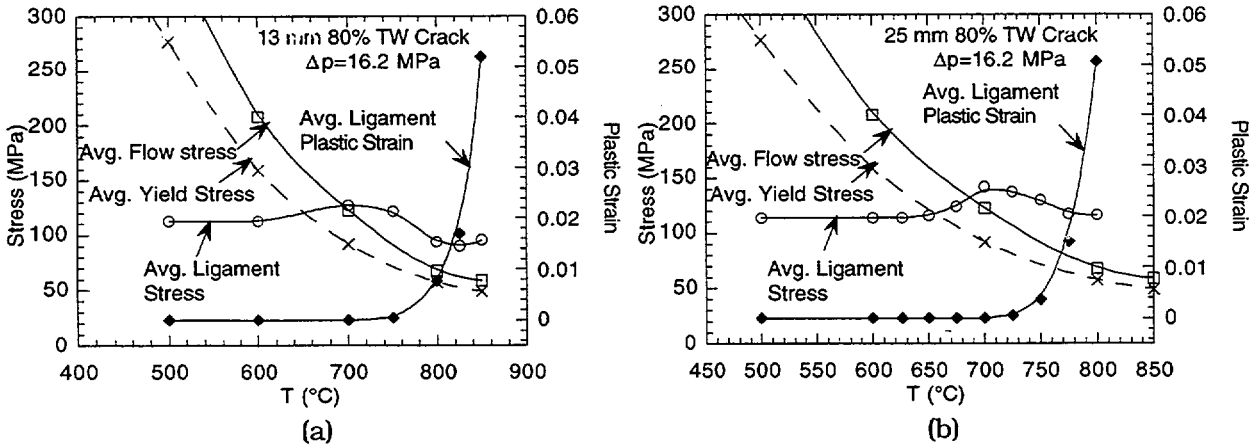

Fig. 63. Calculated variations of ligament-averaged stress, plastic strain, yield stress, and flow stress with temperature under Case 6RU loading of tube with a (a) 13 mm (0.5 in.), (b) 25-mm (1 in.), and (c) 51-mm (2 in.)-long 80% part-throughwall cracks.

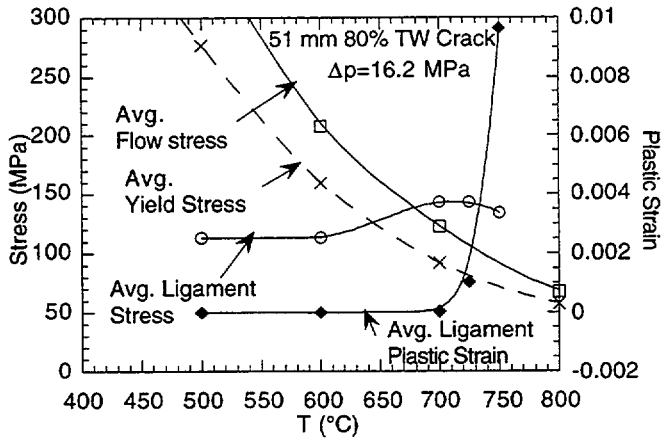

(c)

Fig. 63 (Cont'd)

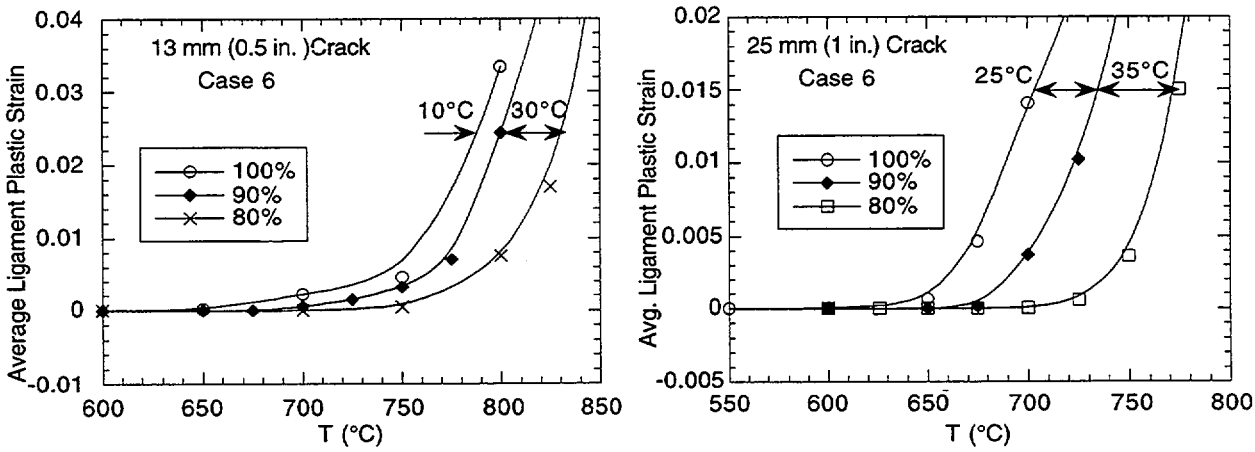

(a) (b)

Fig. 64. Calculated variations of ligament-averaged plastic strain with temperature under Case 6RU loading of tube with a (a) 13-mm (0.5 in.), (b) 25-mm (1 in.), and (c) 51-mm (2 in.)-long, 80, 90, and 100% deep part-throughwall cracks.

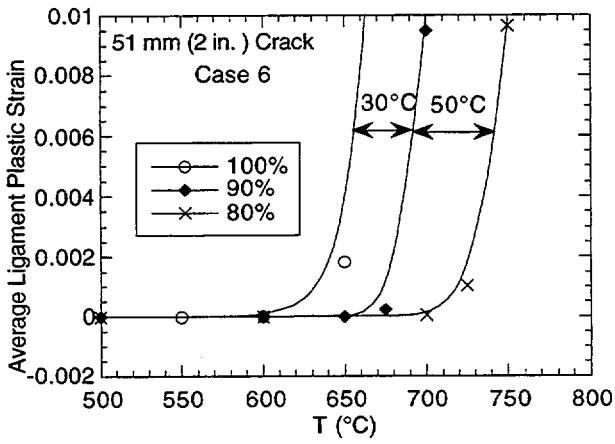

(c)

Fig. 64 (Cont'd)

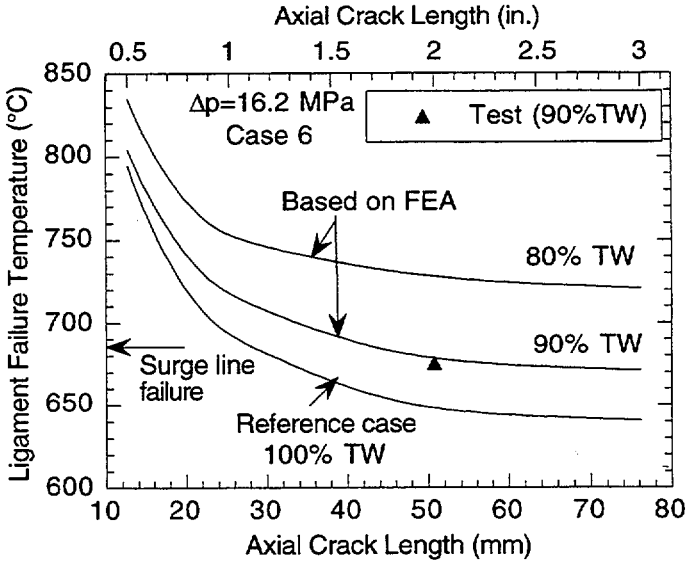

Fig. 65. Predicted ligament failure temperatures for 80, 90, and 100% throughwall cracks due to Case 6RU loading; symbol represents failure temperature of test (BTF-16) conducted at ANL on specimen with 90% part-throughwall, 51-mm (2 in.)-long EDM notch.

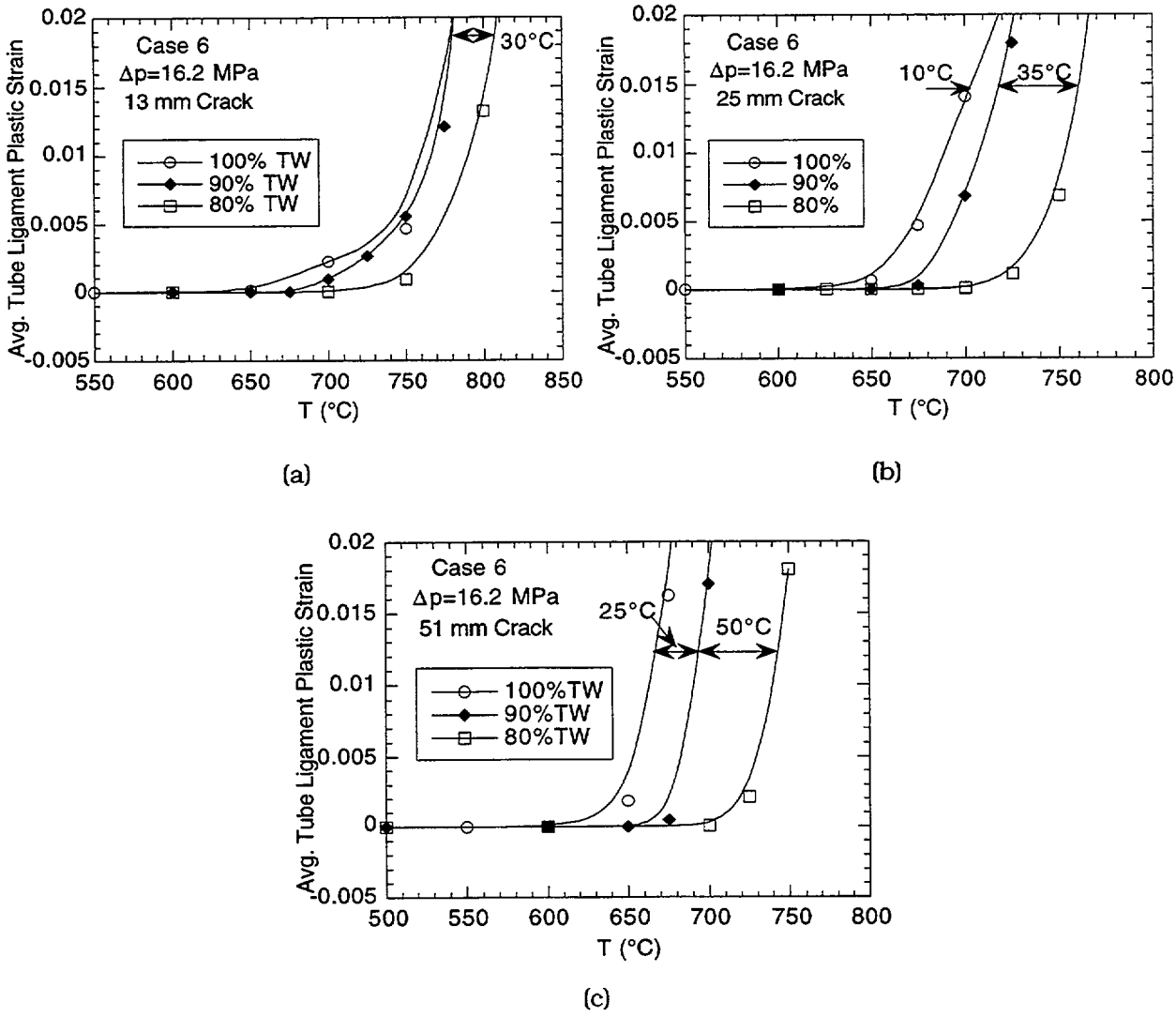

Fig. 66. Calculated variations of average plastic strain in Alloy 600 tube ligament with temperature under Case 6RU loading of tube with a (a) 13-mm (0.5 in.), (b) 25-mm (1 in.), and (c) 51-mm (2 in.)-long, 80 and 90% deep part-throughwall cracks. Also shown are average ligament plastic strains for 100% throughwall cracks.

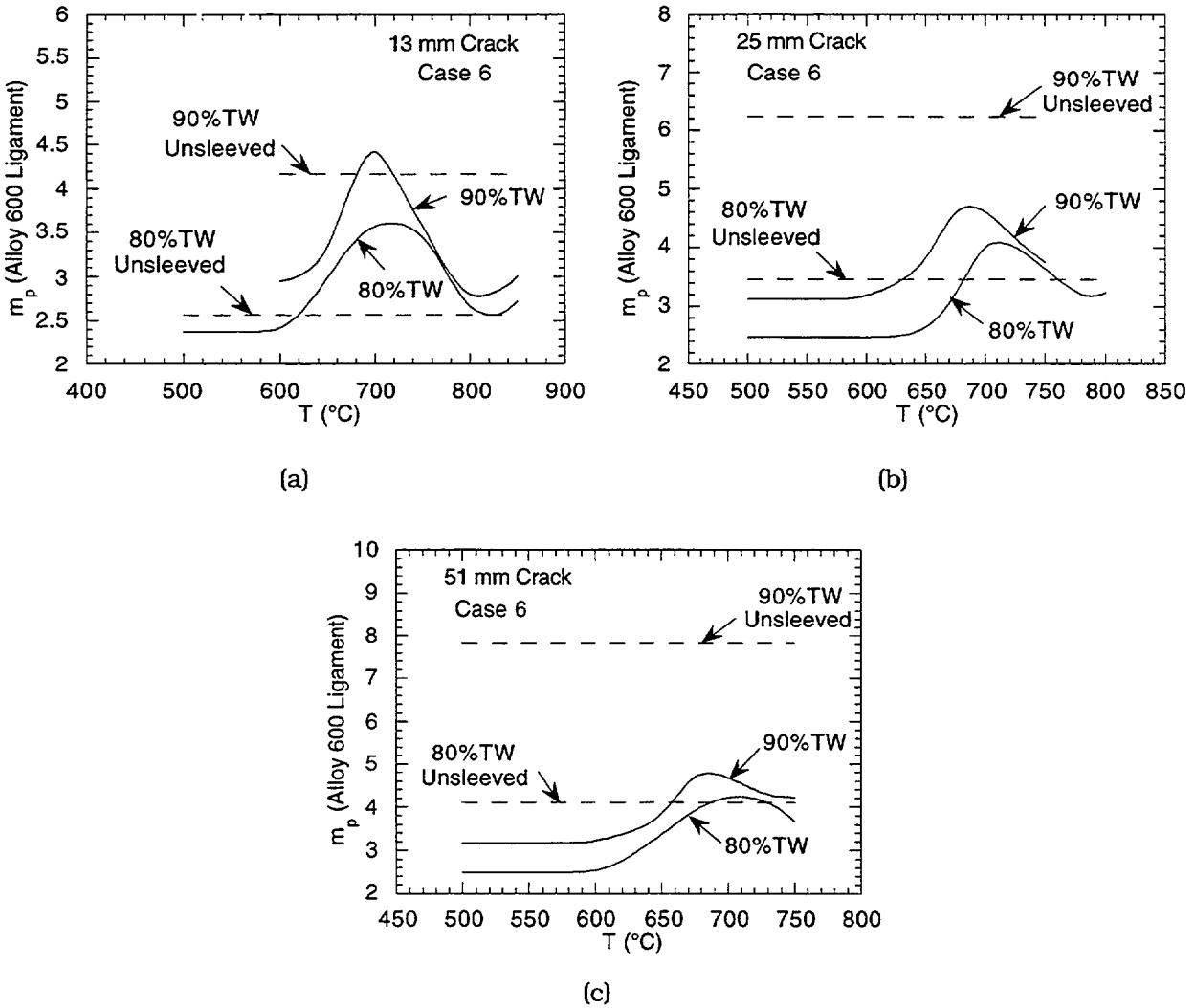

Fig. 67. Calculated variation of m_p for Alloy 600 tube ligament with temperature under Case 6RU loading of tube with (a) 13-mm (0.5 in.), (b) 25-mm (1 in.), and (c) 51-mm (2 in.)-long 80 and 90% deep part-throughwall cracks. Also shown are m_p (ANL) values for unsleeved tubes with 80 and 90% deep part-throughwall cracks.

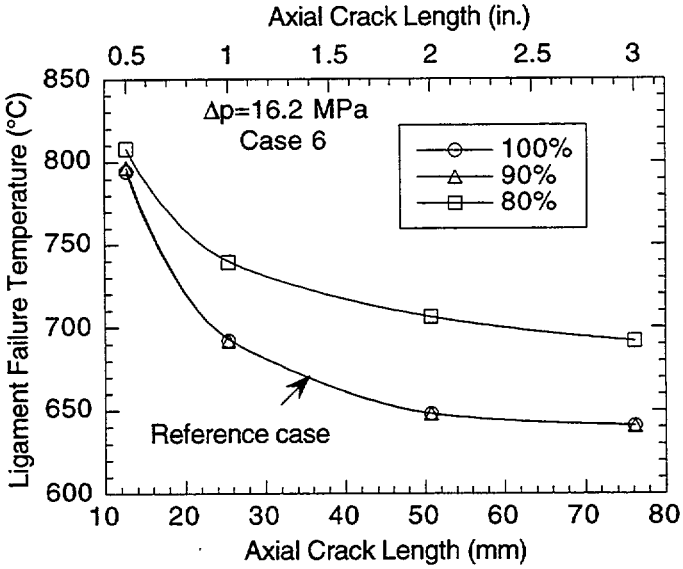

Fig. 68. Predicted ligament failure temperatures by simplified model for 80, 90, and 100% throughwall cracks due to Case 6RU loading.

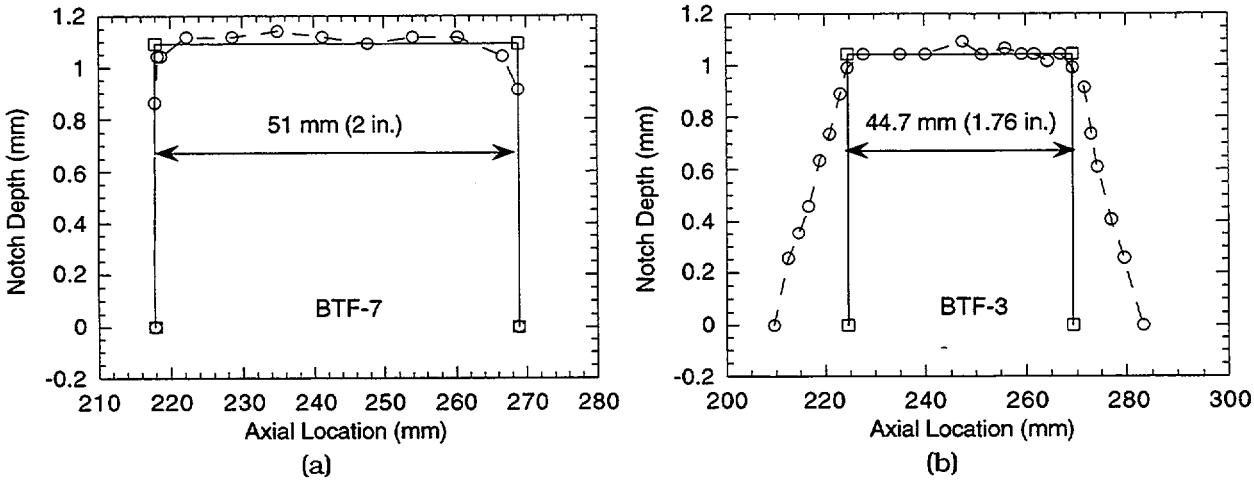

Fig. 69. Part-throughwall crack depth profiles reported by FTI for specimen (a) BTF-7 and (b) BTF-3. Also shown are equivalent crack lengths and depths.

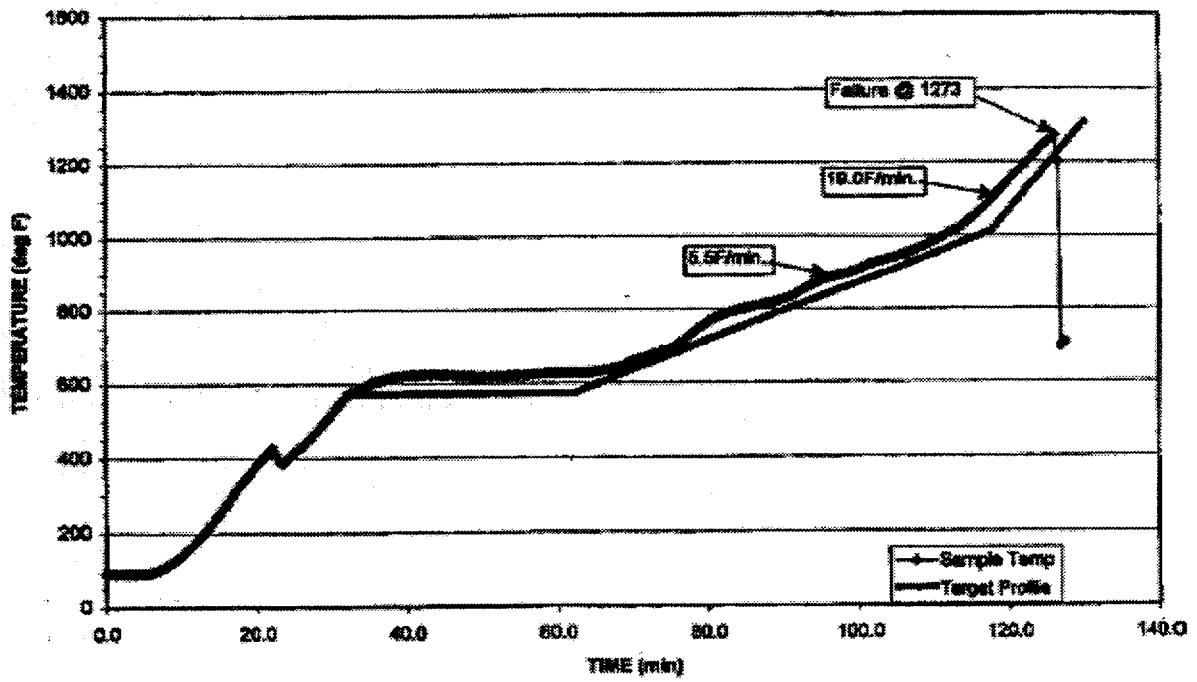

(a)

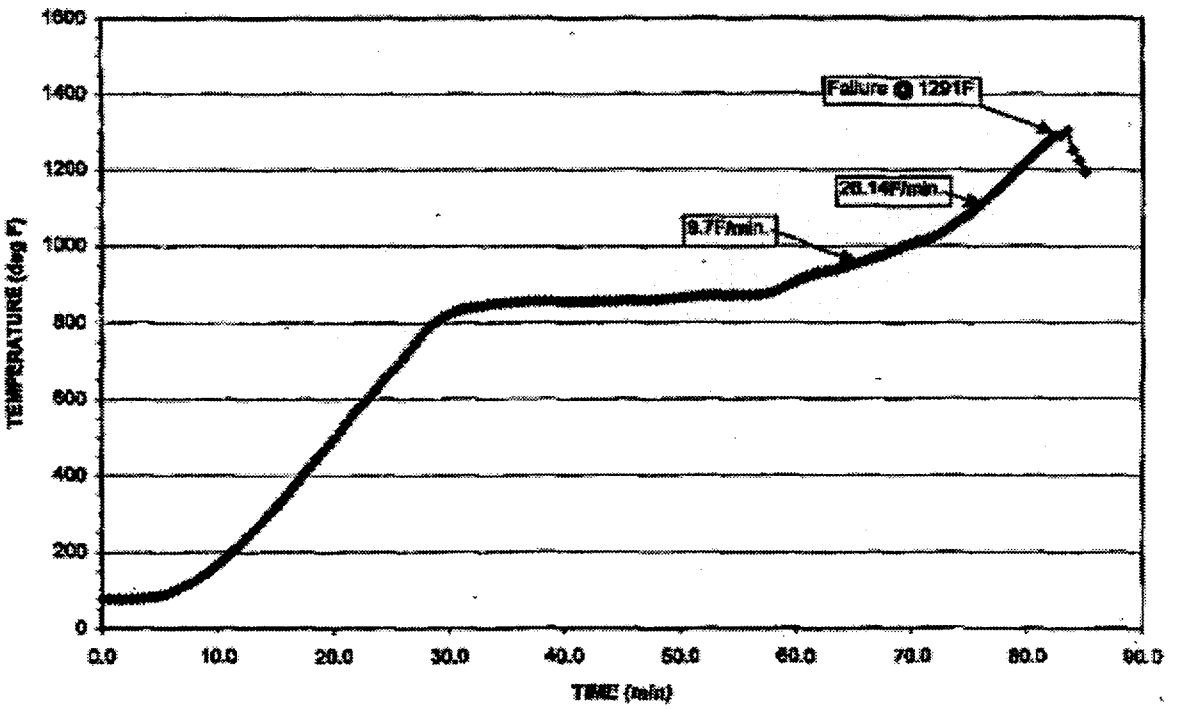

(b)

Fig. 70. Temperature ramps used in FTI tests on Electrosleeved specimens with part-throughwall notches (a) BTF-3 and (b) BTF-7.

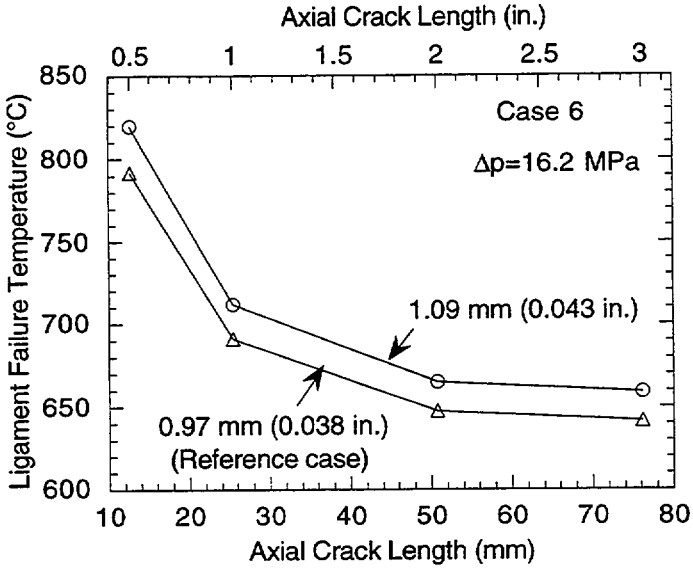

Fig. 71. Effect of Electrosleeve thickness on predicted ligament failure temperature of tube with throughwall axial cracks.

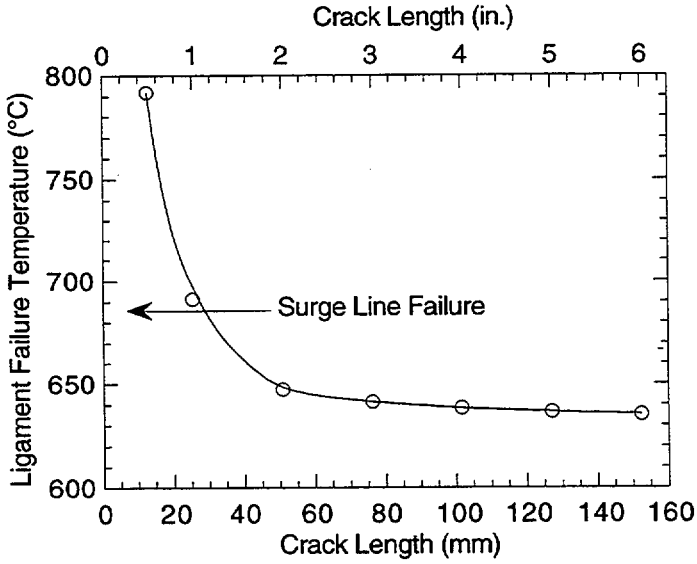

Fig. 72. Effect of crack length on predicted ligament failure temperature of reference Electrosleeved tube with throughwall axial cracks in parent tube during Case 6RU SBO severe accident ramp.

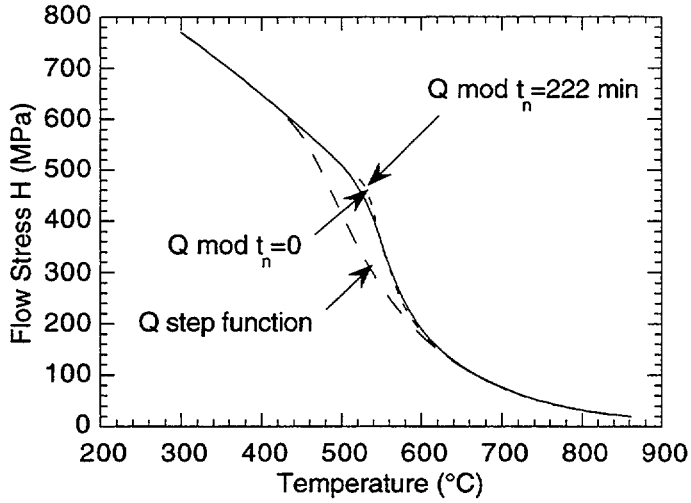

Fig. 73. Effect of shape of variation of activation energy with temperature on calculated loss of flow stress for 1°C min ramp. Nucleation time t_n has little effect on flow stress at temperatures of interest.

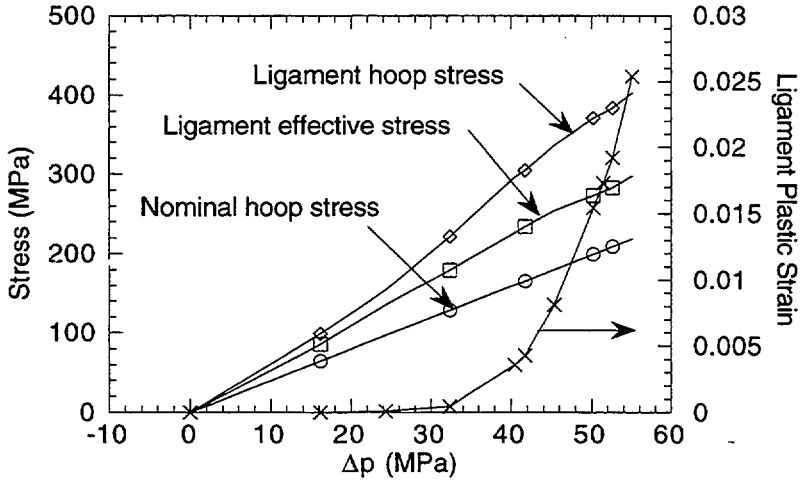

Fig. 74. Variations of average hoop stress, average effective stress, and average hoop plastic strain in ligament with pressure as calculated from FEA results for homogeneous tube of wall thickness 2.24 mm (0.088 in.) containing a 76-mm (3 in.)-long, 1.27-mm (0.050 in.)-deep part-throughwall axial crack. Also shown is variation of nominal hoop stress in unflawed tube with pressure.

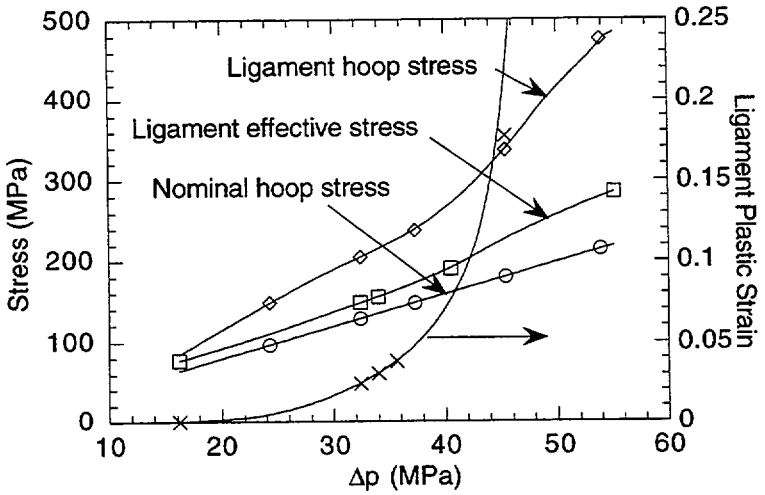

Fig. 75. Variations of average hoop stress, average effective stress, and average hoop plastic strain in ligament with pressure as calculated from FEA results for bi-layer tube (simulating Electrosleeved tube at high temperature) with 0.9-mm (0.038 in.)-thick inner layer and 1.27-mm (0.050 in.)-thick outer layer containing 76-mm (3 in.)-long 100% throughwall axial crack. Flow stress ratio between outer and inner layer = 2. Also shown is variation of nominal hoop stress in unflawed tube with pressure.

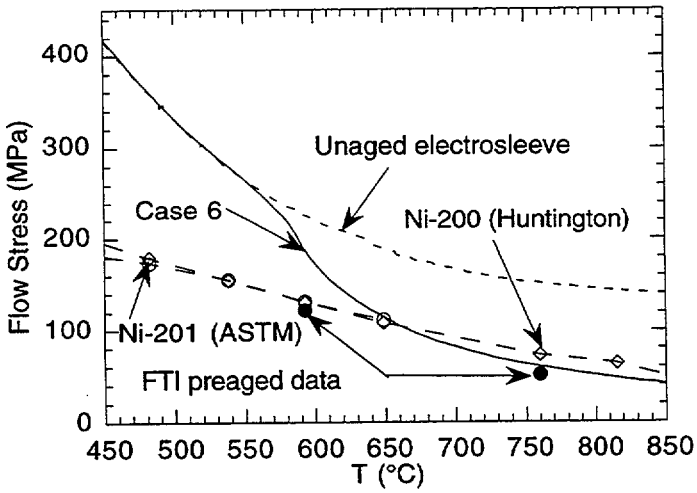

Fig. 76. Comparison of calculated flow stresses (including aging) of Electrosleeve (solid line) with flow stress data (open symbols) of Ni 200 (Huntington) and Ni-201 (ASTM). Also shown are flow stress of unaged electrosleeve (short dashed line) and two FTI flow stress data (filled circle) on 30-min aged specimens.

NRC FORM 335 (2-89) NRCM 1102, 3201, 3202

U.S. NUCLEAR REGULATORY COMMISSION

BIBLIOGRAPHIC DATA SHEET

(See instructions on the reverse)

1. REPORT NUMBER (Assigned by NRC, Add Vol., Supp., Rev., and Addendum Numbers, if any.)

NUREG/CR-6664
ANL-99/23

2. TITLE AND SUBTITLE

Pressure and Leak-Rate Tests and Models for Predicting Failure of Flawed Steam Generator Tubes

3. DATE REPORT PUBLISHED

MONTH	YEAR
August	2000

4. FIN OR GRANT NUMBER

W6487

5. AUTHOR(S)

S. Majumdar, K. Kasza, J. Franklin

6. TYPE OF REPORT

Technical

7. PERIOD COVERED *(Inclusive Dates)*

8. PERFORMING ORGANIZATION - NAME AND ADDRESS *(If NRC, provide Division, Office or Region, U.S. Nuclear Regulatory Commission, and mailing address; if contractor, provide name and mailing address.)*

Argonne National Laboratory
9700 South Cass Avenue
Argonne, IL 60439

9. SPONSORING ORGANIZATION - NAME AND ADDRESS *(If NRC, type "Same as above"; if contractor, provide NRC Division, Office or Region, U.S. Nuclear Regulatory Commission, and mailing address.)*

Division of Engineering Technology
Office of Nuclear Regulatory Research
U.S. Nuclear Regulatory Commission
Washington, DC 20555-0001

10. SUPPLEMENTARY NOTES

J. Muscara, NRC Project Manager

11. ABSTRACT *(200 words or less)*

This report summarizes the models used for predicting failure pressures and leak rates in unrepaired steam generator tubes with axial and circumferential cracks that developed under normal operation and design-basis accident conditions. These models are first validated with failure and leak rate tests at room temperature and at 282°C on tubes with well-characterized rectangular EDM notches and are then applied to the failure and leak rate tests conducted on tubes with laboratory-generated outer-diameter stress corrosion cracks (ODSCC), which have highly complex morphology. A procedure for defining equivalent rectangular cracks for SCC cracks on the basis of Eddy Current +Point™ data is presented. Except for tests that exhibited time-dependent initiation and increase of leak rates, the model predictions are in reasonable agreement with test results. In the second half of the report, a model is presented for predicting failure during severe accidents of Electrosleeved steam generator tubes with axial cracks in the parent tubes. The model is refined on the basis of high-temperature failure test results on Electrosleeved tubes with electro-discharge-machined notches. It is then used to predict failure of Electrosleeved tubes with cracks subjected to postulated severe accident transients.

12. KEY WORDS/DESCRIPTORS *(List words or phrases that will assist researchers in locating the report.)*

steam generator tubes
leak rate
failure
model

13. AVAILABILITY STATEMENT

unlimited

14. SECURITY CLASSIFICATION

(This Page) unclassified

(This Report) unclassified

15. NUMBER OF PAGES

16. PRICE

NRC FORM 335 (2-89)

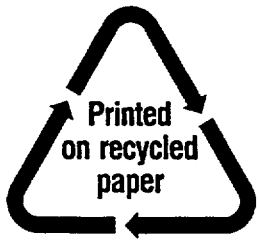

Federal Recycling Program

UNITED STATES
NUCLEAR REGULATORY COMMISSION
WASHINGTON, D.C. 20555-0001